2022

DETECTING SLOW SLIP EVENTS FROM SEAFLOOR PRESSURE DATA USING MACHINE LEARNING

Bing He
University of Rhode Island, hebingjlu@gmail.com

Recommended Citation
He, Bing, "DETECTING SLOW SLIP EVENTS FROM SEAFLOOR PRESSURE DATA USING MACHINE LEARNING" (2022). *Open Access Dissertations.* Paper 1451.
https://digitalcommons.uri.edu/oa_diss/1451

DETECTING SLOW SLIP EVENTS FROM SEAFLOOR PRESSURE DATA USING MACHINE LEARNING

BY

BING HE

A DISSERTATION SUBMITTED IN PARTIAL FULFILLMENT OF THE

REQUIREMENTS FOR THE DEGREE OF

DOCTOR OF PHILOSOPHY

IN

GRADUATE SCHOOL OF OCEANOGRAPHY

UNIVERSITY OF RHODE ISLAND

2022

DOCTOR OF PHILOSOPHY DISSERTATION

OF

BING HE

APPROVED:

Dissertation Committee:

Major Professor	Meng (Matt) Wei
	Yang Shen
	Kathleen Donohue
	Marco Alvarez
	Brenton DeBoef DEAN OF THE GRADUATE SCHOOL

UNIVERSITY OF RHODE ISLAND

2022

ABSTRACT

Largest earthquakes with destructive tsunamic waves mostly occurred in the offshore subduction zone, causing massive fatalities and significant property losses. Due to the limitations of the seafloor geodesy, it is hard to know the stress status offshore, like the terrestrial geodesy. The shallow slow slip event (SSE) occurrence provides an approach to studying the shallow subduction zone stress status and investigating the area and size of the potential large earthquake and following tsunamis. SSE is a bridge linking the slip rates from aseismic creeping near the trench to the highly locked region in the seismogenic zone. Seafloor pressure measurement, as the high precision, low cost, and continuous vertical deformation records, is the most common way of studying offshore vertical deformation caused by geodetic movements. However, due to the long-term instrumental drift and considerable water movement noise in the data, detecting and measuring shallow SSEs from the seafloor pressure data is still very hard.

In manuscript one, we developed a machine learning detector to detect the slow slip event in seafloor pressure data. Because real seafloor pressure data is not this abundant, we first trained the machine learning detector using synthetic data, and then applied the well-trained detector to the real seafloor pressure data collected by the HOBITSS project in New Zealand. The trained model can successfully detect an SSE and the accuracy increases with SSE amplitude. The synthetic data test also shows that the machine learning model outperformed the traditional matched filter method. Our detector found five events in real pressure

data in New Zealand between 2014-12015, two of which are confirmed by the onshore GPS records.

In manuscript two, we applied our machine learning detector to Alaska. The Southern Alaska subduction zone is a high seismic risk zone. Megathrust earthquakes and following devastating tsunami waves threaten south Alaska and the entire Canada and US west coast. We want to know the stress status at the shallow subduction zone in southern Alaska. In this study, we improved our previous machine learning detector by detecting both uplift and subsidence signals. We found four adjacent stations at 100-m water depth were uplifted, while four adjacent stations near the trench subsided in days 290-310 of 2018. This pattern is unlikely oceanographic in origin, based on an analysis of 10-year model output from an ocean circulation model (HYCOM). This pattern is consistent with a simulated ground deformation from a circular SSE on the subduction interface. We also investigated the daily seismicity and tremors using both onshore and offshore seismometers. We found that these seismic activities are closely related to our detected SSE: (1). A few tremors occurred before and near the SSE area. (2). the increased seismicity after SSE is located at the positive stress change area. Furthermore, our detected SSE is located 150-km northeast of the 2020 Mw 7.8 Alaska earthquake and the updip of the 2021 Mw 8.2 Chignik earthquake. The SSE has possibly increased the Coulomb stress in the area of these two large earthquakes.

The major problem for previous papers is correctly and broadly removing the oceanographic signals as much as possible. Therefore, in Chapter Three, we investigated the water column movement contribution to seafloor pressure by combining the machine learning method and ocean circulation model. We first applied the random forest method to study different features' importance in predicting seafloor pressure data, and then we used deep learning neural networks to better predict the results by incorporating the time information. This is an ongoing project. For future work, the well-trained model can be generalized using a small part of real data, and more available observations can be used to predict the real seafloor pressure.

ACKNOWLEDGEMENTS

I would like to express my most sincere appreciation to my advisor Matt Wei. I am so lucky to have Matt as my advisor on this long Ph.D. journey in my life. His great enthusiasm for scientific research has had a significant influence on my research. Matt is a very responsible advisor. No matter how busy he was, he could always make time to provide help for my study and life. We use Slack in our team. Matt always replies to us within 24 hours. I am not a morning person, and Matt has to get up early for his child. I usually send him lots of questions late at night. He usually replies to me before 8 a.m. for the next morning and gives me many ideas for the next day's work.

It was a great pleasure to talk about science with Matt. He always had so many interesting new ideas that greatly enlightened me. He provides me with many approaches and accessible spaces to explore. In the first year of my Ph.D., I do not know how to efficiently do research and solve the questions. He talked about my work with me every two days, taught me how to solve a big question one step by one step, and how to make an efficient work schedule. We had such frequent individual meetings for one semester until I had a clear research goal and work plan, and then he gradually became hands-off.

Matt gives me many chances to attend conferences and meet different scientists. Every time there is a related conference, he will send the conference information to me immediately, telling me that do not to worry about the traveling fee, and he can help me find travel support. I can attend at least two conferences per year before the pandemic days. Matt always encourages me to talk about my

research to different people. I am a little shy when talking with prestigious professors. Matt emailed them to introduce me in advance and help me prepare a few useful sentences during conversations. His efforts gave me much confidence and helped me overcome my social anxiety.

Matt does not only care for our research but also care for our non-academic life. During the explosion of COVID-19 in China, I was stuck in China for over 3 months. I was very anxious. Matt gives me enough patience and help. He told me no matter where I was, I only needed to complete my research task step by step, and he could meet me outside of the working time whenever I had questions. He helped me find a remote job in rock & core and let me not worry about the renting and living expenses. Finally, I went to Dubai for 16 days and successfully entered the US.

I enjoy the working environment in our group. Matt encourages us to help and teach each other. He also treats us when we have some progress to celebrate. I am so happy to work with Matt as his first Ph.D. student and sincerely thank him for everything he has done for me.

I also would like to extend my deepest gratitude to my committee members: Yang Shen, Kathleen Donohue, Marco Alvarez, and Rachel Schwartz. I have really learned a lot from them during these years at GSO. The completion of my dissertation would not have been possible without their help. They gave me much helpful feedback on my Ph.D. research during my qualification exam as well as my research proposal. Those valuable suggestions from them have greatly improved my Ph.D. research and my dissertation.

Specifically, I want to first thank Professor Yang Shen. Yang broadens our research horizons. He always sends advanced research papers and exciting research news to us. Let young scientists know the latest research outcomes. Yang is also the guide for my machine learning study in GSO. When the machine learning study just started blossoming in geoscience, Yang offered a machine learning class and built a great environment to study the new subject in a group. I also really enjoyed learning from and discussing with Yang. Every time I talk with him, I can always be inspired. Yang can quickly find the key to my question and give me valuable suggestions.

I also want to thank Professor Kathleen Donohue, Professor Randolph Watts, and Dr. Karen Tracey. Seafloor geodesy is an interdisciplinary subject, including physical oceanography, geodesy, and seismology. They taught me much knowledge about physical oceanography. My every progress is closed related to their teaching. Matt, Kathy, Karen, Randy, and I have the group meeting every Friday afternoon in the first and second years of my Ph.D. We talked about my progress and the project's plan. It was a great pleasure talking with and learning from them. They are very knowledgeable and friendly. My spoken English was poor during the first year of my Ph.D., but they still listened to my presentation carefully and taught me how to process and analyze pressure data step by step. I feel full of energy and confidence every time after our group meeting.

I am also grateful to Professor Marco Alvarez. I sit in Marco’s class, “Machine Learning”. This class is offered by CS department under special studies. I missed the deadline to choose the class. When I emailed Marco about whether I could sit in his class, Marco quickly agreed without hesitation and let me join their class group and online discussion platform. This is my first time systematically studying machine learning. His class helps me fill the gap between online tutorials and realistic problems. His suggestions and comments on my machine learning study help me build confidence in publishing the papers.

I also enjoyed working with all the current and former colleagues in the Matt and Yang group, including graduate students: Pengcheng Shi, PeiChin Wu, Sandra Slead, LingChao He, Xiaozhuo Wei, and Jiahang Li; postdocs, and visitors: Yiming Luo, Xueyang Bao, Nian Wang. The daily communication, weekly seminars, as well as research collaboration, have enriched my Ph.D. life. Years of life in such a large group have taught me how to communicate with and listen to other people from different backgrounds. Furthermore, the harmonic group environment gives me many chances to learn from others.

Thanks also to other professors in the department, especially those who offered courses that I took: Melissa Omand, Katherine Kelly, Rebecca S. Robinson, Susanne Menden-Deuer, Chris Kincaid, Colleen B. Mouw, Tatiana Rynearson, Kelton McMahon, Brian Savage. I have really learned lots of knowledge and skills from the great courses they provided. The training I received from their courses was significant and helped me better think about and solve the scientific questions I met in my research.

I would like to acknowledge the assistance of all GSO staff. Their efforts and support have made GSO a wonderful community for me to focus on my study and research. Special thanks to Meredith Clark and David Smith. Every time I have any problems, they will help me solve problems quickly. When I encounter some questions and walk around the GSO campus, everyone I meet on the road will say hi to me and ask about my current situation. All my stresses would go away with their asking. I feel very comfortable and lucky in our big GSO group.

Last but not least, I am deeply indebted to my family. Life in a foreign country sometimes may be challenging; my parents always provide me with invaluable suggestions and selfless support and try their best to give me the best they can offer, although they are thousands of miles away, and we have 12 hours of jet lag. I am incredibly grateful to my husband, Jiuxun Yin. Every progress I make is closely related to Jiuxun's support. Every difficult moment is relieved because of his company. Because of him, every dream would have been possible, and life is always colorful. I am the luckiest person in the world to have Jiuxun with me.

PREFACE

The dissertation includes three chapters. The first two chapters are written in manuscript format. The third chapter includes an ongoing project.

Manuscript One, “Detecting Slow Slip Events From Seafloor Pressure Data Using Machine Learning”, was published in Geophysical Research Letters, 2022.

Manuscript Two, “A shallow slow slip event preceded the 2021 Mw8.2 Chignik earthquake in east-central Alaska”, has been submitted to Science Advance.

Chapter Three, “Quantifying the water contribution to seafloor pressure by combining machine learning method and ocean circulation models.”

TABLE OF CONTENTS

LIST OF TABLES

LIST OF FIGURES

CHAPTER 1

MANUSCRIPT 1

Detecting Slow Slip Events from Seafloor Pressure Data Using Machine Learning

Bing He[1]*, Meng Wei[1], D. Randolph Watts[1], and Yang Shen[1]

1. Graduate School of Oceanography, University of Rhode Island.

*Corresponding author: Bing He (bing-he@uri.edu)

Published in 2022, Geophysical Research Letters,

https://doi.org/10.1029/2020GL087579

Key points:

- Using a machine learning method, we detected five events in seafloor pressure data offshore New Zealand, two of which are likely SSEs.
- Performance of the machine learning method is better than the traditional matched filter method.
- This method can be especially useful where the trench is far from GPS onshore.

Abstract

Detecting slow slip events (SSEs) at offshore subduction zones is important to understand the slip behaviour on offshore subduction megathrusts, where tsunamis can be generated. The most widely used method to detect SSEs is to measure the vertical seafloor deformation caused by SSEs using seafloor pressure data. However, due to the small signal-to-noise ratio and instrumental drift, such detection is very difficult. In this study, we trained a machine learning model using synthetic data to detect SSEs, and applied it to real pressure data in New Zealand between 2014-2015. Our method detected five events, two of which are confirmed by the onshore GPS records. Besides, our model performs better than the traditional matched filter method. We conclude that machine learning could be used to detect SSEs in real seafloor pressure data. The method can be applied to other regions, especially where near trench GPS is not available.

Plain Language Summary

We applied machine learning to detect a special tectonic signal recorded by pressure sensors sitting on the seafloor. This signal represents the release of tectonic stress between earthquakes and thus their existence indicates a lower likelihood of future large

earthquakes and tsunamis. It is difficult to detect this signal because of the high noise. Here we show that machine learning successfully detected two such signals and three possible cases in data collected near New Zealand between 2014-2015. The method has the potential to transform our way of detecting such signals in seafloor pressure data offshore New Zealand and elsewhere, especially where the signal source is far away from the shoreline.

1.1 Introduction

Our ability to forecast catastrophic earthquakes and tsunamis on offshore subduction zone such as the 2004 Sumatra and 2011 Japan earthquakes remains weak (Burgmann & Chadwell, 2014). One main limitation is our lack of ability to measure, detect, and quantify small and slow tectonic deformation including SSEs at the seafloor (Burgmann & Chadwell, 2014). This situation is changing as several large projects using seafloor pressure sensors have been conducted in the last decade in Japan (DONET, S-NET), Cascadia (Cascadia Initiative, OOI), New Zealand (HOBITSS), and Alaska (AACSE). These projects have accumulated large datasets that can be analyzed for detecting SSEs.

Even with these datasets, detecting SSEs using seafloor pressure data is still challenging. First, the tectonic signal is small relative to background noise. The typical vertical displacement of a very large SSE is up to a few centimeters spanning weeks to months, although many can be much smaller (Dixon et al., 2014). The corresponding pressure change on a seafloor pressure sensor is comparable to the variation caused by deep ocean meso-scale eddy flows, therefore making detecting SSEs difficult. Second, instrumental drift exists in pressure records (Watts & Kontoyiannis, 1990). Usually, Absolute Pressure

Gauge measurements drift non-linearly for the first few months of the deployment and then linearly after that (Polster et al., 2009). The drift is often removed by fitting the data with an exponential plus linear curve. Part of the SSE amplitude could be masked by the drift and is easily obscured during the pressure data de-drifting procedure.

In the last few years, there has been a surge in the application of machine learning methods in many fields including geosciences. Kong et al., (2019) and Bergen et al., (2019) reviewed recent applications of machine learning in seismology and solid earth geoscience, respectively. Among these studies, convolutional neural network (CNN) plays an important role. It can learn from the complex features of images (Mousavi et al., 2019; Perol et al., 2018), simulate seismic waves (Moseley et al., 2018), classify volcanic ash particles (Shoji et al., 2018) and pick P and S waves in long seismograms (Zhu & Beroza, 2019). In addition, recurrent neural network (RNN) is very helpful to learn the pattern of sequential data (Q. Wang et al., 2017; Wiszniowski et al., 2014).

In this study, we combined CNN and RNN to detect SSEs in seafloor pressure data collected by the HOBITSS project near New Zealand between 2014-2015. As far as we know, this is the first effort using machine learning for this purpose. We compared the results with a traditional matched filter method. The results show that machine learning methods are promising as a means to detect SSEs in seafloor pressure data and could be useful to detect SSEs in other subduction zones, especially where the onshore GPS is too far away from the trench.

1.2 Data and Method

1.2.1 Synthetic Dataset

We applied a supervised machine learning method, which learns the relationship between input and output pairs and then make predictions based on the learned relation. Usually, a large dataset (millions of pieces) is required to train a supervised machine learning model. Because real seafloor pressure data is not this abundant, we first built a large synthetic dataset and used it to train the model. Then we evaluated the performance and applied the trained model to the real data.

The target real data is the seafloor pressure data collected by the HOBITSS project (Wallace et al., 2016). It includes 15 pressure sensors deployed at water depths ranging from 700 m to 3400 m and with an average spacing of 20 km (Figure 1.1a). We used 14 stations with high quality data which span about 250 days between June of 2014 to March of 2015 (station TXBPR2 was not used due to short record). The seafloor pressure data includes oceanographic signals from tides, currents, and eddies, as well as instrumental drift and possible tectonic signals. We first removed tides using tidal response analysis (Munk et al., 1966) and removed the instrumental drift using an exponential plus linear curve (Watts & Kontoyiannis, 1990). Then we calculated the pressure difference between each station and the average of two reference stations (LOBS4 and TXBPR1) in the deep ocean, where no tectonic signal is expected. This subtraction removes large-scale pressure variations affecting both deep and shallow sensors, such as coastal trapped waves and large eddies, which have a spatial scale of several hundreds of kilometers. By calculating the difference, we reduced the variance of the pressure data to a few centimeters equivalent without affecting the tectonic signal (Wallace et al., 2016). This pressure difference is the data we use to detect SSEs.

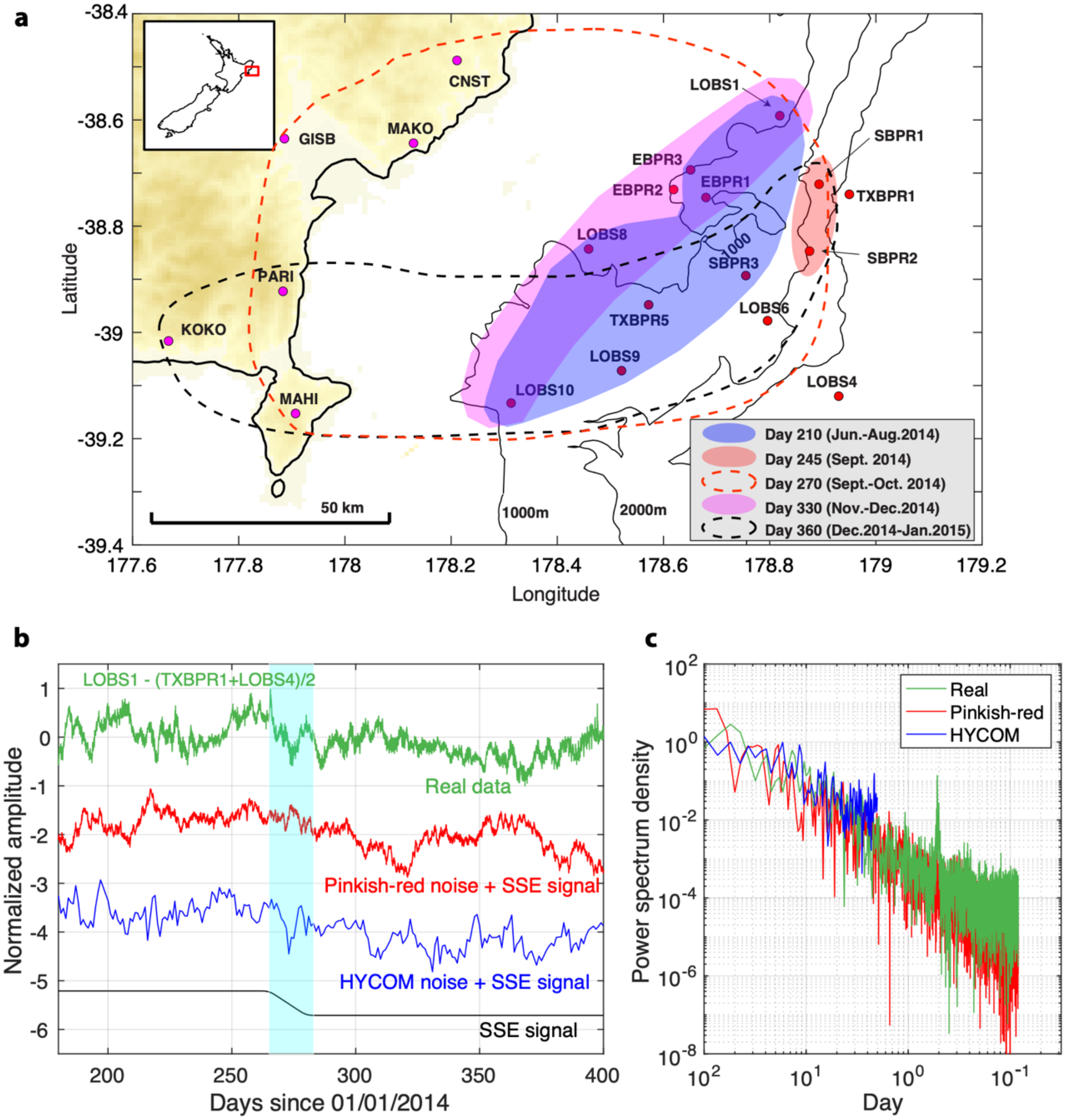

__Figure 1.1.__ (a) Map of the study area near New Zealand (the red box in the small inset on top left). Red dots are the HOBITSS seafloor absolute pressure gauge sites (APG) and the magenta dots on land are GPS stations. TXBPT1 and LOBS4, on the subducting Pacific Plate are chosen as the reference sites to remove the common mode oceanographic noise. Black solid lines are water depth contours at 1000 m interval. The black and the red dashed

lines show the area of SSEs around day 270 and 360. The three shaded area show the other detected events by the machine learning code (PRt-model) as shown in Figure 1.4b. The HYt-model shows similar detections (Figure 1.11). (b) Examples of real data (station LOBS1 minus reference), pinkish-red noise adding SSE signal, HYCOM output adding SSE signal, and SSE signal. Blue bar shows the time of SSE in the data and models. (c) The spectral analysis of the three curves as shown in (b).

A synthetic dataset should resemble real data as closely as possible, e.g. they should have similar power spectra. We used two methods to generate such a dataset: pinkish-red noise and an ocean circulation model output. The pinkish-red noise data was generated by the MATLAB random noise function with spectral density ($\beta = -1.8$), where β is the spectral slope of the variance versus frequency, which we chose to mimic the observed pinkish-red noise nature of the residual pressures. The ocean circulation model is from the Hybrid Coordinate Ocean Model (HYCOM) between 2009-2018 in the target region. The spatial resolution of HYCOM is 1/12 degree. As the model output does not include pressure, we calculated it using the temperature, salinity, and sea surface height within layers at each grid point. We obtained the pressure difference by subtracting reference pressure seaward of the trench. Examples of real data at station LOBS1, and synthetic data (with a synthetic SSE signal added to it), as well as their corresponding power spectrum are shown in Figure 1.1 b-c. Because HYCOM is daily output, the spectrum lacks higher frequency content. The power spectral density of all three decreases linearly with frequency and the HYCOM data appears to have a slightly smaller slope.

Each piece of trained data is two-month long with hourly samples. The ramp-shaped synthetic SSEs were added to part of the dataset (Figure 1.1c; Table 1.1). The SSE ramp with duration between 7-30 days and amplitude between 1.8-5.3 hPa can occur at any time within the trained data. A Gaussian shaped time window with 8 hours was used to smooth the corners of the SSE ramp. For simplification, we only used a ramp signal corresponding to a pressure decrease since we aim to detect seafloor uplift. A small linear and random drift was also added to each piece of data to account for the imperfect de-drifted process (Figure 1.2). Because the HYCOM output is daily, we interpolated HYCOM data into hourly samples using a spline function in MATLAB. To perform a fair comparison between HYCOM and pinkish-red noise, we created hourly pinkish-red noise data and ran a one-day Gaussian low pass filter.

Table 1.1. *The characteristics for synthetic data*

Input Data	Value or Characteristics
Sample length	60 days
Sample rate	One hour
Noise (ocean)	Pinkish-red noise, ocean model output (HYCOM)
Signal	Ramp (random duration between 7-30 days, random temporal position)
Signal-to-noise ratio (SNR)	-3 to 6 dB for single SNR tests, equivalent to amplitude to 1.8 – 5.3 hPa (cm) in offshore of New Zealand 0-3 dB, equivalent to 2.2-3.5 for mixed-SNR and application to real data
Drift	Straight line (random slope), The maximum slope could be 1.5 times of the amplitude of target SSE ramp.
Synthetic data	Noise + Ramp + Drift

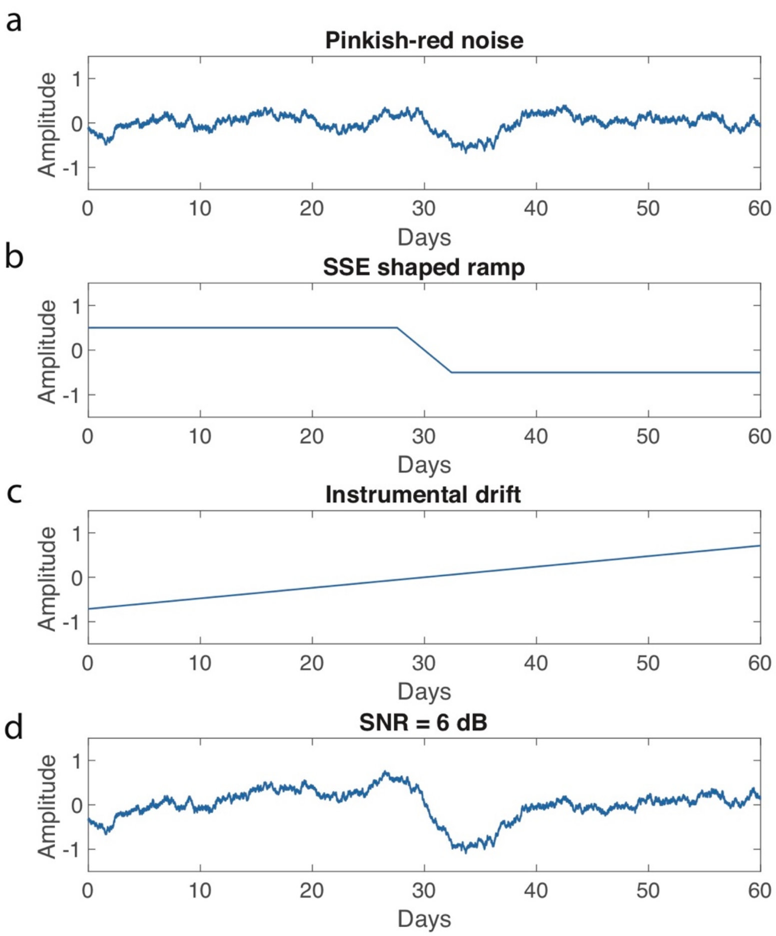

Figure 1.2. A case shows how the synthetic data are constructed. The SNR for this case is 6 dB. The synthetic data (d) is the combination of pinkish-red noise (a), SSE shaped ramp (b), and instrumental drift (c). When the SSE occurs, the continental plate moves upward. The pressure at the seafloor decreases, so the ramp is down.

1.2.2. Machine Learning Methods

We combined CNN and RNN to train the model (layer structure shown in Figure 1.3) and we also showed RNN is very useful in this study (Figure 1.4). Mathematically, each layer is performing a matrix multiplication using an existing library. Conceptually, the 1D convolutional layers were used to extract the features of the data. Then the bidirectional

Long Short Term Memory (LSTM) structures were used to optimize feature extraction in sequential data. In the end, a fully connected layer was set to generate a probability of detection. The machine learning code runs this process many times (each called an epoch) and monitors the performance. When the validation performance is not improved, the machine learning code stops the calculation. We used a binary cross-entropy as the loss function and chose an ADAM algorithm for optimization (Kingma & Ba, 2014). The loss function is defined as:

$$Loss = -(y \times log(p) + (1 - y) \times log\,(1 - p)) \tag{1.1}$$

where y is a binary indicator of 0 or 1 and p is the predicted probability.

We first used a single station as the input to train the machine learning model as shown in section 1.3.2. Later, in order to improve the accuracy of detection, we used three close stations as input to the same training algorithm.

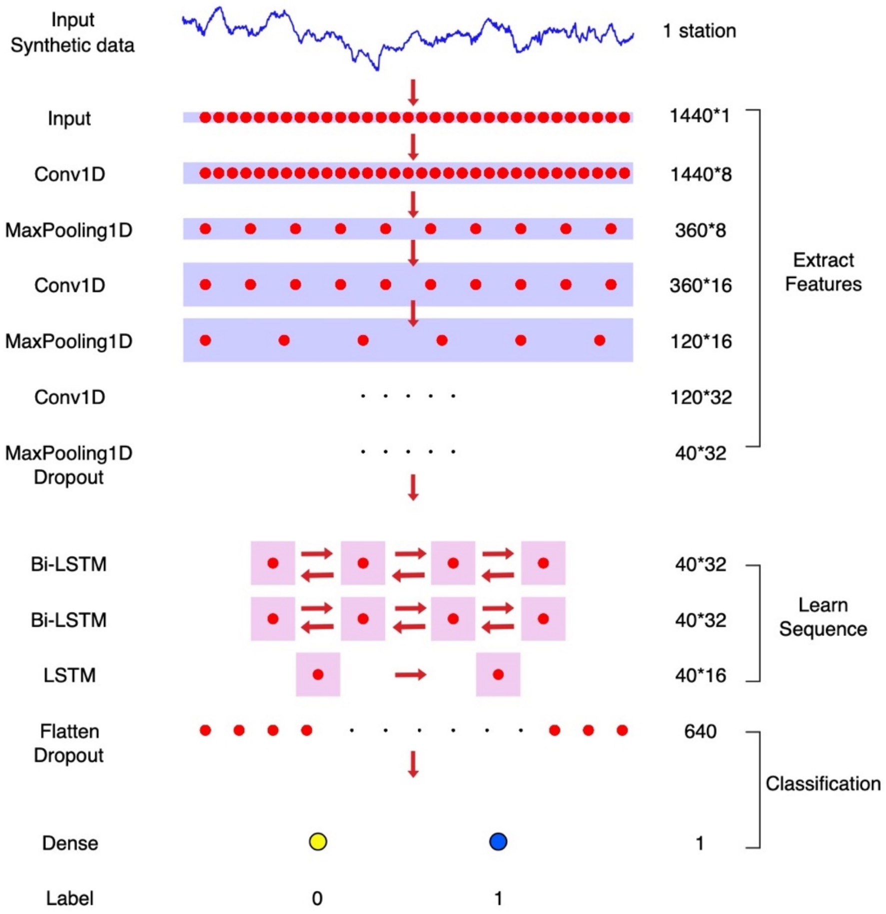

Figure 1.3. *Layer structure of our neural network. Left labels are the function names in the Keras package in Python. Conv1D means 1D convolutional neural network. MaxPooling1D means 1D max pooling layer. Dropout is the drop-out layer. Bi-LSTM means bilateral Long Short Term Memory layer. Flatten and dense are functional layer names. Right numbers are the rows and columns in each training layer. The filter and kernel sizes are chosen based on the experience and many tests.*

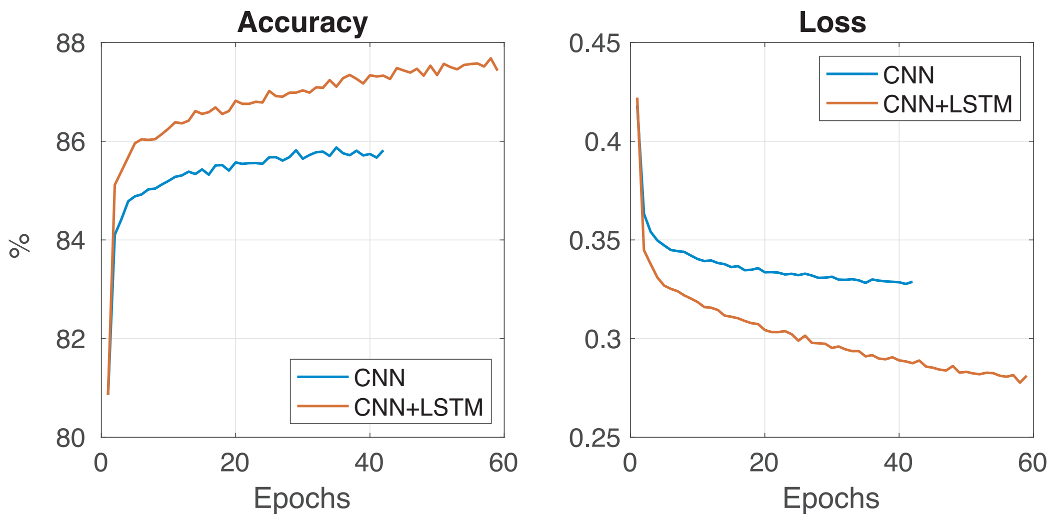

Figure 1.4. *This is a test to show the comparison of CNN model and the combination the CNN and LSTM model and this test used pinkish-red noise data with SNR 0-dB. Accuracy and loss represent the performance of model. The combination of the CCN and LSTM shows better performance than CNN only model. This result is also consistent with Mousavi et al., (2019)'s result.*

We also conducted extensive testing that use three stations as input instead of one station. We chose three stations that are close to each other (< 40 km) and had 101 combinations. For the HYt-model, we used HYCOM data at the study region to construct the synthetic data. For the PRt-model, three pieces of unrelated pinkish-red noise data were used. The model performance of the three-station case in synthetic data was much better than the one-station case. For example, in the same SNR, three-station cases had much higher accuracy and lower loss compared to the one-station cases (Figure 1.5).

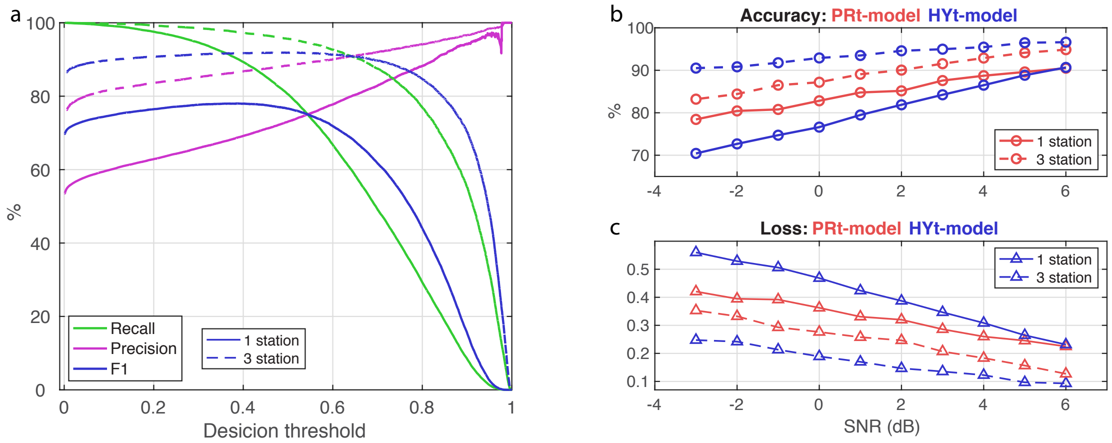

Figure 1.5.*(a) How key performance indicators change with decision threshold. This figure is from PRt-model. (b)(c) Accuracy and loss vary with signal to noise ratios. In figure (a)(b)(c), solid lines are from single-station trained models, while dashed lines are from three-station trained models. Pinkish-red noise data trained models are shown by red lines and HYCOM data trained models are shown by blue lines. For the single-station case, PRt-model is better than HYt-model. For the three-station case, HYt-model performs better than PRt-model.*

Overall, the PRt-model outperforms the HYt-model for detecting the first large SSE around day 270 in the real data. It is difficult to evaluate the performance for detecting the event around day 360 because not all stations were affected. Here, we showed 6 representative cases (Figure 1.6). For stations that are around the northern part of study area, the PRt-model reported only one SSE (Figure 1.6.a, b). In contrast, when stations were located in the southern part, two SSEs were detected with high probabilities in both two models (Figure 1.6.c, d). For a few combinations, PRt-model reported nothing, but HYt-model found SSEs and possible events (Figure 1.6.e, f). Overall, the HYt-model seems to be very sensitive to small changes in the pressure time series. It might be due to the fact that

HYCOM data are from three close stations and have coherent noise for three stations. When additional noise adds to the HYCOM data, HYt-model becomes much more sensitive than PRt-model.

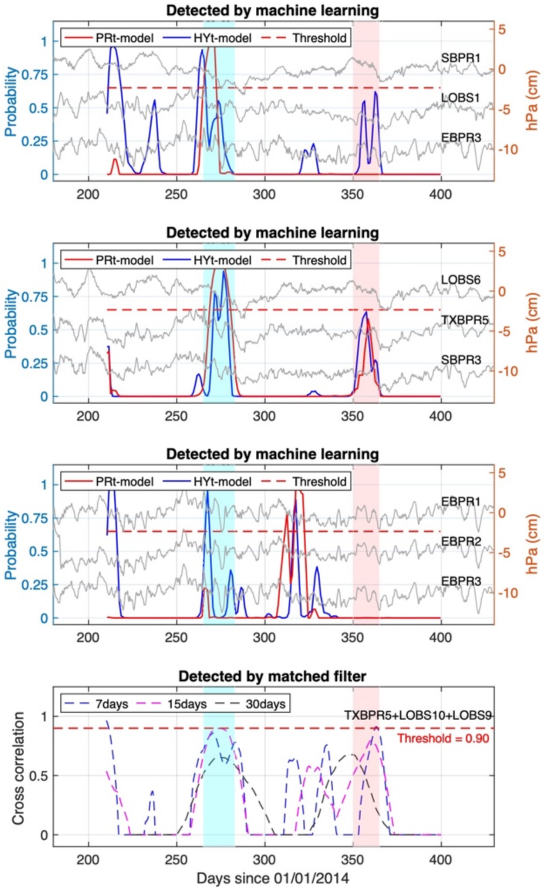

Figure 1.6. *Comparison between the machine learning model on three stations with a traditional matched filter method. (a-f) Machine learning detected probabilities on some three station combinations. The background three gray lines are three seafloor pressure difference data for the input to the machine learning method. The red and blue lines are detected probabilities from PRt-model and HYt-model, respectively. The red dashed line represents the decision threshold 0.65. (g-h) Detected results on average of three stations by the matched filter method. Blue, megenta and black lines are matched filtered output*

using 7-day, 15-day and 30-day templates, respectively. The horizontal dashed line shows the 0.9 detection threshold.

To compare the performance with the matched filter method, we stacked these three-station data and calculated correlation between the stacked values and templates with various durations. The performance of the matched filter for the three-station case is similar to that from the one-station case (Figure 1.6.g, h). A template is optimal to detect SSEs with a duration similar to the template but not SSEs with much different duration. For example, the combination of TXBPR5, LOBS10, LOBS9, 15-day template barely reached the threshold of 0.9 around day 270 whereas 7-day and 30-day templates missed it. Around day 360, only 7-day template detected the second SSE and other templates failed.

Even though the three-station case performs better on synthetic data than the one-station case, its performance on real data is not as well as expected, which depends on combinations of three stations. It is difficult to visualize and interpret the results from the three-station model, so we prefer the one-station method.

We labeled each piece of data either 1 or 0, where 1 means that the center of the SSE is on day 30 at the mid-point of the 2-month long data, and 0 means that either no SSE occurs in the data, or the center of this SSE is before day 28 or after day 32 of the data. The four-day buffer zone around the middle of the 2-month period allows the model to scan real data at any length of time and remain stable. Half of the synthetic data were labeled as 1, one fourth of the data contained an SSE but not in the middle, and the remaining one fourth only contained noise and instrumental drift. We normalized all the input data by dividing by their standard deviation, and divided them into training (60%), validation (20%), and test (20%) datasets. The machine learning algorithm trains the model and validates the performance in the meanwhile. After training, we used test datasets to evaluate the model performance. We built multiple synthetic datasets with the SSE ramp duration ranging from 7 to 30 days and various signal-to-noise ratios (SNRs). SNR is defined as:

$$SNR = 10 \times log_{10}\left[\left(\frac{\sigma_{ramp}}{\sigma_{noise}}\right)^2\right] \tag{1.2}$$

where σ is the standard deviation, σ_{ramp} and σ_{noise} represent the standard deviation of SSE ramp and noise, respectively. The models are trained separately with the SNR ranging from -3 to 6 dB, which is equivalent to the amplitude of 1.8 to 5.3 cm SSE ramp in the study region, and then we evaluated how the performance improves with increasing SNRs. later, we built a dataset with mixed SNRs, which we used to detect SSEs in real data.

The training dataset needs to be big enough to ensure performance. We used 80,000 for each individual SNR dataset and 320,000 for mixed SNRs dataset. To validate the data size, we compared the performance of the pinkish-red noise training dataset from 10,000 to 640,000 for SNR = 0 dB. Both accuracy and loss improve slightly from 10,000 to 40,000 and remain about the same level with the larger dataset (Figure 1.7.).

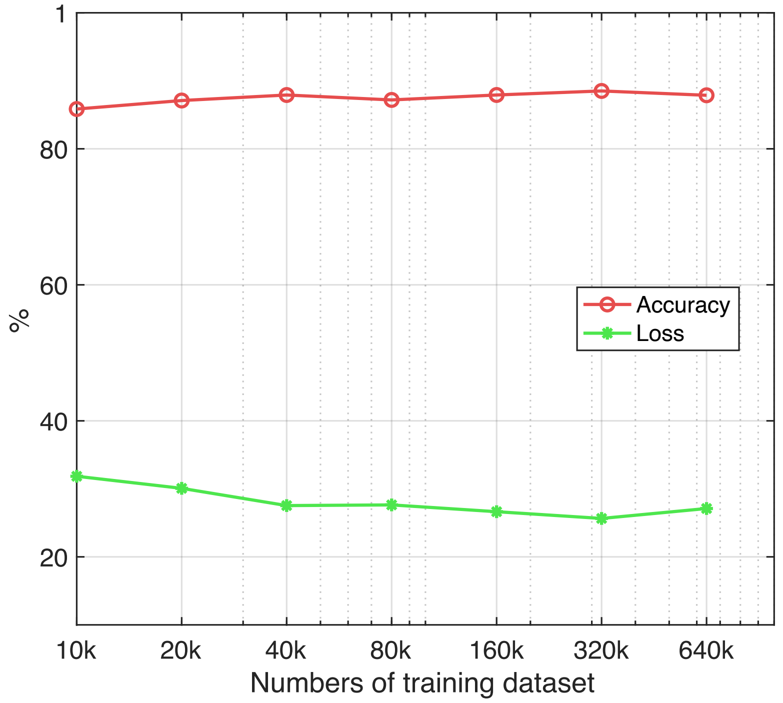

Figure 1.7. *Accuracy and loss for SNR = 0 dB with different sizes of trained dataset. We used pinkishred-noise data to do this test. There is an improvement when the data size increased from 10k to 40k. We used trained dataset with at least 80k pieces of data in our model.*

1.3 Results

1.3.1. Performance on synthetic data

We first evaluated the performance of these two synthetic data trained models using evaluation metrics including accuracy, precision, recall, F1 score and loss, which are defined as:

$$Accuracy = \frac{TP+TN}{TP+TN+FP+FN}, \tag{1.3}$$

$$Precision = \frac{TP}{TP+FP}\ , Recall = \frac{TP}{TP+FN}, \quad (1.4)$$

$$F1 = 2 \times \frac{Precision \times Recall}{Precision+Recall}, \quad (1.5)$$

where TP, TN, FP and FN represent the number of true positive, true negative, false positive and false negative, respectively. Accuracy is used for evaluating the fraction of data correctly detected. Precision represents the fraction of true positive among the predicted positive tags. Recall represents the fraction of true positive among the actual positive tags. F1 is a function of precision and recall and is used to choose an appropriate decision threshold. Loss function (eq. 1) is defined in the Methods section and is used to evaluate how accurate the model is. The smaller the loss value, the better the trained model.

A decision threshold of probability is required to define detection, so these evaluation metrics are calculated. As shown in Figure 1.8.a: precision increases with threshold whereas recall and F1 decrease with threshold. These three curves intersect at a threshold of 0.55, which we chose to use for this model. The recall and precision versus threshold figures in the different SNRs look very similar, and the decision threshold fluctuates within 3%.

Figure 1.8.b shows the performance of the pinkish-red noise data trained model (PRt-model) and HYCOM data trained model (HYt-model) on different SNRs. With increasing SNR, accuracy and loss gradually improve. The accuracy of the HYt-model ranges from 0.71 to 0.91 for SNR between -3 dB to +6 dB, and that of the PRt-model ranges from 0.79 to 0.91.

The loss decreases with SNR from 0.56 to 0.22 in HYt-model and 0.42 to 0.22 in PRt-model. In all, PRt-model outperformed HYt-model in the synthetic test for most SNRs.

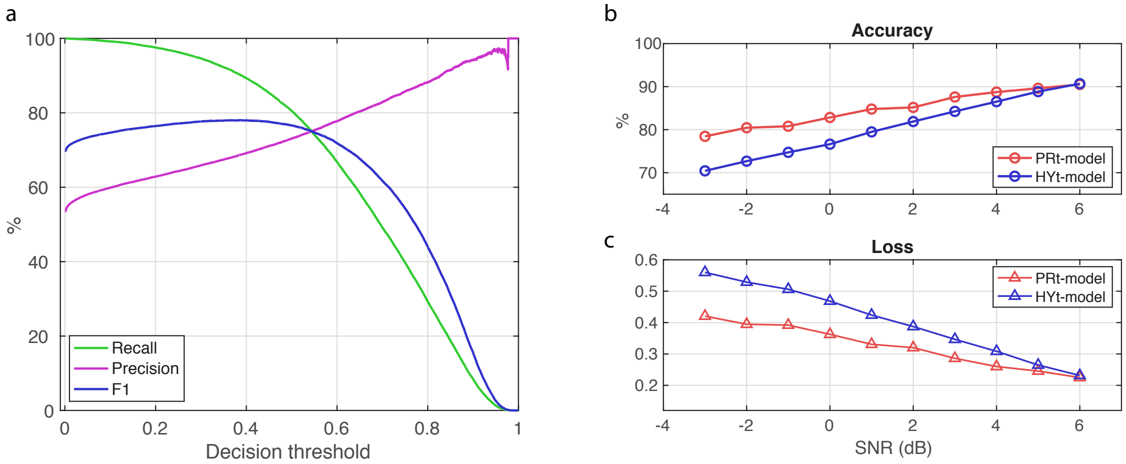

Figure 1.8. *(a) How key performance indicators change with decision threshold. This figure uses the PRt-model. HYt-model also gives a threshold at 0.55. (b)(c) Accuracy and loss vary with SNRs for both models.*

1.3.2. Performance on real data

We applied our model to real pressure data collected by the HOBITSS project in New Zealand between June 2014 and March 2015, during which at least two SSEs have been identified (Muramoto et al., 2019; Wallace et al., 2016; Warren-Smith et al., 2019). Before application, we built a synthetic dataset with mixed SNRs and ramp durations to train our model. We first used the same range of SNR as the single SNR tests, but the performance in synthetic test is poor (<70% accuracy). Thus, we shortened the SNR range to 0 and 3 dB, which is equivalent to 2.2-3.5 cm of seafloor uplift considering the water noise level in the study region. The ramp duration was randomly chosen between 7 and 30 days. We processed the real pressure data as described in an earlier section to remove tides, instrumental drift, and common wave signals. Then we used a one-day Gaussian low passed filter to remove high frequency component in the data. Later, we used a 60-day sliding window with 1-day sliding increment to cut the data into hundreds of pieces and normalized each piece, dividing by their standard deviation. Finally, we put all the pieces into machine learning code and make predictions (Figure 1.9.b).

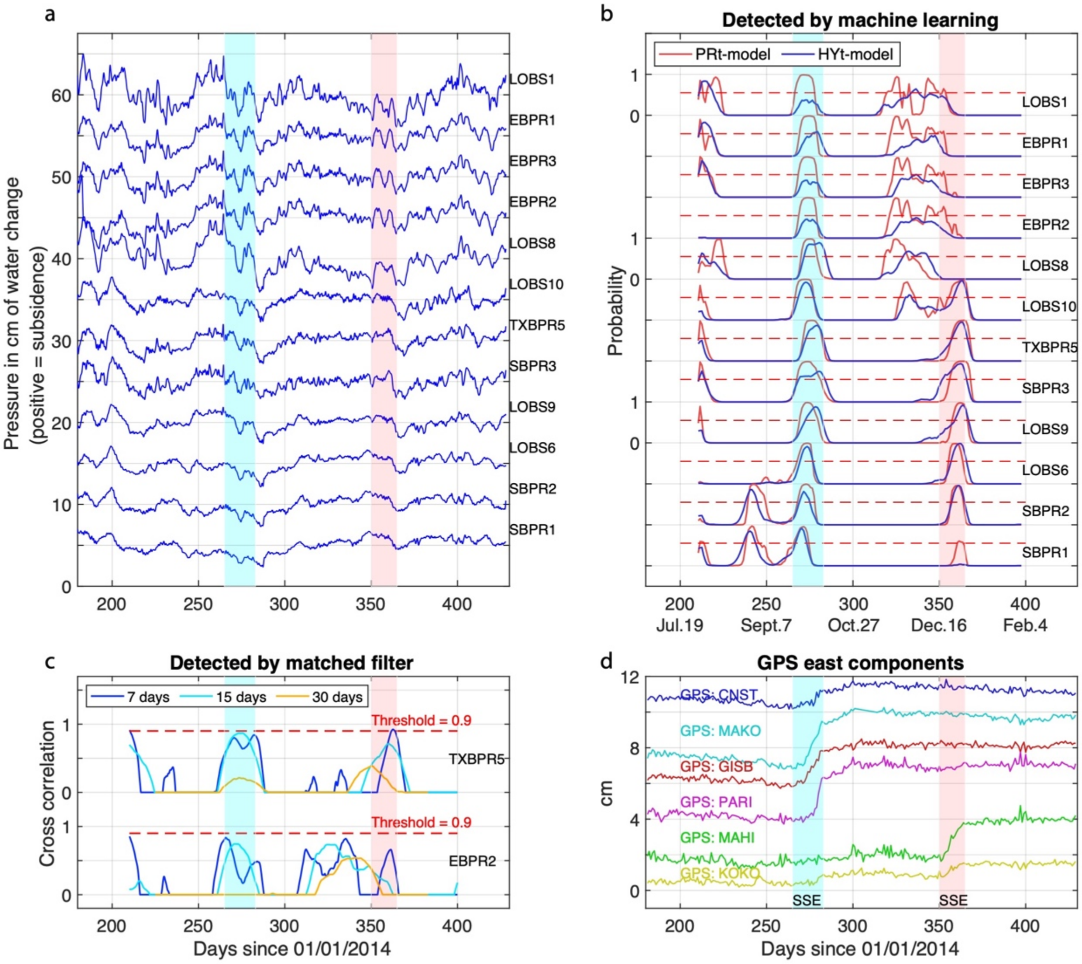

Figure 1.9. *(a) The de-tided, de-drifted and 1-day low pass filtered pressure difference data at each station. Blue and red shadings indicate the time of two known SSEs based on the GPS records (d). (b) Detected probabilities from PRt-model and HYt-model. All the detected probabilities curves (red and blue) varies from 0 to 1. Red dashed lines represent the threshold of 0.55. The detected probabilities that exceed the threshold are considered as events. (c) The cross correlation of the template and data from station TXBPR5 and EBPR2. Both template and windowed data are normalized before cross correlation. Blue,*

cyan and yellow lines are output using 7-day, 15-day and 30-day templates, respectively. The horizontal dashed lines show the threshold of 0.9. (d) The east components of the GPS stations.

Both the PRt-model and HYt-model successfully detected two large events that have been reported previously as SSEs (Figure 1.1.a and Figure 1.9.b). The first event around day 270 affected all stations in this region (except deep sea reference sites), including five nearby GPS stations. The second event is smaller and affected only six pressure stations and three GPS stations. In addition to these two events with GPS confirmation, both models reported three more events: one around day 210 in eight stations; one around day 245 in two stations; another one around day 330 in six stations. On one hand, all the stations with detection are spatially coherent (Figure 1.1 a), suggesting the detection of a real event rather than random noise. On the other hand, without additional information such as GPS, it is difficult to know whether these events were from small SSEs or ocean eddies. For most detections, both models showed a similar level of probability. For several stations (EBPR1-3 and LOBS1), the PRt-model showed higher probabilities in the same events compared to the HYt-model (Figure 1.9 b).

To compare the performance with the traditional matched filter method, we used templates with durations of 7 days, 15 days and 30 days to calculate the cross-correlation with the pressure difference data at each station (Figure 1.10). The performance of the matched filter method depends on whether the template ramp length is similar to the real signal. For station TXBPR5, only the 15-day template barely reached the 0.9 threshold for the SSE around day 270 and only the 7-day template exceeds the 0.9 threshold for the event around day 360 (Figure 1.9 c). It is likely that the two events have different durations in the seafloor pressure data. Therefore, no single template would successfully detect both events with high probability whereas our machine learning method can. For station EBPR2, none of the three templates detected the event around day 270 (Figure 1.9 c), but the machine learning method did.

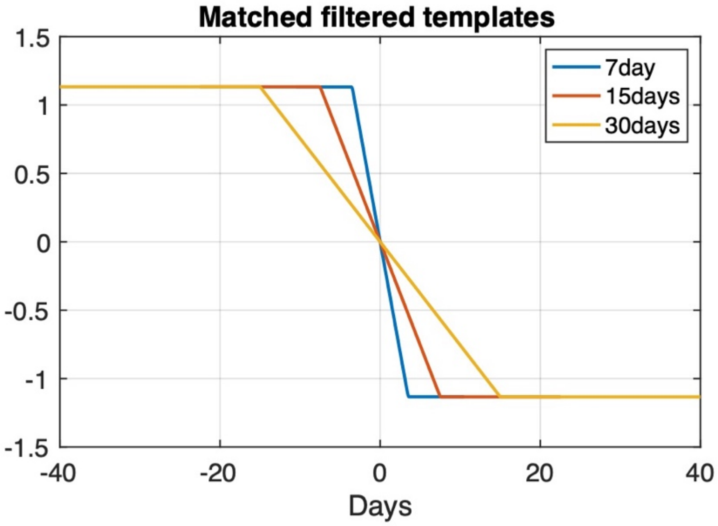

Figure 1.10. *Templates used in this study for the matched filter method. They also represent the SSE ramp used to construct the synthetic data.*

1.4 Discussion

Overall, the performance of the HYt-model and PRt-model is similar. They both detected five events in the real dataset. In synthetic tests, the PRt-model outperformed HYt-model slightly (figure 1.8; higher accuracy and lower loss). It is possibly due to the fact that HYt-model used daily output which lacks energy in high frequency. In real application, PRt-model reported high probability (>90%) for all stations for the largest event around day 270, whereas HYt-model reported lower probability (~40%) at stations EBPR1-3 and LOBS1. We also conducted 3-station tests, which used data from 3-stations as input instead of one. Compared to 1-station tests, both models in 3-station tests showed higher accuracy and lower loss in synthetic tests, which is expected with more data. In contrast to the 1-station cases, HYt-model outperformed PRt-model in synthetic tests for 3-station cases (Figure 1.5), which could be due to the presence of coherent noise in HYCOM data. Applying to real data, the model performance of 3-station tests depends on the specific station combination (Figure 1.6), and there is no consistent difference between the two models. We focused on the 1-station method because the results from 3-station tests are hard to interpret and depend on the station combination.

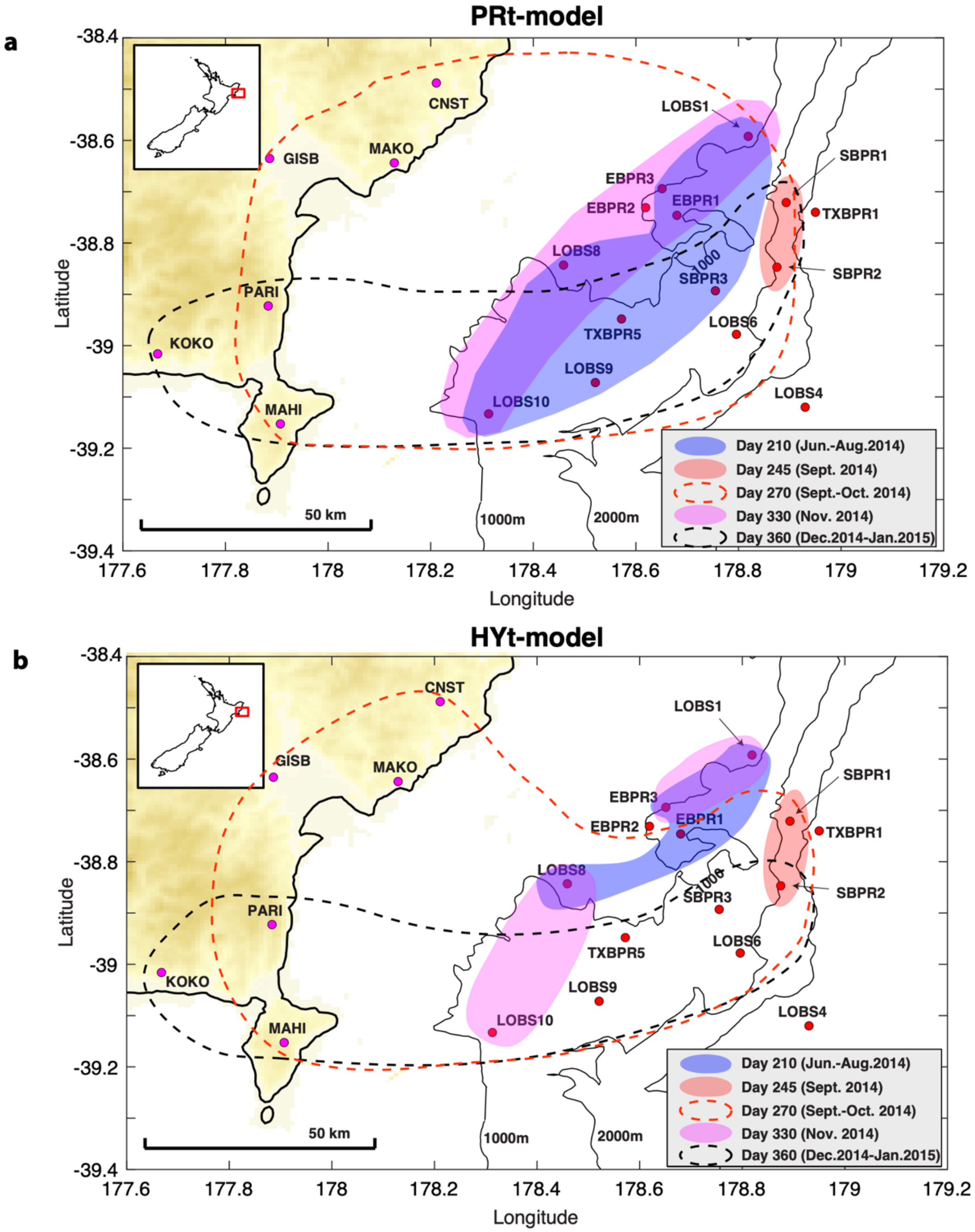

Figure 1.11. *Comparison between PRt-model and HYt-model on the spatial distribution of detected events. Map of the study area near New Zealand (the red box in the small inset on top left). Red dots are the HOBITSS seafloor absolute pressure gauge sites (APG) and the magenta dots on land are GPS stations. TXBPT1 and LOBS4, on the subducting Pacific Plate are chosen as the reference sites to remove the common mode oceanographic noise.*

Black solid lines are water depth contours at 1000 m interval. The black dashed line and the red dashed line show the area of SSE events around day 270 and 360. The three shaded area show the other detected events by the machine learning code. The data used to plot these shaded and unfilled circles are from Figure 4b. The detected probabilities that exceed the threshold of 0.55 are considered as events. (a) is from PRt-model and (b) is from HYt-model.

Intuitively, the detection probability should increase with SNR. Assuming the noise level is about the same for all the stations, there should be a correlation between detection probability and uplift amplitude. However, we did not find such correlation after comparing the uplift maps (Wallace et al., 2016; Muramoto et al., 2019) with the detection probability of single-station models (PRt-model and HYt-model) for the largest SSE (around day 270) (Figure 1.12). There might be two reasons. First, the detection probability appeared to saturate at certain SNR, above which the probability is always high (>90%). For example, the detection probability using the PRt-model is consistently high (>90%) and with little variations among stations whereas the uplift maps show considerable variation in magnitude (2-3 times). It is likely that the smallest uplift is above the saturation threshold for PRt-model. Second, the low detection probability is due to the low SNR. The noise level is not the same among stations and stations in shallow water have higher noise. This is consistent with the observation that the HYt-model shows low detection probabilities (~0.4) in shallow stations EBPR1-3 and LOBS1, because the reference sites are in deep water and the pressure correlation between stations decreases with distance (Fredrickson et al., 2019).

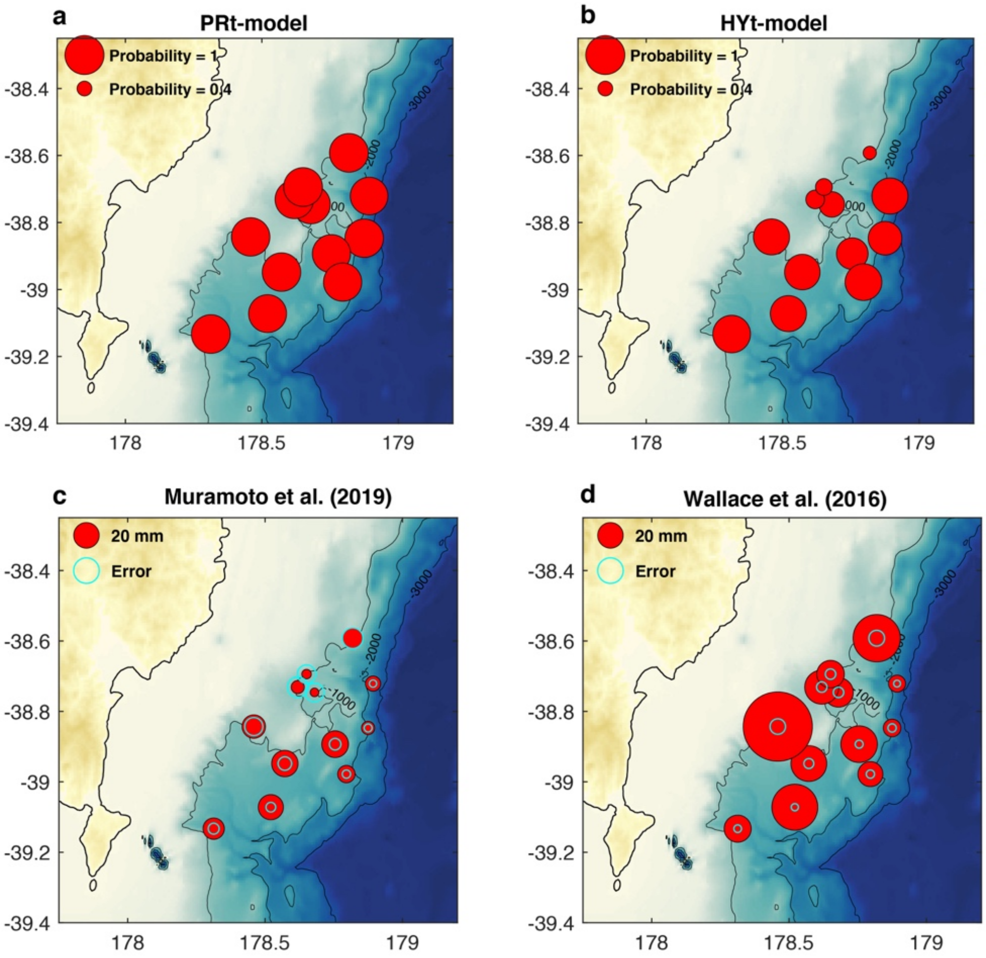

Figure 1.12. *(a) The detected probabilities from the single station trained machine learning model for the first SSE from the PRt-model. The circle size represents the detected probability. (b) same as (a) but from the HYt-model. (c) is from Muramoto et al., (2019)'s result. (d) is from Wallace et al., (2016)'s result. (c)(d) The amplitudes of the first SSE. The size of the red circle represents the amplitude of the vertical displacement. The size of cyan circle represents the error bar.*

Many studies have attempted to reduce the oceanographic noise in seafloor pressure measurements (Inazu et al., 2012; Ito et al., 2013; Suzuki et al., 2016; He et al., 2018; Muramoto et al., 2019; Wallace et al., 2016). Some have tried to do this using ocean models.

For example, Hino et al., (2014) and Muramoto et al., (2019) used the global barotropic ocean model to remove the major component of ocean mass variation. Hino et al., (2014) reduced the water noise to 2-4 cm in the region near the 2011 Tohoku earthquake. Muramoto et al., (2019) reduced the variance in the HOBITSS data by about 66%, significantly lower than the variance reduction achieved by using nearby reference sites as done here and in Wallace et al., (2016). Even though ocean models do improve the measurement, they may also introduce an error of a few centimeters (Inazu et al., 2012). These models should therefore be used with care. Others have also tried to make the correction by using in-situ measurements. For example, He et al., (2018) yielded moderate improvement by using deep current measurements and the geostrophic balance assumption to remove the ocean circulation contribution. Gomberg et al., (2019) suggested an approach to reduce the water column and some instrumental noise based on correlations between seafloor temperature and pressure changes. In this paper, we did not apply the machine learning method to these corrected measurements. However, our machine method can also be applied to timeseries corrected in alternative ways such as detect SSEs, for which the only difference might be the noise structure and SNRs.

The neural network method can be viewed as a collection of matched filters. Therefore, it is not surprising that it outperforms results from using a single template. In practice, one may run detection using many matched filters and only report ones with high probability along with the template. However, this is cumbersome. Our method provides an alternative and convenient way to detect SSEs in seafloor pressure data. The model only needs to be trained once and then can be applied to many data quickly.

Shallow SSEs are now recognized in several subduction zones, including New Zealand, Japan and Costa Rica (Dixon et al., 2014; Ito et al., 2013a; Wallace et al., 2016). Peninsular areas in these regions have allowed precise on-land geodetic measurements to detect these events, with limitations. However, shallow SSEs may be present in many other subductions such as Cascadia but remains undetected (Fredrickson et al., 2019). Our method provides a novel approach to detect SSEs using seafloor pressure data in these regions where the trench is far from land-based geodetic networks. One remaining challenge is how to distinguish between SSEs and ocean effects after detection. The solution might be including additional data such as borehole tiltmeter and study the spatial pattern of the signal. More studies like this and applications to more areas will be needed to address this problem.

Acknowledgments

The authors thank Laura Wallace and an anonymous reviewer for reviewing this paper. The authors thank Kathleen Donohue and Karen Tracey for the guidance on analyzing seafloor pressure data and Marco Alvarez for the suggestions on neural network algorithm. The authors are grateful to the PIs of the HOBITSS project for providing the New Zealand seafloor pressure data (which is now available through the IRIS DMC). The GPS timeseries shown are provided by GeoNet (www.geonet.org.nz). The HYCOM data is from HYCOM website (https://www.hycom.org/dataserver/gofs-3pt0/analysis); High resolution bathymetry data is from GMRT website (https://www.gmrt.org/GMRTMapTool/). Most of the data processing, calculations and figures are carried out using MATLAB. The machine learning code was written with Python packages Keras (https://keras.io/) and Scikit-learn (https://scikit-learn.org/stable/). This work was supported by NSF award 1728060.

References

Burgmann, R., & Chadwell, D. (2014). Seafloor Geodesy. *Annual Review of Earth and Planetary Sciences*, 42(1), 509–534. https://doi.org/10.1146/annurev-earth-060313-054953

Aagaard, B. T., Knepley, M. G., & Williams, C. A. (2013). A domain decomposition approach to implementing fault slip in finite-element models of quasi-static and dynamic crustal deformation. *Journal of Geophysical Research: Solid Earth*, *118*(6), 3059–3079. https://doi.org/10.1002/jgrb.50217

Araki, E., Saffer, D. M., Kopf, A. J., Wallace, L. M., Kimura, T., Machida, Y., et al. (2017). Recurring and triggered slow-slip events near the trench at the Nankai Trough subduction megathrust. *Science*, *356*(6343), 1157–1160. https://doi.org/10.1126/science.aan3120

Baba, T., Hirata, K., Hori, T., & Sakaguchi, H. (2006). Offshore geodetic data conducive to the estimation of the afterslip distribution following the 2003 Tokachi-oki earthquake. *Earth and Planetary Science Letters*, *241*(1), 281–292. https://doi.org/10.1016/j.epsl.2005.10.019

Badrinarayanan, V., Handa, A., & Cipolla, R. (2015, May 27). SegNet: A Deep Convolutional Encoder-Decoder Architecture for Robust Semantic Pixel-Wise Labelling. arXiv. https://doi.org/10.48550/arXiv.1505.07293

Baillard, C., Crawford, W. C., Ballu, V., Hibert, C., & Mangeney, A. (2013). An Automatic Kurtosis-Based P- and S-Phase Picker Designed for Local Seismic Networks. *Bulletin of the Seismological Society of America*, *104*(1), 394–409. https://doi.org/10.1785/0120120347

Baker-Yeboah, S., Watts, D. R., Byrne, D. A., & Witter, D. L. (2011). Sea Surface Height Variability in the eastern South Atlantic from Satellite and in situ Measurements, *2011*, OS23A-1620.

Bappy, J. H., Simons, C., Nataraj, L., Manjunath, B. S., & Roy-Chowdhury, A. K. (2019). Hybrid LSTM and Encoder–Decoder Architecture for Detection of Image Forgeries. *IEEE Transactions on Image Processing*, *28*(7), 3286–3300. https://doi.org/10.1109/TIP.2019.2895466

Barcheck, G., Abers, G. A., Adams, A. N., Bécel, A., Collins, J., Gaherty, J. B., et al. (2020). The Alaska Amphibious Community Seismic Experiment. *Seismological Research Letters*, *91*(6), 3054–3063. https://doi.org/10.1785/0220200189

Bartlow, N. M., Wallace, L. M., Beavan, R. J., Bannister, S., & Segall, P. (2014). Time-dependent modeling of slow slip events and associated seismicity and tremor at the Hikurangi subduction zone, New Zealand. *Journal of Geophysical Research: Solid Earth*, *119*(1), 734–753. https://doi.org/10.1002/2013JB010609

Bergen, K. J., Johnson, P. A., Hoop, M. V. de, & Beroza, G. C. (2019). Machine learning for data-driven discovery in solid Earth geoscience. *Science*, *363*(6433). https://doi.org/10.1126/science.aau0323

Beroza, G. C., & Ide, S. (2011). Slow Earthquakes and Nonvolcanic Tremor. *Annual Review of Earth and Planetary Sciences*, *39*(1), 271–296. https://doi.org/10.1146/annurev-earth-040809-152531

Bürgmann, R. (2018). The geophysics, geology and mechanics of slow fault slip. *Earth and Planetary Science Letters*, *495*, 112–134. https://doi.org/10.1016/j.epsl.2018.04.062

Chen, K. H., Tai, H.-J., Ide, S., Byrne, T. B., & Johnson, C. W. (2018). Tidal Modulation and Tectonic Implications of Tremors in Taiwan. *Journal of Geophysical Research: Solid Earth*, *123*(7), 5945–5964. https://doi.org/10.1029/2018JB015663

Crowell, B. W., & Melgar, D. (2020). Slipping the Shumagin Gap: A Kinematic Coseismic and Early Afterslip Model of the Mw 7.8 Simeonof Island, Alaska, Earthquake. *Geophysical Research Letters*, *47*(19), e2020GL090308. https://doi.org/10.1029/2020GL090308

Cummings, J. A., & Smedstad, O. M. (2013). Variational Data Assimilation for the Global Ocean. In S. K. Park & L. Xu (Eds.), *Data Assimilation for Atmospheric, Oceanic and Hydrologic Applications (Vol. II)* (pp. 303–343). Berlin, Heidelberg: Springer. https://doi.org/10.1007/978-3-642-35088-7_13

Davies, J., Sykes, L., House, L., & Jacob, K. (1981). Shumagin Seismic Gap, Alaska Peninsula: History of great earthquakes, tectonic setting, and evidence for high seismic potential. *Journal of Geophysical Research: Solid Earth*, *86*(B5), 3821–3855. https://doi.org/10.1029/JB086iB05p03821

Davis, E. E., Villinger, H., & Sun, T. (2015). Slow and delayed deformation and uplift of the outermost subduction prism following ETS and seismogenic slip events beneath Nicoya Peninsula, Costa Rica. *Earth and Planetary Science Letters*, *410*, 117–127. https://doi.org/10.1016/j.epsl.2014.11.015

Dixon, T. H., Jiang, Y., Malservisi, R., McCaffrey, R., Voss, N., Protti, M., & Gonzalez, V. (2014). Earthquake and tsunami forecasts: Relation of slow slip events to subsequent earthquake rupture. *Proceedings of the National Academy of Sciences*, *111*(48), 17039–17044.

Dobashi, Y., & Inazu, D. (2021). Improving Detectability of Seafloor Deformation From Bottom Pressure Observations Using Numerical Ocean Models. *Frontiers in Earth Science*, *8*. https://doi.org/10.3389/feart.2020.598270

Fredrickson, E. K., Wilcock, W. S. D., Schmidt, D. A., MacCready, P., Roland, E., Kurapov, A. L., et al. (2019). Optimizing Sensor Configurations for the Detection of Slow-Slip Earthquakes in Seafloor Pressure Records, Using the Cascadia Subduction Zone as a Case Study. *Journal of Geophysical Research: Solid Earth*, *124*(12), 13504–13531. https://doi.org/10.1029/2019JB018053

Freymueller, J. T., Suleimani, E. N., & Nicolsky, D. J. (2021). Constraints on the Slip Distribution of the 1938 MW 8.3 Alaska Peninsula Earthquake From Tsunami Modeling. *Geophysical Research Letters*, *48*(9), e2021GL092812. https://doi.org/10.1029/2021GL092812

Gomberg, J., Hautala, S., Johnson, P., & Chiswell, S. (2019). Separating Sea and Slow Slip Signals on the Seafloor. *Journal of Geophysical Research: Solid Earth*, *124*(12), 13486–13503. https://doi.org/10.1029/2019JB018285

Hayes, G. P., Moore, G. L., Portner, D. E., Hearne, M., Flamme, H., Furtney, M., & Smoczyk, G. M. (2018). Slab2, a comprehensive subduction zone geometry model. *Science*, *362*(6410), 58–61. https://doi.org/10.1126/science.aat4723

He, B., Watts, R. D., Tracey, K. L., Donohue, K. A., & Wei, M. (2018). Reducing `Noise' in Ocean Bottom Pressure Measurements in the Cascadia Subduction Zone. *AGU Fall Meeting Abstracts*, *T41F-0369*. Retrieved from http://adsabs.harvard.edu/abs/2018AGUFM.T41F0369H

He, B., Wei, M., Watts, D. R., & Shen, Y. (2020). Detecting Slow Slip Events From Seafloor Pressure Data Using Machine Learning. *Geophysical Research Letters*, *47*(11), e2020GL087579. https://doi.org/10.1029/2020GL087579

Hino, R., Inazu, D., Ohta, Y., Ito, Y., Suzuki, S., Iinuma, T., et al. (2014). Was the 2011 Tohoku-Oki earthquake preceded by aseismic preslip? Examination of seafloor vertical deformation data near the epicenter. *Marine Geophysical Research*, *35*(3), 181–190. https://doi.org/10.1007/s11001-013-9208-2

Huene, R. von, Miller, J. J., & Dartnell, P. (2016). A possible transoceanic tsunami directed toward the U.S. west coast from the Semidi segment, Alaska convergent margin. *Geochemistry, Geophysics, Geosystems*, *17*(3), 645–659. https://doi.org/10.1002/2015GC006147

Ide, S. (2012). Variety and spatial heterogeneity of tectonic tremor worldwide. *Journal of Geophysical Research: Solid Earth*, *117*(B3). https://doi.org/10.1029/2011JB008840

Inazu, D., Hino, R., & Fujimoto, H. (2012). A global barotropic ocean model driven by synoptic atmospheric disturbances for detecting seafloor vertical displacements from in situ ocean bottom pressure measurements. *Marine Geophysical Research*, *33*(2), 127–148. https://doi.org/10.1007/s11001-012-9151-7

Inoue, T., Ito, Y., Wallace, L. M., Yoshikawa, Y., Inazu, D., Garcia, E. S. M., et al. (2021). Water Depth Dependence of Long-Range Correlation in Nontidal Variations in Seafloor Pressure. *Geophysical Research Letters*, *48*(8), e2020GL092173. https://doi.org/10.1029/2020GL092173

Ito, Y., Hino, R., Kido, M., Fujimoto, H., Osada, Y., Inazu, D., et al. (2013a). Episodic slow slip events in the Japan subduction zone before the 2011 Tohoku-Oki earthquake. *Tectonophysics*, *600*, 14–26. https://doi.org/10.1016/j.tecto.2012.08.022

Ito, Y., Hino, R., Kido, M., Fujimoto, H., Osada, Y., Inazu, D., et al. (2013b). Episodic slow slip events in the Japan subduction zone before the 2011 Tohoku-Oki earthquake. *Tectonophysics*, *600*, 14–26. https://doi.org/10.1016/j.tecto.2012.08.022

Itoh, Y., Nishimura, T., Ariyoshi, K., & Matsumoto, H. (2019). Interplate Slip Following the 2003 Tokachi-oki Earthquake From Ocean Bottom Pressure Gauge and Land

GNSS Data. *Journal of Geophysical Research: Solid Earth*, *124*(4), 4205–4230. https://doi.org/10.1029/2018JB016328

Kingma, D. P., & Ba, J. (2014). Adam: A Method for Stochastic Optimization. *ArXiv:1412.6980 [Cs]*. Retrieved from http://arxiv.org/abs/1412.6980

Kong, Q., Trugman, D. T., Ross, Z. E., Bianco, M. J., Meade, B. J., & Gerstoft, P. (2019). Machine Learning in Seismology: Turning Data into Insights. *Seismological Research Letters*, *90*(1), 3–14. https://doi.org/10.1785/0220180259

Li, J., Shillington, D. J., Bécel, A., Nedimović, M. R., Webb, S. C., Saffer, D. M., et al. (2015). Downdip variations in seismic reflection character: Implications for fault structure and seismogenic behavior in the Alaska subduction zone. *Journal of Geophysical Research: Solid Earth*, *120*(11), 7883–7904. https://doi.org/10.1002/2015JB012338

Li, J., Shillington, D. J., Saffer, D. M., Bécel, A., Nedimović, M. R., Kuehn, H., et al. (2018). Connections between subducted sediment, pore-fluid pressure, and earthquake behavior along the Alaska megathrust. *Geology*, *46*(4), 299–302. https://doi.org/10.1130/G39557.1

Li, S., & Freymueller, J. T. (2018). Spatial Variation of Slip Behavior Beneath the Alaska Peninsula Along Alaska-Aleutian Subduction Zone. *Geophysical Research Letters*, *45*(8), 3453–3460. https://doi.org/10.1002/2017GL076761

Li, S., Freymueller, J., & McCaffrey, R. (2016). Slow slip events and time-dependent variations in locking beneath Lower Cook Inlet of the Alaska-Aleutian subduction zone. *Journal of Geophysical Research: Solid Earth*, *121*(2), 1060–1079. https://doi.org/10.1002/2015JB012491

Lindsey, E. O., Mallick, R., Hubbard, J. A., Bradley, K. E., Almeida, R. V., Moore, J. D. P., et al. (2021). Slip rate deficit and earthquake potential on shallow megathrusts. *Nature Geoscience*, *14*(5), 321–326. https://doi.org/10.1038/s41561-021-00736-x

Liu, C., Lay, T., Xiong, X., & Wen, Y. (2020). Rupture of the 2020 MW 7.8 Earthquake in the Shumagin Gap Inferred From Seismic and Geodetic Observations. *Geophysical Research Letters*, *47*(22), e2020GL090806. https://doi.org/10.1029/2020GL090806

Liu, C., Lay, T., & Xiong, X. (2022). The 29 July 2021 MW 8.2 Chignik, Alaska Peninsula Earthquake Rupture Inferred From Seismic and Geodetic Observations: Re-Rupture of the Western 2/3 of the 1938 Rupture Zone. *Geophysical Research Letters*, *49*(4), e2021GL096004. https://doi.org/10.1029/2021GL096004

Lomax, A., Virieux, J., Volant, P., & Berge-Thierry, C. (2000). Probabilistic Earthquake Location in 3D and Layered Models. In C. H. Thurber & N. Rabinowitz (Eds.), *Advances in Seismic Event Location* (pp. 101–134). Dordrecht: Springer Netherlands. https://doi.org/10.1007/978-94-015-9536-0_5

Montgomery-Brown, E. K., & Syracuse, E. M. (2015). Tremor-genic slow slip regions may be deeper and warmer and may slip slower than non-tremor-genic regions. *Geochemistry, Geophysics, Geosystems*, *16*(10), 3593–3606. https://doi.org/10.1002/2015GC005895

Moseley, B., Markham, A., & Nissen-Meyer, T. (2018). Fast approximate simulation of seismic waves with deep learning. *ArXiv:1807.06873 [Physics]*. Retrieved from http://arxiv.org/abs/1807.06873

Mousavi, S. M., Zhu, W., Sheng, Y., & Beroza, G. C. (2019). CRED: A Deep Residual Network of Convolutional and Recurrent Units for Earthquake Signal Detection. *Scientific Reports*, *9*(1), 1–14. https://doi.org/10.1038/s41598-019-45748-1

Mousavi, S. M., Ellsworth, W. L., Zhu, W., Chuang, L. Y., & Beroza, G. C. (2020). Earthquake transformer—an attentive deep-learning model for simultaneous earthquake detection and phase picking. *Nature Communications*, *11*(1), 3952. https://doi.org/10.1038/s41467-020-17591-w

Munk, W. H., Cartwright, D. D., & Bullard, E. C. (1966). Tidal spectroscopy and prediction. *Philosophical Transactions of the Royal Society of London. Series A, Mathematical and Physical Sciences*, *259*(1105), 533–581. https://doi.org/10.1098/rsta.1966.0024

Muramoto, T., Ito, Y., Inazu, D., Wallace, L. M., Hino, R., Suzuki, S., et al. (2019). Seafloor Crustal Deformation on Ocean Bottom Pressure Records With Nontidal Variability Corrections: Application to Hikurangi Margin, New Zealand. *Geophysical Research Letters*, *46*(1), 303–310. https://doi.org/10.1029/2018GL080830

Nanjo, K. Z., Hirata, N., Obara, K., & Kasahara, K. (2012). Decade-scale decrease inb value prior to the M9-class 2011 Tohoku and 2004 Sumatra quakes. *Geophysical Research Letters*, *39*(20). https://doi.org/10.1029/2012GL052997

Nishikawa, T., & Ide, S. (2018). Recurring Slow Slip Events and Earthquake Nucleation in the Source Region of the M 7 Ibaraki-Oki Earthquakes Revealed by Earthquake Swarm and Foreshock Activity. *Journal of Geophysical Research: Solid Earth*, *123*(9), 7950–7968. https://doi.org/10.1029/2018JB015642

Park, H., Oh, C., Moon, J., & Kim, S. (2018). Development of a lane change risk index using vehicle trajectory data. *Accident Analysis & Prevention*, *110*, 1–8. https://doi.org/10.1016/j.aap.2017.10.015

Perol, T., Gharbi, M., & Denolle, M. (2018). Convolutional neural network for earthquake detection and location. *Science Advances*, *4*(2), e1700578. https://doi.org/10.1126/sciadv.1700578

Polster, A., Fabian, M., & Villinger, H. (2009). Effective resolution and drift of Paroscientific pressure sensors derived from long-term seafloor measurements. *Geochemistry, Geophysics, Geosystems*, *10*(8). https://doi.org/10.1029/2009GC002532

Reverso, T., Marsan, D., Helmstetter, A., & Enescu, B. (2016). Background seismicity in Boso Peninsula, Japan: Long-term acceleration, and relationship with slow slip events. *Geophysical Research Letters*, *43*(11), 5671–5679. https://doi.org/10.1002/2016GL068524

Ross, Z. E., White, M. C., Vernon, F. L., & Ben-Zion, Y. (2016). An Improved Algorithm for Real-Time S-Wave Picking with Application to the (Augmented) ANZA Network in Southern California. *Bulletin of the Seismological Society of America*, *106*(5), 2013–2022. https://doi.org/10.1785/0120150230

Rousset, B., Fu, Y., Bartlow, N., & Bürgmann, R. (2019). Weeks-Long and Years-Long Slow Slip and Tectonic Tremor Episodes on the South Central Alaska Megathrust. *Journal of Geophysical Research: Solid Earth*, *124*(12), 13392–13403. https://doi.org/10.1029/2019JB018724

Ruiz, S., Metois, M., Fuenzalida, A., Ruiz, J., Leyton, F., Grandin, R., et al. (2014). Intense foreshocks and a slow slip event preceded the 2014 Iquique Mw 8.1 earthquake. *Science*, *345*(6201), 1165–1169. https://doi.org/10.1126/science.1256074

Saffer, D. M., & Wallace, L. M. (2015). The frictional, hydrologic, metamorphic and thermal habitat of shallow slow earthquakes. *Nature Geoscience*, *8*(8), 594–600. https://doi.org/10.1038/ngeo2490

Schorlemmer, D., & Wiemer, S. (2005). Microseismicity data forecast rupture area. *Nature*, *434*(7037), 1086–1086. https://doi.org/10.1038/4341086a

Schorlemmer, D., Wiemer, S., & Wyss, M. (2005). Variations in earthquake-size distribution across different stress regimes. *Nature*, *437*(7058), 539–542. https://doi.org/10.1038/nature04094

Serban, I., Klinger, T., Tesauro, G., Talamadupula, K., Zhou, B., Bengio, Y., & Courville, A. (2017). Multiresolution Recurrent Neural Networks: An Application to Dialogue Response Generation. *Proceedings of the AAAI Conference on Artificial Intelligence*, *31*(1). https://doi.org/10.1609/aaai.v31i1.10984

Shillington, D. J., Bécel, A., Nedimović, M. R., Kuehn, H., Webb, S. C., Abers, G. A., et al. (2015). Link between plate fabric, hydration and subduction zone seismicity in Alaska. *Nature Geoscience*, *8*(12), 961–964. https://doi.org/10.1038/ngeo2586

Shoji, D., Noguchi, R., Otsuki, S., & Hino, H. (2018). Classification of volcanic ash particles using a convolutional neural network and probability. *Scientific Reports*, *8*(1), 1–12. https://doi.org/10.1038/s41598-018-26200-2

Stevenson, A. J., Scholl, D. W., & Vallier, T. L. (1983). Tectonic and geologic implications of the Zodiac fan, Aleutian Abyssal Plain, northeast Pacific. *GSA Bulletin*, *94*(2), 259–273. https://doi.org/10.1130/0016-7606(1983)94<259:TAGIOT>2.0.CO;2

Suzuki, K., Nakano, M., Takahashi, N., Hori, T., Kamiya, S., Araki, E., et al. (2016). Synchronous changes in the seismicity rate and ocean-bottom hydrostatic pressures along the Nankai trough: A possible slow slip event detected by the Dense Oceanfloor Network system for Earthquakes and Tsunamis (DONET). *Tectonophysics*, *680*, 90–98. https://doi.org/10.1016/j.tecto.2016.05.012

Todd, E. K., & Schwartz, S. Y. (2016). Tectonic tremor along the northern Hikurangi Margin, New Zealand, between 2010 and 2015. *Journal of Geophysical Research: Solid Earth*, *121*(12), 8706–8719. https://doi.org/10.1002/2016JB013480

Todd, E. K., Schwartz, S. Y., Mochizuki, K., Wallace, L. M., Sheehan, A. F., Webb, S. C., et al. (2018). Earthquakes and Tremor Linked to Seamount Subduction During Shallow Slow Slip at the Hikurangi Margin, New Zealand. *Journal of Geophysical Research: Solid Earth*, *123*(8), 6769–6783. https://doi.org/10.1029/2018JB016136

Vallée, M., Nocquet, J.-M., Battaglia, J., Font, Y., Segovia, M., Régnier, M., et al. (2013). Intense interface seismicity triggered by a shallow slow slip event in the Central

Ecuador subduction zone. *Journal of Geophysical Research: Solid Earth*, *118*(6), 2965–2981. https://doi.org/10.1002/jgrb.50216

Wallace, L. M., Webb, S. C., Ito, Y., Mochizuki, K., Hino, R., Henrys, S., et al. (2016). Slow slip near the trench at the Hikurangi subduction zone, New Zealand. *Science*, *352*(6286), 701–704.

Wang, F., Wei, S. S., Ruppert, N. A., & Zhang, H. (2021). Seismic imaging of the Alaska Peninsula using the body-wave double-difference tomography. AGU. Retrieved from https://agu.confex.com/agu/fm21/meetingapp.cgi/Paper/903665

Wang, Q., Guo, Y., Yu, L., & Li, P. (2017). Earthquake Prediction based on Spatio-Temporal Data Mining: An LSTM Network Approach. *IEEE Transactions on Emerging Topics in Computing*, 1–1. https://doi.org/10.1109/TETC.2017.2699169

Warren-Smith, E., Fry, B., Wallace, L., Chon, E., Henrys, S., Sheehan, A., et al. (2019). Episodic stress and fluid pressure cycling in subducting oceanic crust during slow slip. *Nature Geoscience*, *12*(6), 475–481. https://doi.org/10.1038/s41561-019-0367-x

Watts, D. R., & Kontoyiannis, H. (1990). Deep-Ocean Bottom Pressure Measurement: Drift Removal and Performance. *Journal of Atmospheric and Oceanic Technology*, *7*(2), 296–306. https://doi.org/10.1175/1520-0426(1990)007<0296:DOBPMD>2.0.CO;2

Wech, A. G., Sheehan, A. F., Boese, C. M., Townend, J., Stern, T. A., & Collins, J. A. (2013). Tectonic Tremor Recorded by Ocean Bottom Seismometers.

Seismological Research Letters, *84*(5), 752–758. https://doi.org/10.1785/0220120184

Wech, Aaron G., & Creager, K. C. (2008). Automated detection and location of Cascadia tremor. *Geophysical Research Letters*, *35*(20). https://doi.org/10.1029/2008GL035458

Wei, M., McGuire, J. J., & Richardson, E. (2012). A slow slip event in the south central Alaska Subduction Zone and related seismicity anomaly. *Geophysical Research Letters*, *39*(15). https://doi.org/10.1029/2012GL052351

Wei, S. S., Ruprecht, P., Gable, S. L., Huggins, E. G., Ruppert, N., Gao, L., & Zhang, H. (2021). Along-strike variations in intermediate-depth seismicity and arc magmatism along the Alaska Peninsula. *Earth and Planetary Science Letters*, *563*, 116878. https://doi.org/10.1016/j.epsl.2021.116878

Wei, X., Shen, Y., Caplan-Auerbach, J., & Morgan, J. (2020). An improved earthquake catalog during the 2018 Kīlauea Volcano eruption from combined onshore and offshore seismic arrays. AGU. Retrieved from https://agu.confex.com/agu/fm20/meetingapp.cgi/Paper/689044

Wiszniowski, J., Plesiewicz, B. M., & Trojanowski, J. (2014). Application of real time recurrent neural network for detection of small natural earthquakes in Poland. *Acta Geophysica*, *62*(3), 469–485. https://doi.org/10.2478/s11600-013-0140-2

Withers, M., Aster, R., Young, C., Beiriger, J., Harris, M., Moore, S., & Trujillo, J. (1998). A comparison of select trigger algorithms for automated global seismic phase and event detection. *Bulletin of the Seismological Society of America*, *88*(1), 95–106. https://doi.org/10.1785/BSSA0880010095

Xiao, Z., Freymueller, J. T., Grapenthin, R., Elliott, J. L., Drooff, C., & Fusso, L. (2021). The deep Shumagin gap filled: Kinematic rupture model and slip budget analysis of the 2020 Mw 7.8 Simeonof earthquake constrained by GNSS, global seismic waveforms, and floating InSAR. *Earth and Planetary Science Letters*, *576*, 117241. https://doi.org/10.1016/j.epsl.2021.117241

Yarce, J., Sheehan, A. F., Nakai, J. S., Schwartz, S. Y., Mochizuki, K., Savage, M. K., et al. (2019). Seismicity at the Northern Hikurangi Margin, New Zealand, and Investigation of the Potential Spatial and Temporal Relationships With a Shallow Slow Slip Event. *Journal of Geophysical Research: Solid Earth*, *124*(5), 4751–4766. https://doi.org/10.1029/2018JB017211

Ye, L., Lay, T., Kanamori, H., Yamazaki, Y., & Cheung, K. F. (2021). The 22 July 2020 MW 7.8 Shumagin seismic gap earthquake: Partial rupture of a weakly coupled megathrust. *Earth and Planetary Science Letters*, *562*, 116879. https://doi.org/10.1016/j.epsl.2021.116879

Zhu, W., & Beroza, G. C. (2019). PhaseNet: a deep-neural-network-based seismic arrival-time picking method. *Geophysical Journal International*, *216*(1), 261–273. https://doi.org/10.1093/gji/ggy423

CHAPTER 2

MANUSCRIPT 2

A shallow slow slip event preceded the 2021 Mw8.2 Chignik earthquake in east-central Alaska

Authors: Bing He[1]*, XiaoZhuo Wei[1], Meng (Matt) Wei[1]*, Yang Shen[1], Marco Alvarez[2], Susan Schwartz[3]

Affiliations:

[1]Graduate School of Oceanography, University of Rhode Island

[2]Department of Computer Science and Statistics, University of Rhode Island

[3]Earth and Planetary Sciences Department, University of California, Santa Cruz

Corresponding authors: Bing He (bing-he@uri.edu), Meng Wei (matt-wei@uri.edu)

submitted to *Science Advance*

Abstract

Slow slip events (SSEs) have been discovered at shallow depth near the trench in some subduction zones and have been linked to the triggering of large earthquakes and absence of tsunamis. These shallow SSEs are invariably submarine, making it difficult to observe their temporal and spatial extent. Here, we report a shallow SSE in late 2018 in east-central Alaska, up-dip of and preceding the Mw 8.2 Chignik earthquake on July 29th, 2021. The SSE was detected in data from an offshore array of seafloor pressure gauges by a machine learning method. This detection is supported by the spatial pattern of simulated SSE deformation, the increased seismicity after SSE at the positive Coulomb stress change area, and the absence of a sizeable tsunami following the Chignik earthquake. Our method has the potential to transform the way offshore SSEs are detected and to improve tsunami hazard assessment in subduction zones.

Teaser

Machine learning is used to tease out tectonic signals from seafloor pressure data, improving understanding of great earthquakes and tsunamis.

2.1 Introduction

Slow slip events (SSEs) have recently been discovered at shallow depth on the plate interface in some subduction zones, including Costa Rica and New Zealand (Araki et al., 2017; Davis et al., 2015, p. 2; Dixon et al., 2014; Saffer & Wallace, 2015; Wallace et al., 2016). These shallow SSEs may be linked to tsunamigenic earthquakes and the triggering of large interplate earthquakes (Hino et al., 2014; Ito et al., 2013b; Saffer & Wallace, 2015).

SSEs likely play an important but as yet unresolved role in the accommodation of plate motion near the trench at many subduction zones. Detailed observations of slip during SSEs are critical to understanding the distribution of locking on subduction faults offshore which determines the potential seismic and tsunami hazard posed by subduction zones (Lindsey et al., 2021). However, it is challenging to detect and measure shallow SSEs because the standard GNSS systems for measuring land displacement do not operate under water. Seafloor pressure gauges, which detect SSEs by observing pressure changes due to vertical displacement of the seafloor, currently provide the only viable way to continuously observe and spatially map out displacements during an SSE (Ito et al., 2013b; Ruiz et al., 2014; Wallace et al., 2016). The challenge is that the oceanic noise is comparable to the tectonic signal in seafloor pressure data and only very large SSEs with several centimeters of seafloor displacement can be observed.

Recently, we developed a machine learning method to detect small shallow SSEs in seafloor pressure data (He et al., 2020). We have applied this method to data in New Zealand between 2014 and 2015 and detected five events, two of which are confirmed by the onshore GPS records. We also have shown that our method performs better than the traditional matched filter method (He et al., 2020). Here, we improved the method by adding the capability of detecting not only seafloor uplift but also subsidence. We applied this improved method to the seafloor pressure data collected in the Alaska Amphibious Community Seismic Experiment (AACSE) (Figure 2.1). The spatial pattern of the vertical deformation in late October 2018 is consistent with an SSE. The occurrence of an SSE is also supported by seismicity patterns around the event and the lack of tsunami after the

2021 Mw 8.2 Chignik earthquake. The SSE preceded the 2021 Chignik earthquake and likely increased the Coulomb stress in the rupture area of the 2021 earthquake by 0.2 bar. The unique geological structure on the seafloor might create the geophysical condition for SSEs in this area.

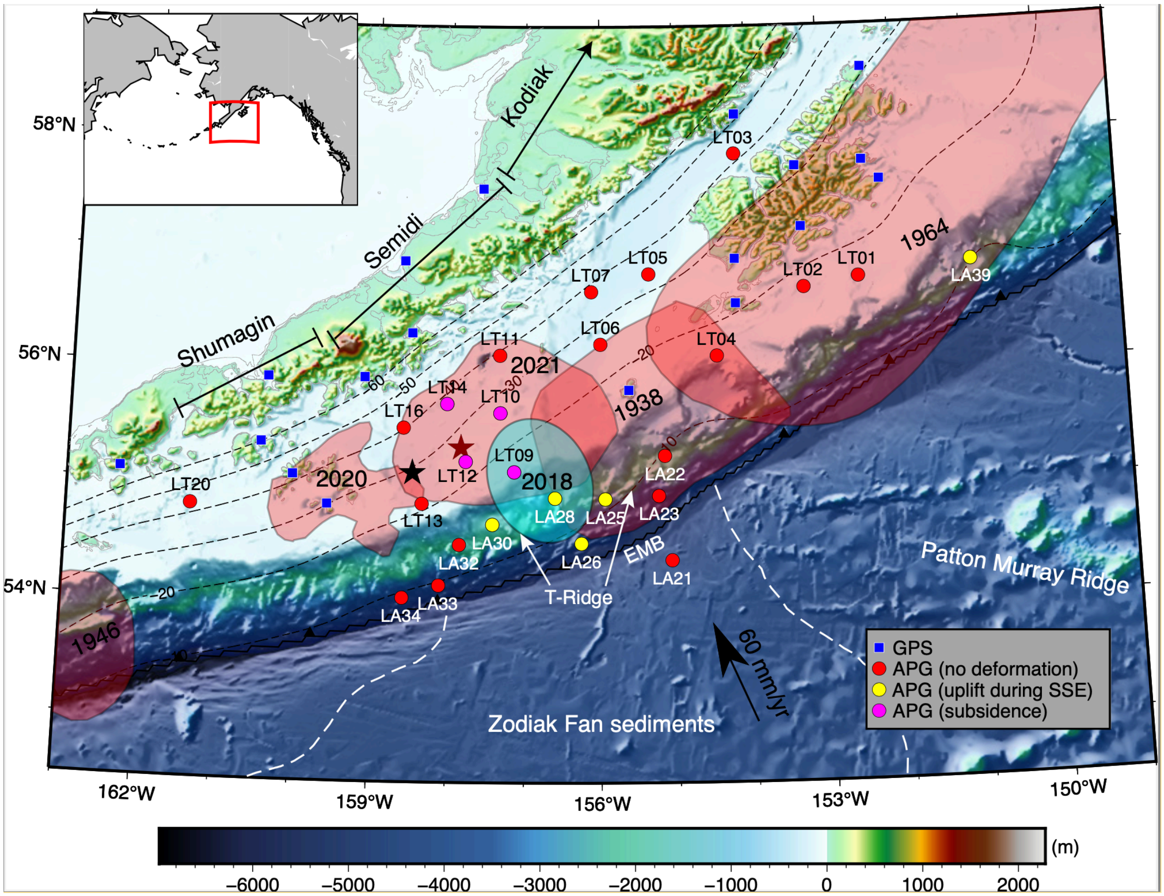

Fig. 2.1. *Map of the study area in the Alaska-Aleutian megathrust (the red box in the small inset on the top left). Red, magenta, and yellow circles represent absolute pressure gauges (APGs) in AACSE. The dashed black lines indicate the slab depth contours with a 10 km interval from Slab2 (Hayes et al, 2018). The red shaded areas are the historical earthquake distributions. The 1938 Mw8.3 earthquake is shown in 1 m slip contours from the best fitting model in Freymueller et al., (2021). The 2020 Mw7.8 earthquake is shown in the 50-*

cm slip contours (Crowell & Melgar, 2020). The 2021 Mw8.2 earthquake is from the USGS inversion results and shown in 1-m slip contours. The black and red stars label the epicenters of the 2020 Simeonof earthquake and 2021 Chignik earthquake, respectively. The cyan shaded area is our preferred 2018 SSE area. The white dashed lines show the area covered by Zodiak Fan sediments. T-ridge represents the transitional ridge or escapement terminating the transitional zone. EMB means the embayment into the Semidi deformation front (Huene et al., 2016).

Earthquakes and SSEs in Alaska

The Alaskan subduction zone is caused by the Pacific plate subducting beneath the North American Plate. There are three segments in the study region which show diverse slip behaviors, incoming plate structures, and hydration levels (S. Li & Freymueller, 2018; S. S. Wei et al., 2021). In the west, the Shumagin segment shows a low degree of seismic locking, called the Shumagin gap (Davies et al., 1981), which has abundant seismicity but lacks large earthquakes attributed to the rough surface of the subducted plate (Shillington et al., 2015). The 2020 Mw7.8 earthquake is the largest on the eastern Shumagin gap since 1917 (Crowell & Melgar, 2020). No shallow slip was released by this earthquake and its aftershocks and most slip was at depths from 20 km to 45 km (Liu et al., 2020; Xiao et al., 2021; Ye et al., 2021). The Semidi segment is in the middle of the Shumagin and Kodiak segment and can host large earthquakes with a magnitude of 8 every 50 to 75 years (Davies et al., 1981). The last two events are the 1938 M8.3 earthquake and the 2021 Mw8.2 Chignik earthquake. There is no seismic slip model for the 1938 earthquake, but an aftershock zone extended ~270-300 km along strike and a tsunami model shows large slip concentrated at shallow depth (< 20 km) (Davies et al., 1981; Freymueller et al., 2021). The 2021 earthquake had about half of its slip overlapping with the 1938 earthquake rupture with most slip occurring below 20 km depth. The Semidi segment is characterized as mid-locking, with more sediments subducted and smoother than Shumagin (J. Li et al., 2015; S. Li & Freymueller, 2018; Shillington et al., 2015). The Kodiak segment shows high locking and has the most active seismicity at all depths (S. Li & Freymueller, 2018; S. S. Wei et al., 2021). The Kodiak segment and eastward hosted the largest digitally recorded M 9.2 earthquake in the world. The systematic along-strike variations provide an excellent opportunity to explore the relationship between earthquake behavior and geological/geophysical setting.

In both the Upper and Lower Cook Inlets, in south-central Alaska, long-term SSEs with durations of a couple of years and intervals of decades occurred in the last ten years. Although the duration, interval, and magnitude of these SSEs vary from event to event, these SSEs occur at a depth of around 40 km to 60 km, which coincides with the down-dip limit of megathrust earthquakes (S. Li et al., 2016; M. Wei et al., 2012). However, no SSEs have been reported at the up-dip end of the seismogenic zone, mostly due to the fact that the Alaskan islands are far from the trench and there are no seafloor geodetic observations. The large community-based seafloor seismometer and pressure gauge deployment of AACSE in Alaska-Aleutian subduction margin allows us to detect shallow SSEs in this area.

2.2 Materials and Methods

AACSE pressure data preprocessing

Between May 2018 and August 2019, the Alaska Amphibious Community Seismic Project (AACSE) deployed 75 broad-band ocean-bottom seismometers (OBSs) and 30 broad-band land seismometers on the southern Alaskan subduction margin, aiming to study tectonics, structure, and seismic activities (Barcheck et al., 2020) (Fig. 2.2). 34 of the OBSs were equipped with absolute pressure gauges (APGs). Among the 34 APGs, only 15 shallow-water depth stations (depth < 300-m) and 11 deep-water depth stations (depth > 1500-m) have data stored by IRIS, which we used in this study (Fig. 2.1). The pressure data of stations LA26, LT02, and LT09 were shorter than others because of discontinuity. The sampling rate of raw data is 120 Hz, and we downsampled the data to a half-hour per sampling point for further processing because we were not interested in the high-frequency content.

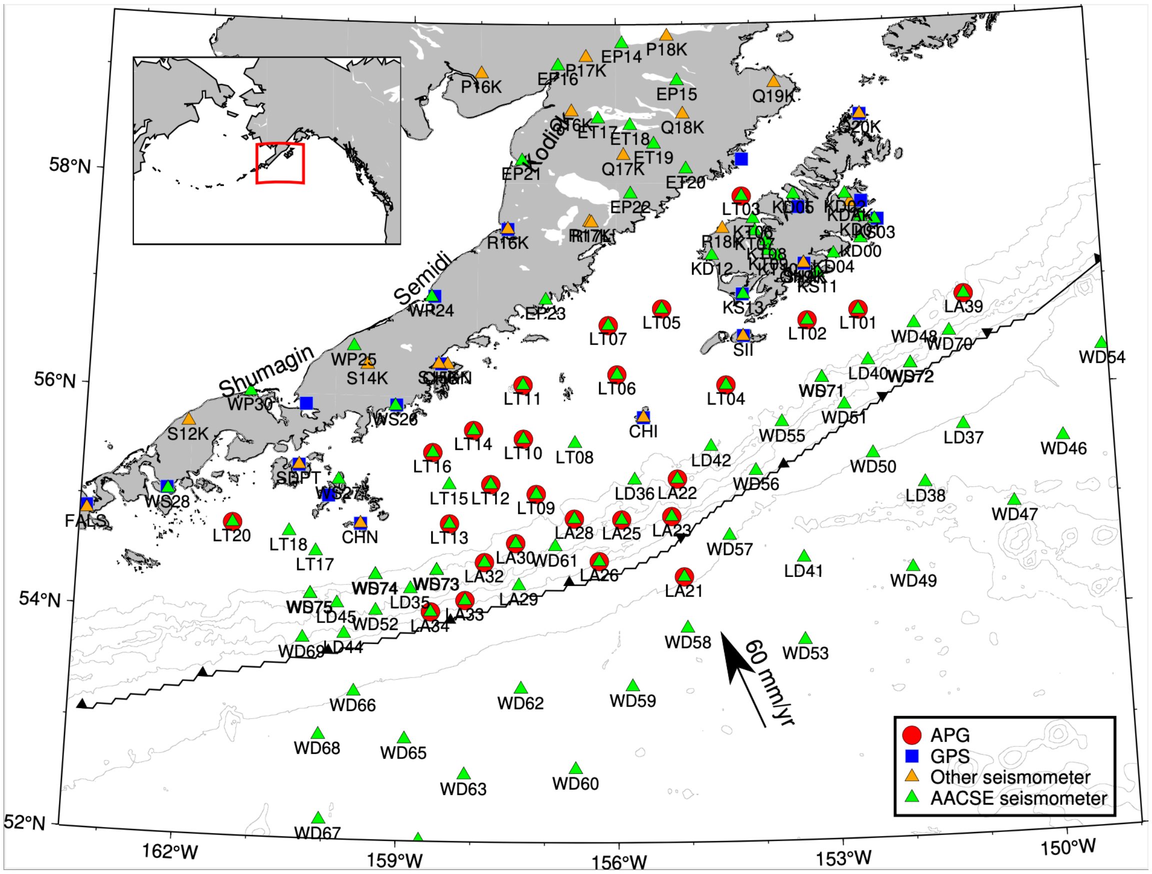

Fig. 2.2. *Map of the study region with locations of seismic stations used in the analysis. Pressure and GPS stations are also shown here.*

We processed the seafloor pressure data in three steps: de-tiding, de-drifting, and removing oceanographic signals. First, we removed tides using tidal response analysis (Munk et al., 1966) (Fig. 2.3a). Second, we used an improved method to remove the sensor drift. Pressure sensor drift is a gradual sensor degradation, which is traditionally estimated using an exponential plus linear curve (Watts & Kontoyiannis, 1990). However, we found that the conventional method will over-estimate the drift by including long-period ocean signals. Therefore, we modified the conventional method with the help of the ocean circulation model, HYCOM, which can reasonably predict the long-period ocean waves. We first subtracted the low pass filtered (fourth-order Butterworth filter with 20 days) HYCOM data from the de-tided pressure data, and then we used the conventional method to remove the drift. Then, we added the HYCOM data back to the de-drifted pressure data (Fig. 2.3b). The new de-drifted data show a higher correlation coefficient with HYCOM data than the conventional method (Fig. 2.3cd and Fig. 2.4). Our new de-drifting approach can remove the drift without affecting the long-period ocean waves.

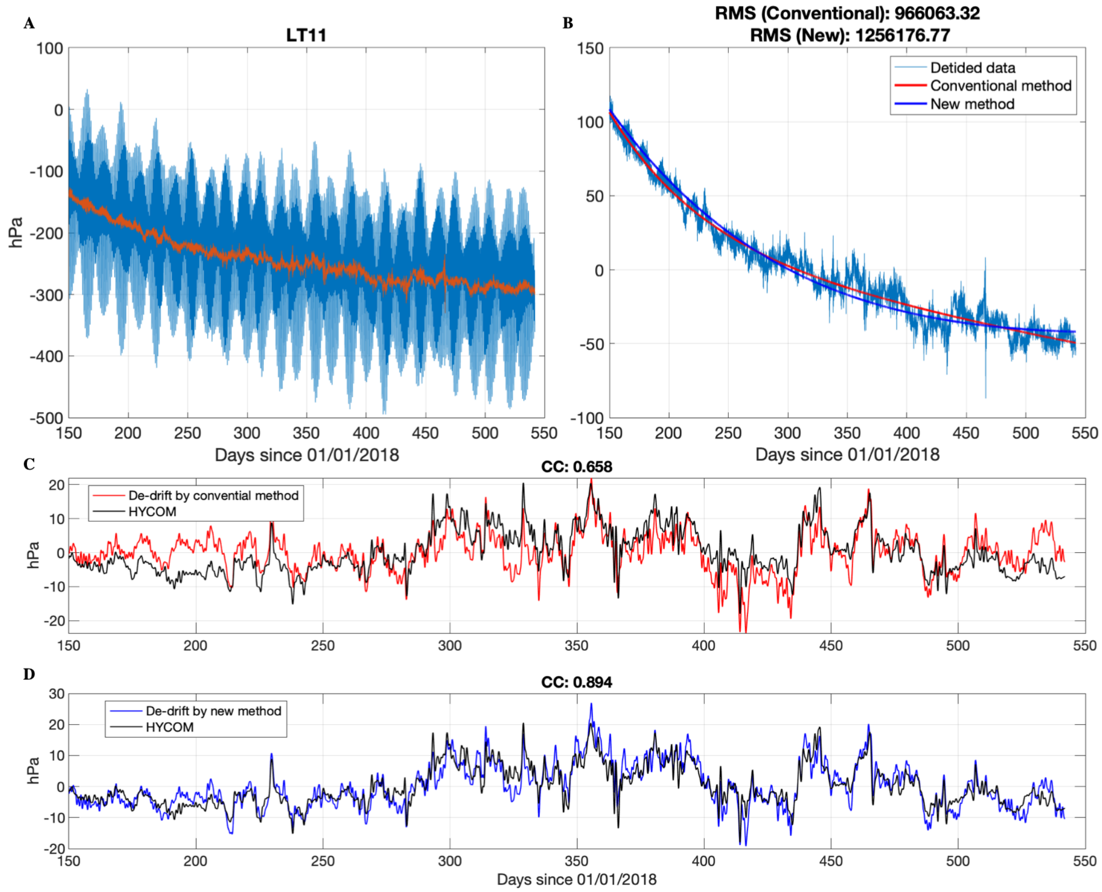

Fig. 2.3. *De-tide process. (a). De-tiding process. (b). De-drifting process by two methods. Conventional method means de-drift by exponential plus linear curve. New method is subtracting the HYCOM data first, and then removing drift using the conventional method. (c)(d). The comparisons between HYCOM data and different de-drited data. CC means the correlation coefficient.*

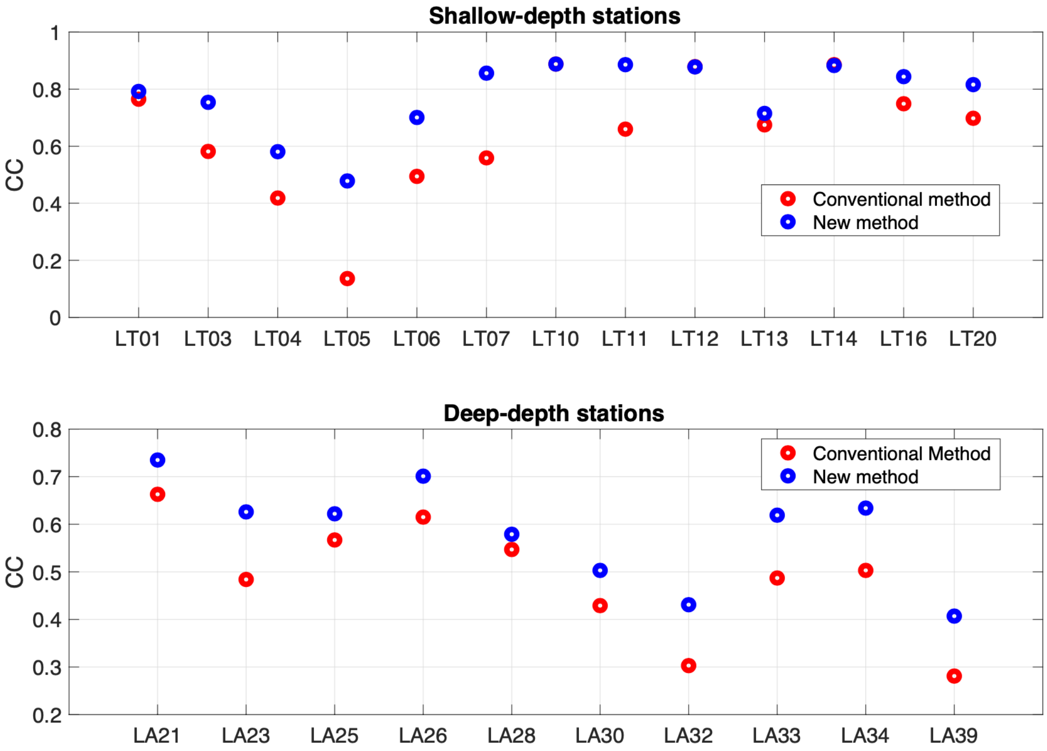

Fig. 2.4. *The correlation coefficients between HYCOM data and different de-drifting data.*

Third, we removed oceanographic noise by an ocean circulation model and reference station method. The deep ocean system is relatively quiet and is mainly affected by the upper water column movement. The eddies in the deep ocean can reach lateral scales of several hundreds of kilometers and larger. We thus assumed most deep-water stations are affected by identical deep eddy flows and chose station LA21 on the other side of the trench as the reference station. We subtracted the reference station from other deep-water stations.

There are 15 shallow water stations on the continental shelf. The seafloor pressures at shallow-water stations are primarily affected by wind forcing and atmospheric pressure loading. The pressure variations at the shallow-depth stations are two to three times larger than that at the deep-depth stations. The shallow-depth pressures have the same period of ocean waves but various amplitudes. If we choose one shallow-water station as the reference and subtract the reference, some oceanographic signals would be left or over-subtracted by the reference station. Therefore, we used ocean circulation models to remove the oceanographic signals. The ocean circulation models commonly provide daily output, so we removed the high-frequency pressure data using a 1-day low pass filter. Fig. S5A shows the shallow-water comparison between the real seafloor pressure data and one ocean circulation model, HYCOM. Furthermore, we found there are some oceanic waves left in the deep-water residuals. We further subtract the model pressure difference from the deep-water residuals. Fig. 2.5.B shows the deep-water residual comparison.

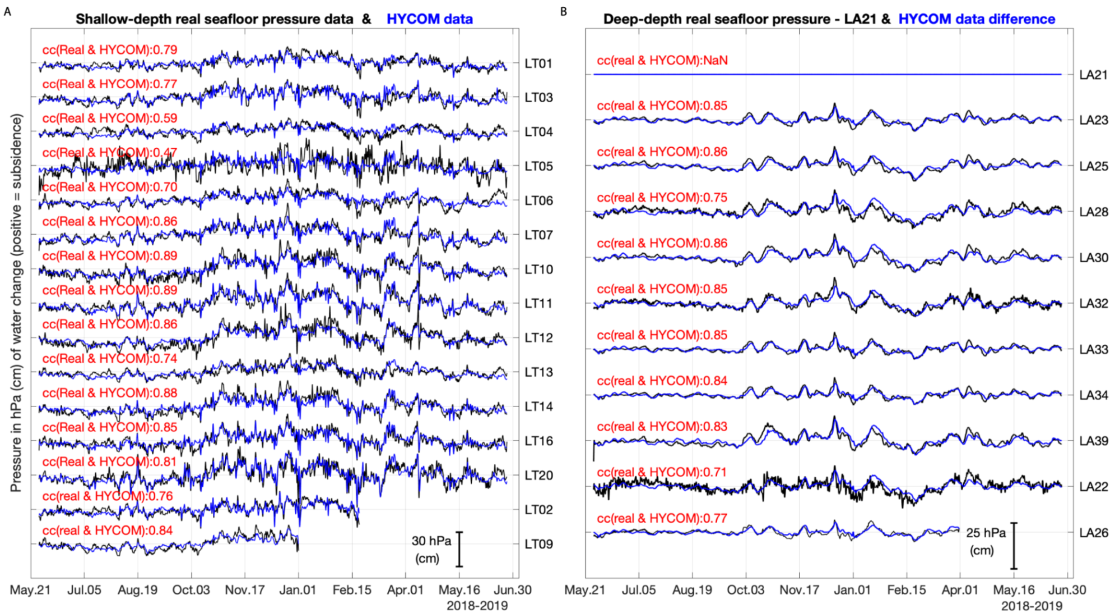

Fig. 2.5. *The comparison between real seafloor pressure data and HYCOM. For deep-depth pressure data, we used pressure difference data to have the better comparison.*

We calculated the variance reduction (VR) to describe how much oceanographic signals can be removed in seafloor pressure data (Fig. 2.6). $VR = \frac{1-(Variance(Real-HYCOM))}{Variance\ (Real)}$. For shallow-water stations, besides the very noisy station LT05, the average correlation coefficient (CC) between the real seafloor pressure and HYOM output is 0.80. The average VR is 0.64. For deep-water stations, the average CC is 0.82, and the average VR is 0.70. We also tried different low pass filters for one to ten days in HYCOM pressure data, and the result did not improve. The variance reductions in this study are comparable with the results in New Zealand (Muramoto et al., 2019), even though the station spacing in Alaska is sparse. By calculating the difference between the HYCOM and pressure data, we reduced the variance of the pressure data to a few centimeters equivalent without affecting the tectonic signal. This pressure difference is the data we put into the machine learning detector.

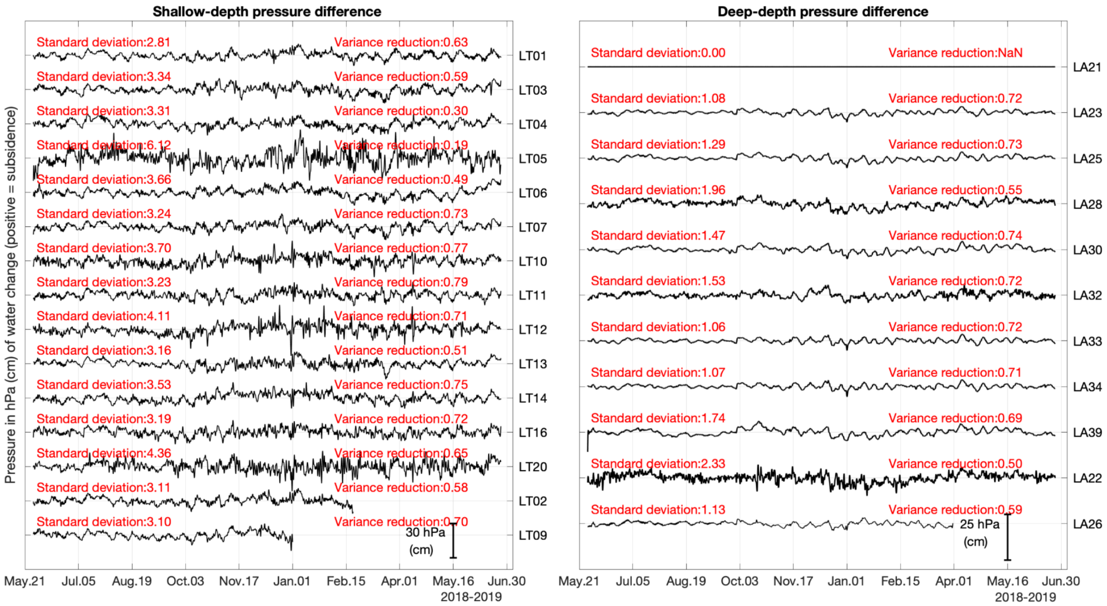

Fig. 2.6. *The pressure difference between real seafloor pressure data and HYCOM data. The standard deviation and variance reduction for each data are labeled in the figure.*

There are many ways to remove the oceanographic noise in the seafloor pressure data, such as numerical circulation models (HYCOM, ECCO4, ROMs), global mean, isobath average, temperature and pressure correlation, and reference station method (Fredrickson et al., 2019; Gomberg et al., 2019; Hino et al., 2014; Inazu et al., 2012; Wallace et al., 2016). Each one has its own strengths and disadvantages. In this study, we used the HYCOM because HYCOM simulates the observation better than others (Dobashi & Inazu, 2021). Compared to the correlation relations, we also found that HYCOM performs better on the continental shelf than on the steep continental slope because of the rapid water movements. Therefore, we further remove the oceanographic noise in the continental slope by the reference station method. Besides, HYCOM has a spatial resolution of 1/12 degrees, which is much better than ECCO4, which has a spatial resolution of .5 degrees. The stations located at the same isobath have similar oceanographic contributions. The correlation coefficient can be over 90% in Alaska, while the correlation coefficient of the stations distributed at the different isobath decreases from 90% to 60% along the slope. The global mean and reference station method is unsuitable for a large area, such as AACSE. Removing the average isobath method is hard to keep two stations at the same isobath with various geodetic signals. The subtraction between them may further subtract the geodetic signals. In addition, we check the bottom temperature data with APGs, and they are not very well recovered.

SSE detection with machine learning

We built a deep learning model to detect the approximate time of SSE in the pressure records. The basic procedure is the same as in our previous study (He et al., 2020). We added the capability of detecting subsidence. Because real seafloor pressure data is limited and insufficient, we used synthetic data to train the machine learning model (detector). The synthetic data has a spectrum similar to the real data and contains the expected SSE signals with random duration, amplitude, and timing. Then we evaluated the model performance and applied the trained model to the real data.

The synthetic data consists of three components: stochastic noise data with a pinkish-red spectrum, linear drifts with random amplitude, and artificial SSE ramps (Fig. 2.7). This study is improved by including up-ramp and down-ramp synthetic SSE signals, representing the subsidence and uplift in the pressure. The total number of synthetic training data is 0.56 million. We trained the machine learning model on synthetic data with a 3-5 dB signal-to-noise ratio. It means that if the standard deviation of background pressure is 1 hPa (1 cm), the aimed amplitude of SSE is 2.5-4.3 cm. In this study, the standard deviation of each piece of data ranges from ~1-4 dB so that the target amplitude can be 2.5 to 17.2 cm. Other parameter settings are the same as in our previous study (He et al., 2020).

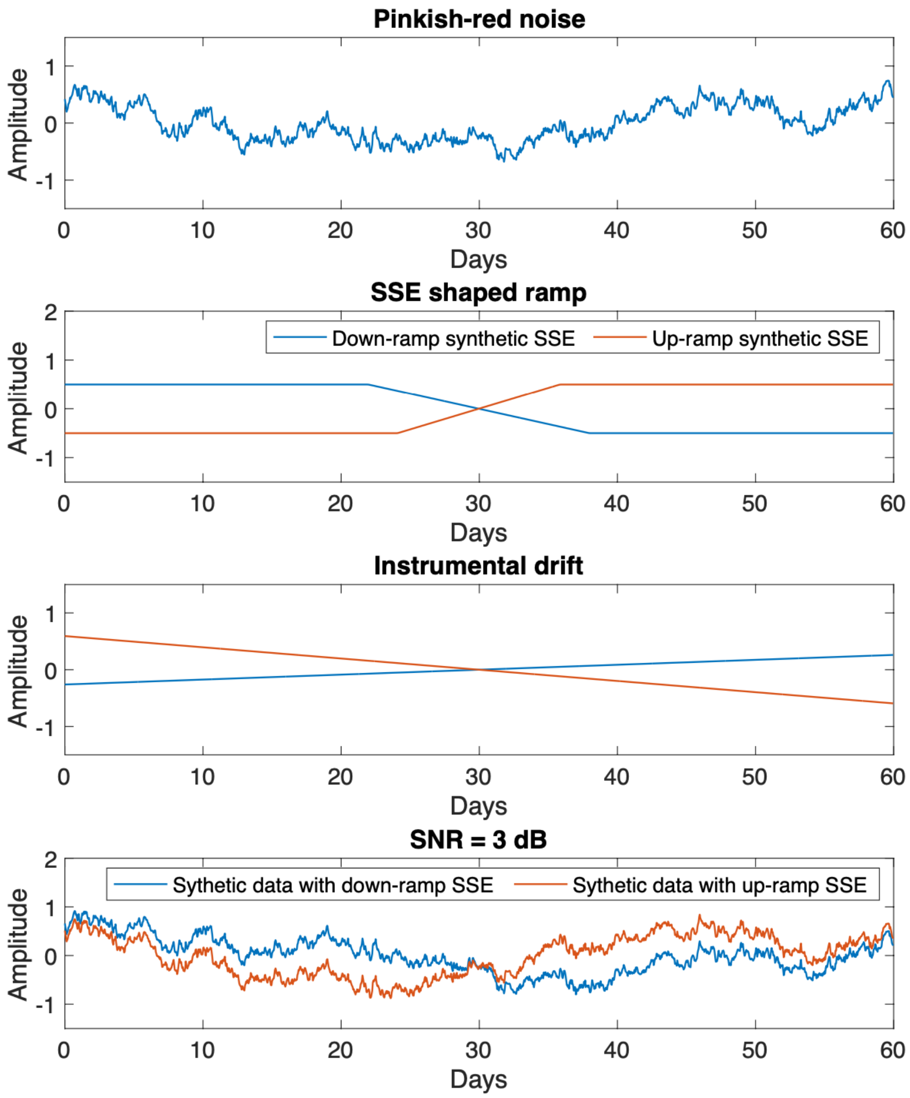

***Fig. 2.7**. A case shows how the synthetic data is constructed. The SNR for this case is 3 dB. The synthetic data (d) is the combination of pinkish-red noise (a), up-ramp and down-ramp synthetic SSE (b), and instrumental drifts (c). When the SSE occurs, the continental plate moves upward close to the trench and moves downward far away to the trench. The pressure close to the trench decreases, so the ramp is down. The pressure far away to the trench increases, so the ramp is up.*

The deep learning model includes convolutional and recurrent neural networks, which can extract and study the long and short-term patterns in time series data (Fig. 2.8). The input is a piece of 60-days normalized pressure difference data from one station. The final layer of the network outputs a vector of probabilities of uplift, subsidence, and no SSE (Fig. 2.8). The trained model accuracy reaches 80% on synthetic data (Fig. 2.9).

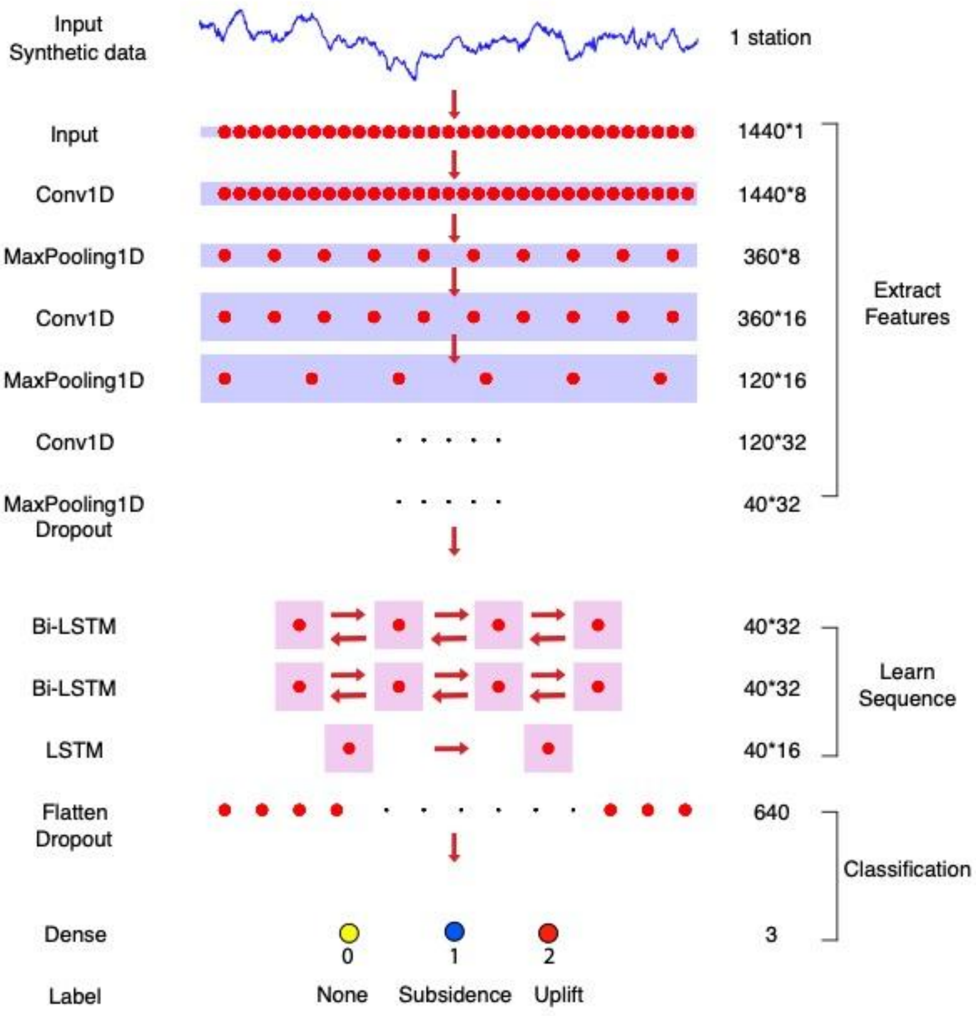

Fig. 2.8. *The architecture of the machine learning method. Left labels are the function names in Keras. They are 1-D convolutional layer, 1-D max pooling layer, bilateral long and short term memory layer, flatten, dense and dropout layers. Right numbers are the*

rows and columns in each layer. The hyperparameters are chosen based on many random tests.

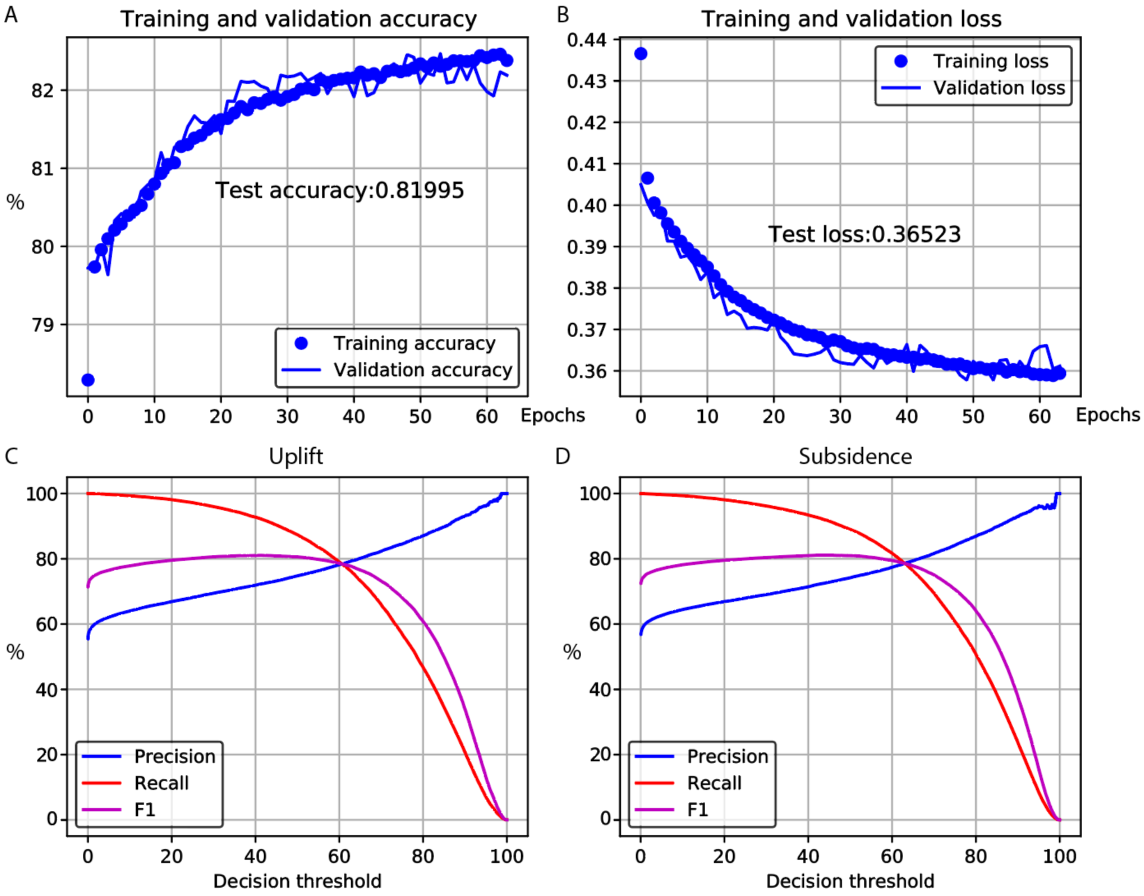

Fig. 2.9. *The training performance. (a)(b). The accuracy and Loss change with epochs. (c)(d). The key performance indicators change with the decision threshold. We chose 0.6 as the detection threshold in figure 2.11.*

In order to make sure our detected SSE is not due to oceanographic sources, we run the machine learning detectors on HYCOM data as well. HYCOM data from 2010 to 2019 were used in this region. We calculated the seafloor pressure by integrating the temperature and salinity from the upper water column and sea surface height. To resemble the real data processing steps, we subtracted the global mean from the shallow-water (0-500 m) and

(500–4500 m) deep-water stations. We put the pressure residuals of each station into the machine learning detector. The detector indeed finds some subsidence and uplifts (Movie. 2.1). For example, stations located closely are able to show identical signals because some common waves are left in the pressure residuals. Also, one or two stations can show the signals together due to the noises or small eddies. However, we did not find a single case with multiple stations showing a similar pattern in our detected SSE. Therefore, from a statistical point of view, our SSE pattern is not likely result from an oceanographic process.

SSE simulation

We simulated the surface displacement caused by an SSE using a kinematic model. We first built a realistic three-dimensional geometry in Alaska using the slab 2.0 model (Hayes et al., 2018). Then we prescribed an initial slip model on the fault plane. The prescribed slip model should be chosen as simply as possible, so we decided on an oval slip patch on the fault with two radii of 65 km and 50 km and nonuniform slip of 10 to 15 cm. The moment magnitude of the simulated SSE is around 6.8. Next, we set the material properties based on the one-dimensional Alaska velocity model (Table 2). Finally, we tested models at different locations to compare the observations.

Table 2.1 *The Southern Alaska (SCAK) velocity model used to locate the earthquakes.*

Depth (km)	Vp (km/s)	Vs (km/s)
-4.0	5.30	2.974
4.0	5.60	3.140
10.0	6.20	3.480
15.0	6.90	3.870

20.0	7.40	4.150
25.0	7.70	4.325
33.0	7.90	4.430
47.0	8.10	4.550
65.0	8.30	4.655

Earthquake detection

In order to better observe the relationship between SSEs with seismicity, we built a more detailed earthquake catalog for the entire study region. In addition to the AACSE seismic data, we also used seismic data from the National Tsunami Warning Center Alaska Seismic Network (network code: AT), the Alaska Regional Network (network code: AK), the Global Seismograph Network (network code: II), the Transportable Array (network code: TA), and the Alaska Volcano Observatory Network (network code: AV). However, only those broadband stations within a 4.4-degree distance from 55.258N, 155.8625W were used.

The procedure of the catalog building is as follows. First, a recursive short-time-average/long-time-average (STA/LTA) algorithm (Withers et al., 1998) is used to detect possible earthquake records on individual seismometer channels with a trigger threshold of 5, after filtering the data between 2 and 10 Hz. The STA window length was set to 2 s, while the LTA window length was set to 10 s. Then, the detection windows on different stations were associated with different events based on P-wave and S-wave coda traveling speeds of 10 and 4 km/s. The values were set slightly larger to accommodate the large interstation distance of the array. A kurtosis-based automatic phase picker was used to pick

P- and S-wave arrivals (Baillard et al., 2013; Ross et al., 2016). Some of the OBSs suffered from instrumental malfunctions (Barcheck et al., 2020), and we discarded the channels with no records. A particle motion filter was applied on the remaining three-component data to automatically separate P- and S-waves (Ross et al., 2016). The Nonlinloc package was used to determine the earthquake locations (Lomax et al., 2000) in a spherical earth, using the travel times calculated by TauP (Crotwell et al., 1999). The phase picks with large misfits were down-weighted while searching for the optimized earthquake locations. We used the Southern Alaska 1D velocity model, also called SCAK model (**Table 2**) for the earthquake localization, despite the fact that Alaska is a region with strong lateral structure variations and the Alaska Earthquake Center actually used several different 1D velocity models for the events in our study area (Personal communication with Natalia Ruppert from Alaska earthquake center). The possible SSE region is just located on the boundary between the two model areas, but our stations in the north were in the center of Southern Alaska. The usage of the SCAK model, rather than other models, could avoid causing large misfits for the distant stations. Besides, we could eliminate the location inconsistencies that different velocity models might cause by applying only one velocity model. An example of an earthquake in the SSE region detected by our method but not in the USGS catalog is shown in Fig. 2-10. This event has one of the least recording station numbers, compared with other events in the same region.

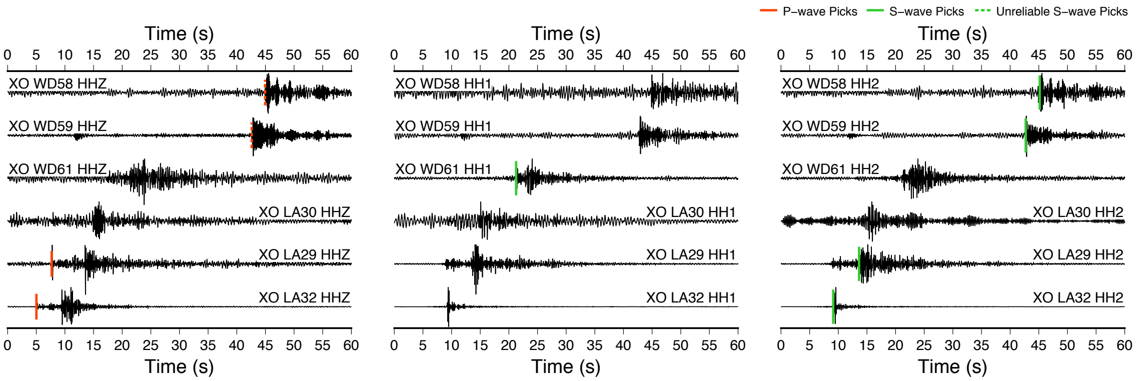

Fig. 2-10. *Earthquake examples. An example of a new M_L 2.99 earthquake detected and located in our catalog, in the SSE region, which is not in the USGS catalog. Its origin time is 2018-11-11T14:13:43.854265 (UTC), and the source location is 54.438010N, 158.023437W at the depth of 37.6979177 km. The red and green vertical bars represent our picked P- and S-wave arrivals. The dashed vertical bars indicate the down-weighted picks during the localization. Each trace is normalized by its maximum value.*

After the earthquakes were located, we launched a re-association process for the events to better constrain their locations. The re-association method is described by (X. Wei) et al., 2020. We used a new set of STA and LTA window lengths, which were half of the original values, to re-detect the possible recorded earthquakes. Accordingly, the trigger threshold was lowered to 3. The STA/LTA parameters update helped find more earthquake records on distant stations with lower signal-to-noise ratios (SNRs). However, only bringing these lower SNR records in the re-association process could avoid raising the false detections considerably. For the re-associated events, their phase arrivals were picked, and their source locations were determined following the same procedure after the association process. Finally, for every single event, we measured their local magnitudes (Richter, 1936).

Tremor detection

An SSE is usually associated with tremors occurring at the updip and downdip part of the seismogenic zone (Beroza & Ide, 2011). Therefore, we investigated the tremors around the SSE location. The tremor detection method incorporated the automated envelope cross-correlation technique (Aaron G. Wech & Creager, 2008). Because our target region is the Semidi segment, we choose the seismic stations within a circle with (-157, 55) as the center and 3 degrees as the radius. This tremor detection region includes 46 inland and offshore seismic stations. Two horizontal components of waveforms are used because tremor is generally dominated by S waves (Ide, 2012). To obtain the better envelope cross-correlation results, two different frequency bands were applied (Todd et al., 2018; Todd & Schwartz, 2016): (1) 2-8 Hz to isolate tremor with low frequencies and (2) 10-16 Hz to separate local earthquakes with energy from high frequencies. The two bandpass filtered data envelopes were calculated, and then low pass filtered to 0.2 Hz and downsampled to 1 Hz for use in the envelope cross-correlation.

The continuous records are split into half overlapping 3-minute windows. First, we quickly removed large-amplitude earthquakes and large spikes, which affect cross-correlation results from each window, by using the method in Chen et al., (2018). The amplitude is simplified to 1 or 0 if higher or lower than the average value. If the segments are less than 10 or the total length proportion of segments is less than 30%, this window is considered to have a large amplitude of earthquakes or large spikes and removed. Second, we calculated the envelope cross-correlation in different frequency bands. Because of the relatively sparse stations in AACSE, the criteria for tremor detection is lower than in other studies (Chen et al., 2018; Todd et al., 2018). We used a hierarchical cluster method to find the most correlated station pairs. The tremor is located if the cross-correlation is over 0.68 for more than 3 station pairs, but the time window is skipped if the cross-correlation is over 0.65 for at least 6 stations in 10-16 Hz to minimize the local earthquake detections. Third, some regional or teleseismic waves are not shown in the high-frequency band We chose four reference stations (EP22, WD53, LT20, WD67) outside the study region and filtered them to 2-8 Hz, enveloped and downsampled. When the cross-correlation is over 0.65 for at least four stations, including the reference station, that time window is discarded. Fourth, we have USGS and our own seismic catalogs. We eliminated the detection time window that includes earthquakes in the catalogs. These automated processes help to reduce the number of false tremor detections significantly. Finally, we visually inspected all the detection results and abandoned small tremors with durations less than 30 s. Besides, we checked three seismic and hydrophone components to avoid T-phase in the seismic data. We also tested another frequency band pair of 4-10 Hz and 12-18 Hz used in New Zealand tremor detection (Todd et al., 2018). The results do not improve.

2.3 Results

SSE detection

We applied our machine learning detector trained by synthetic data (He et al., 2020) to the processed AACSE pressure data. The pressure time series is split into 60-day sliding windows with 1-day sliding increments and each piece of 60-day data is normalized by its standard deviation. We apply the machine learning detector to the data and the detector calculates the probability of subsidence or uplift in the middle part of the data. A probability of plus one or minus one indicates the highest probability that the 60-day segment contains an SSE, corresponding to an uplift or subsidence of the seafloor, respectively. According to the machine learning threshold test, we chose ±0.6 as the decision threshold. The detector defines an SSE when the absolute value of the probability is over 0.6. All the predicted probabilities are organized into the time series shown in Fig. 2.11. B. In addition, we have a movie to show the spatial distribution of the detected results (Movie 2.2).

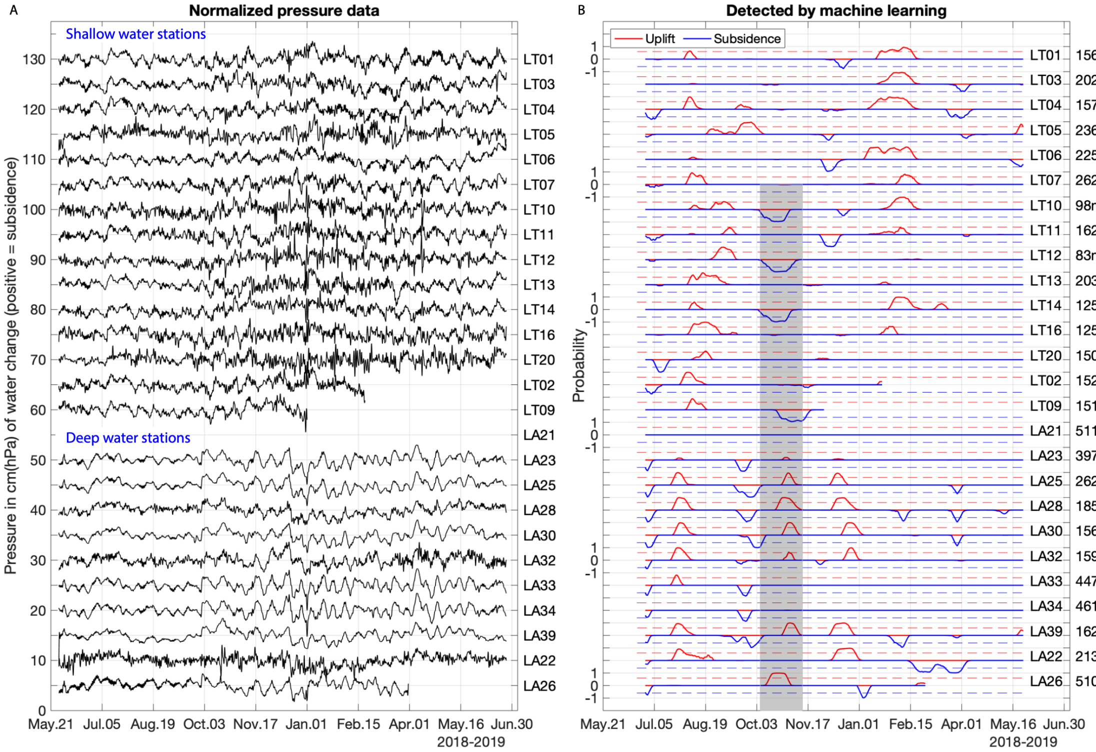

Fig. 2.11. *Normalized pressure data and machine learning detection results. (A). Shallow-water and deep-water normalized pressure data. (B). Detected probabilities from each station. All the detected probabilities (red and blue) vary within ±1. Red and blue dashed lines represent the detection thresholds of ±0.6, respectively. Only the probabilities over the thresholds are considered as an uplift or subsidence signal.*

The detection results show four types of spatial patterns. The first is where most stations show the same trend over a short time range. An example of this pattern is evident around June and July 2018, when over half of the stations show an apparent subsidence signal (Fig. 2.11 B & 2.12 A). This pattern is common in our detections, and the large distance of spatially coherent signals (several hundreds of kilometers) is likely caused by large-scale ocean circulations that have not been fully eliminated by our date processing. A second common pattern is where only one station shows a noticeable uplift or subsidence signal, such as the uplift of station LT05 on Sept. 20, 2018 (Fig. 2.11 B). This is most likely due to small oceanographic signals or instrumental noise from a specific location or station. A third pattern (Figure 2.12 B) shows three uplifting stations close to the trench and two subsiding stations at a similar location along strike but far from the trench. This pattern appears to be consistent with SSE motion because of its spatial pattern (Fig. 2.12 B). However, there is a gap between the uplifted and subsided stations due to a lack of stations between the two groups. Some adjacent stations do not show the same pattern, such as LA23 and LT07 (Fig. 2.12 B). In addition, oceanographic signals commonly produce similar motions at stations located at the same isobaths (Fredrickson et al., 2019). The uplifting stations LA22, LA25, and LA28 are from identical depths while subsiding station LT11 and LT06 are at close depths (Fig. 2.13 B). There is a GPS station, AC13, between the positive and negative stations. There is no evidence for an SSE that generated displacement over 3 cm. This pattern can be explained by the coincidence of two localized eddy flows. The fourth pattern evident in our data occurs around Oct. 28, 2018, and shows subsidence at stations LT09, LT10, LT12, and LT19 and uplift at stations LA25, LA26, LA28, and LA30 (Fig. 2.13C). This spatial pattern looks more like an SSE than oceanographic waves. Although station LA39 located several hundred kilometers to the east also shows uplift during this period, the two near-trench stations between LA39 and the uplift stations, LA22 and LA23, do not show uplift. The uplift of LA39 is likely a coincidence.

To better understand the proposed SSE displacement pattern, we calculated the expected surface deformation from an SSE using Pylith, an open-source finite-element code (Aagaard et al., 2013). A model centered at 55.07N, 156.82W (depth range of 8-20 km) with a 20-degree oblique angle to the trench's perpendicular direction can reproduce the observed spatial pattern (Fig. 1 & Fig. 3D) with the uplift (3-4 cm) close to the trench and the subsidence (1-2 cm) further away from the trench. The location of stations LT09 and LT14 in the simulated model generates small deformations, but they are evident in detections. It can be due to the simple assumption of the shape of the SSE. The finite fault inversion method can help to better constrain the SSE area. The model predicts very small deformation at the inland GNSS stations and is consistent with GNSS observations.

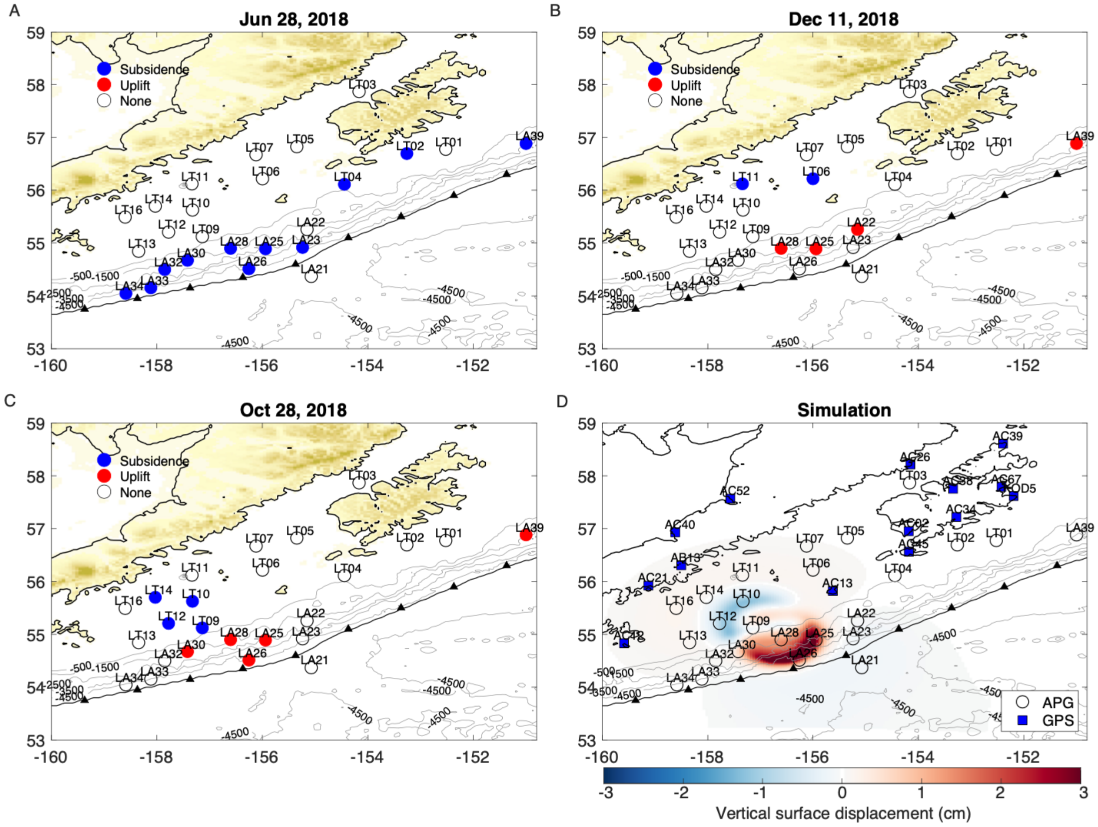

Fig. 2.13. *Detection snapshots and simulation. (A, B, C) The detection of apparent vertical deformation at three dates. More detected results are shown in the Movie 2.2. (D) Simulated surface displacement of an SSE on the thrust interface. Red and blue represent uplift and subsidence, respectively.*

Seismicity pattern

SSEs can trigger small earthquakes in nearby regions (Nishikawa & Ide, 2018; Vallée et al., 2013; Yarce et al., 2019). Here, we create an improved earthquake catalog in the area centered at the likely SSE region (see Method for details). Between June 10th and June 24th of 2019, some airgun shots occurred in our SSE region (Barcheck et al., 2020). Thus, we masked this period in Fig. 4A to avoid possible false earthquake detections. We also show the USGS catalog as a comparison. When there are AACSE and other sources of earthquakes in the USGS catalog, we chose the AACSE as the first choice for the earthquake locations and origin times. The total number of detected earthquakes in our catalog is about three times of that in the USGS catalog.

Daily seismicity rate shows an increase of seismicity in this area right after the SSE (Fig. 2.14A). We counted the number of earthquakes within a 120-km radius circle centered at 55°N, 157°W. The daily seismicity rate increases three times in the ten days right after the SSE compared to during the SSE in both the USGS catalog and our study. The elevated seismicity occurred on the up-dip and down-dip ends of the SSE area (Fig. 2.14B), likely triggered by the SSE. Additionally, the seismicity rate drops about 25 percent in the ten months after the SSE (Fig. 2.14A). There are two rate peaks before the SSE. The increased seismicity near July 24th, 2018, is due to a Mw 4.5 mainshock and its aftershocks. There is no major shock for the peak on August 13th, 2018. The magnitude of seismicity is smaller than 3 and earthquakes are sparsely distributed.

Earthquake swarms associated with shallow SSEs have been observed in New Zealand, Japan, and Ecuador (Bartlow et al., 2014; Montgomery-Brown & Syracuse, 2015; Nishikawa & Ide, 2018; Reverso et al., 2016; Vallée et al., 2013). In these studies, some swarms occurred before the SSE as foreshocks, and others occurred during or after the SSE. In our case, the earthquake swarms followed the SSE and are located updip and downdip of the SSE (Fig. 2.14B). We further calculate the Coulomb stress change caused by the SSE using the previously mentioned numerical simulation model. The elevated seismicity is located at positive Coulomb stress change regions, consistent with triggering by the SSE

(Fig. 2.14B). We also observed that the epicenters of the 2020 Simeonof earthquake and 2021 Chignik earthquake were located at the positive Coulomb stress change regions. The SSE increased the Coulomb stress for the 2021 earthquake by about 0.2 bar and the 2020 earthquake by less than 0.05 bar. The SSE might have advanced the 2021 Chignik earthquake.

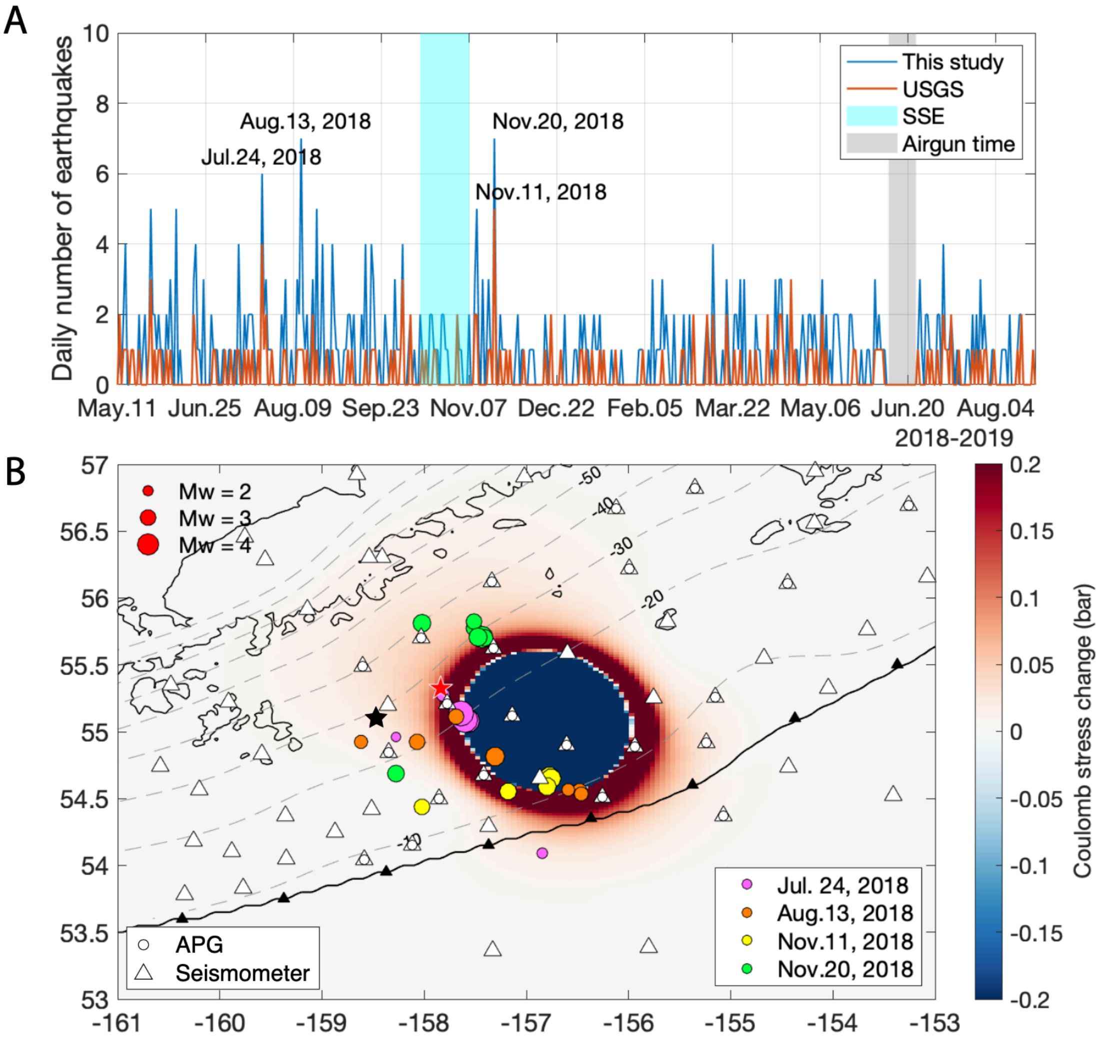

Figure 2.14. *Daily earthquakes and coulomb stress change. (A) Change of seismicity rate near the SSE region. The blue rectangle highlights the duration of the SSE. The gray bar*

masks the airgun shot time. (B) Coulomb stress change of the SSE. The different color dots represent the earthquake spatial distribution from four significant days, which are highlighted in (A). The yellow and green dots show the earthquake swarm after the SSE. The black and red stars label the epicenters of the 2020 Simeonof earthquake and 2021 Chignik earthquake, respectively.

Tremor detection

Often enhanced nonvolcanic tremor activity accompanies SSEs near their source area (Beroza & Ide, 2011; Rousset et al., 2019). In this study, we attempted to detect tremors using OBS data from Aug. 2018 to 2019 (see method section for details). Around 20 isolated short-duration (~ 90 seconds long) tremors were detected near the SSE at stations LA23, LA25 and LD36 (Fig. 2.15); however, only 3 occurred close in time to the SSE on Oct.7 (Fig. 2.15).

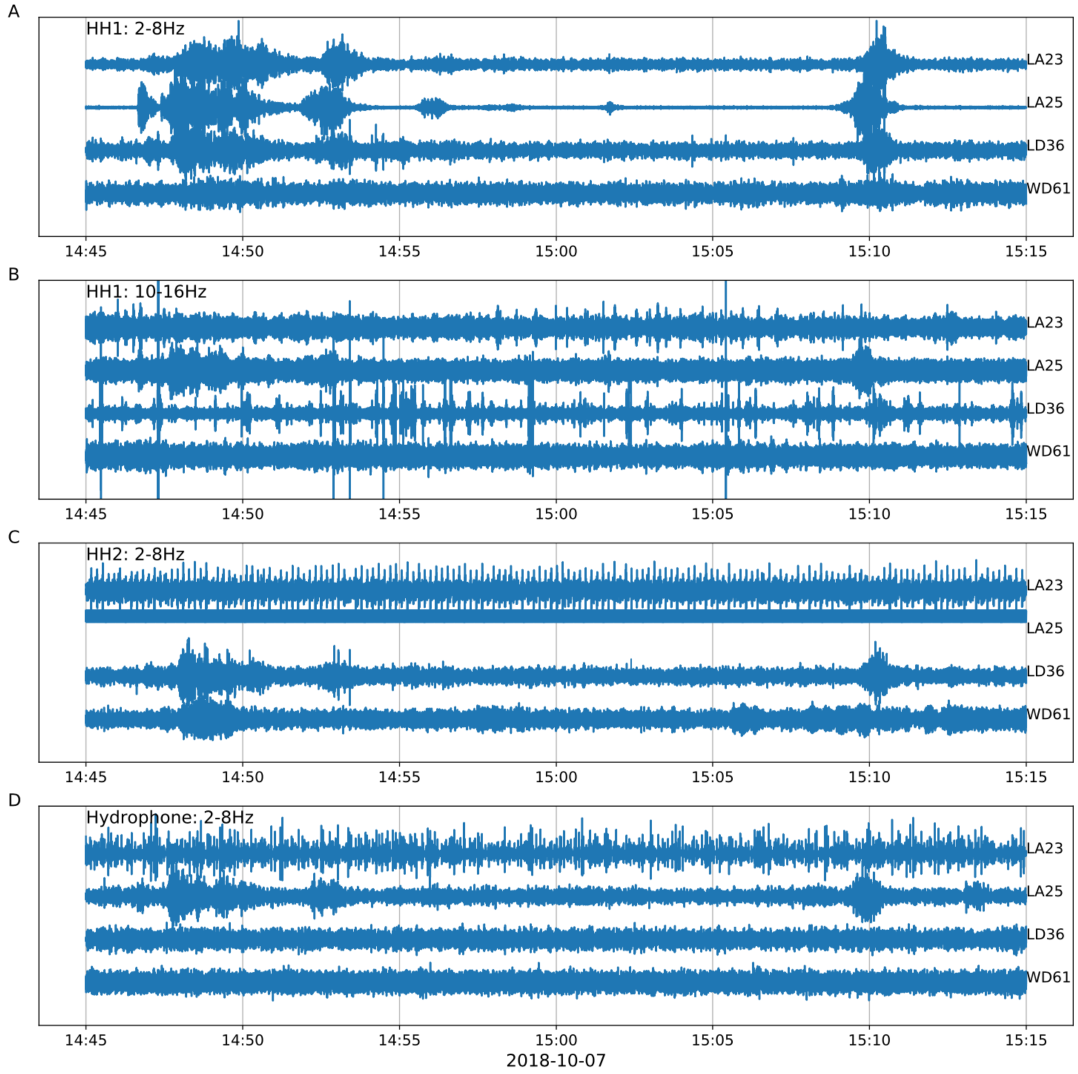

Figure 2.15. *An example of tremor detected by our method on Oct. 7, 2018. A and B show the HH1 component in 2-8 Hz and 10-16 Hz, respectively. C and D show the HH2 and EDH component in 2-8 Hz.*

The lack of enhanced tremor activity can be due to the sparse station distribution, noisy OBS data, small amplitude tremors, and fewer tremors in this area (Montgomery-Brown & Syracuse, 2015). The station spacing in AACSE is 20-40 km. We require at least three stations to detect a tremor. It is possible that only one or two stations captured some tremors, and we could not identify them. Additionally, noise is much higher (between 1 and 8 Hz) in the OBS data compared to the land stations (Barcheck et al., 2020). It is hard to detect small tremors from OBS data (A. G. Wech et al., 2013). Lastly, it is possible that tremors are just not abundant in this SSE area, which has been observed elsewhere. For example, Boso Peninsula did not produce any detectable tremors during the 2013 SSE, although the region is densely instrumented (Montgomery-Brown & Syracuse, 2015).

2.4 Discussion

Geological and physical conditions for SSE in this region

The occurrence of shallow SSEs is related to several conditions: (1) abundant fluids; (2) high fault roughness and heterogeneous fault structure; (3) near the transition zone of frictional properties; and (4) modestly unstable fault patches smaller than a critical dimension needed for earthquake nucleation (Bürgmann, 2018; Saffer & Wallace, 2015). In the Semidi segment, trace element analysis in nearby volcanoes shows that there is less fluid in Semidi compared to the Shumagin in the deep subduction zone (>100 km) (S. S. Wei et al., 2021). However, the fluid status is unclear in the shallow Semidi segment. On the one hand, there are several bending faults visible on seismic Line 4 on the west end of the Semidi segment, and the topography becomes smooth on seismic Line 3 in the middle part of the Semidi segment (J. Li et al., 2015; Shillington et al., 2015). Additionally, the Semidi segment has relatively thick sediments subducted compared to the southwest Shumagin segment (Shillington et al., 2015; S. S. Wei et al., 2021). A newly formed accretionary margin occurred only ~3 Ma ago and subducted sediments scraped by the accretionary wedge are relatively weak (Stevenson et al., 1983). The weakly faulted and thicker sediment layer could carry abundant pore fluid in intergranular and fracture porosity to enter the trench at Semidi. On the other hand, the seismic reflection data show that P wave velocity within the subducting layer of the Semidi segment is substantially lower than in the overlying plate, and is also lower than expected for its burial depth of hydrostatic pore-fluid pressure. The elevated Vp/Vs ratio, at the shallow subduction zone along the trench including the SSE area, is observed by a double-difference earthquake tomography study (F. Wang et al., 2021). It is likely that the shallow section is highly overpressured due to the sediment compaction (J. Li et al., 2018).

Thick Zodiac Fan sediment (~800-m) and other pelagic sediments subduct into the Semidi segment (Stevenson et al., 1983). However, such thick sediment cannot submerge the subducting ridge, whose height is over 1 km. In the west of the Semidi segment, a buried extension of the subducting Patton-Murray Ridge was recognized. It created a ridge or escarpment terminating the continental shelf and an embayment in the accretionary front (Fig. 2.1) (Huene et al., 2016). These geological features are unique in Semidi and thought to be favorable for tsunami hosting earthquakes (Huene et al., 2016). The physical conditions for tsunami hosting earthquakes and shallow SSEs are similar (Saffer & Wallace, 2015), which may also favor shallow SSEs. The 2021 Mw 8.2 Chignik earthquake occurred at this spot but created a minor tsunami and did not rupture to shallow depth, suggesting that shallow SSEs are possible in this area. The buried extension of the subducting Patton-Murray Ridge can be responsible for the SSEs.

There are many seismic reflection studies from Kodiak to Shumagin. The detailed fault structure information can help indicate the different portions of the seismogenic zone. On the west Semidi, a thin sharp reflection with a single low-velocity zone is observed at a depth of 13 to 20 km, and it is explained as the frictional unstable region (J. Li et al., 2015). In our SSE simulation result, significant slip is also found at the shallow depths around 8-15 km, so our proposed SSE dominantly slides at the velocity-strengthening (stable) to weakening (unstable) fault patch. The fault patch can be over-pressured and slip as SSEs due to a combination of trapping fluids and disequilibrium compaction.

The relation between the SSE and large earthquakes.

Our detected SSE occurred between Oct. 12 and Nov. 6 of 2018 with 5 – 10 days of uncertainty. On July 22, 2020, a Mw 7.8 earthquake occurred on the Shumagin segment, located about 150 km southwest of the SSE area. The 2021 Chignik main shock occurred on the Semidi segment in July, and the hypocenter is at 32.2 km depth. Seismic inversion shows that the earthquake did not rupture to the shallow subduction zone (Liu et al., 2022). In contrast, a Mw 8.3 earthquake occurred in 1938 just east of the 2021 Chignik earthquake. The 1938 earthquake ruptured to a much shallower depth and generated an intermediate tsunami (Freymueller et al., 2021). The relatively deeper earthquake in 2021 compared to the 1938 earthquake could be due to the occurrence of the SSE, which released the stress accumulations in the shallow Semidi subduction zone. Besides, the epicenter of these earthquakes is located at the positive Coulomb stress change regions. The SSE can statically trigger these two large earthquakes according to their nucleation zones

A 10-year analysis of the b-value in this area shows that the SSE occurred in a region with a low b-value (Liu et al., 2020). Variations of the b-value can be interpreted as the presence of asperities and variable frictional properties (Schorlemmer & Wiemer, 2005). The decrease in b-value also indicates the high-stress accumulation and potential large earthquake location (Nanjo et al., 2012; Schorlemmer et al., 2005). In the west Semidi segment, Liu et al. (2020) found the b-value gradually decreased from 0.95 to below 0.8 since 2011, which can be related to the nucleation of the 2021 Chignik earthquake. They also observed that the b-value rebounded from 0.7 to 0.75 at the end of 2018. The rebound might have been caused by the stress released by the 2018 SSE.

We applied a newly developed machine learning method to detect SSEs in seafloor pressure data between summers of 2018 and 2019 offshore southern Alaska. The method detected one event between Oct. 13 and Nov. 6, 2018 with 5 to 10 days of uncertainty. The spatial pattern of the deformation is unlikely oceanographic in origin, based on analysis of the 10-years model output from the global numerical circulation model HYCOM. It is consistent with a simulated ground deformation from an oval-shaped SSE patch on the subduction interface. The spatial and temporal evolution of seismicity in this region is also consistent with the existence of an SSE. Our detected SSE is located 150-km northeast of the 2020 Mw 7.8 Alaska earthquake and updip of the 2021 Mw 8.2 Chignik earthquake. Neither earthquake ruptured to the shallow depth, and no significant tsunami occurred with the two earthquakes, consistent with our observations of shallow SSEs in this region, which released tectonic stresses on the shallow subduction zone interface. Our method has the potential to transform the way of detecting such signals in seafloor pressure data offshore, especially where the signal source is far away from the shoreline.

Acknowledgments

We sincerely thank Randolph Watts and Karen Tracey for the guidance on analyzing seafloor pressure data, Natalia Ruppert for providing velocity models of Alaskan-Aleutian subduction zone, Jiuxun Yin and Noel Bartlow for their constructive and productive discussion, and Sandra Slead for proof reading. We are grateful to the PIs and staffs of the AACSE for providing the Alaska ocean bottom pressure and seismic data. This project is supported by the National Science Foundation of United States (Award #2025563 and #1949620).

Data and materials availability

AACSE seismic and pressure data can be downloaded from ISRS. The earthquake catalog is from USGS website. The HYCOM data are from HYCOM website (https://www.hycom.org/dataserver/gofs-3pt1/reanalysis). The ECCO4 data are from NASA ECCO website (https://podaac.jpl.nasa.gov/ECCO?tab=mission-objectives&sections=about%2Bdata). High-resolution bathymetry data are from GMRT website (https://www.gmrt.org/GMRTMapTool/). Most of the data processing, calculations, and figures are carried out using MATLAB and PYTHON. The machine learning code was written with Python packages Keras (https:// keras.io/) and Scikit-learn (https://sci- kit-learn.org/stable/). The machine learning model can be found in github (https://github.com/bing-he/SSE_detection_using_machine_learning).

References

Aagaard, B. T., Knepley, M. G., & Williams, C. A. (2013). A domain decomposition approach to implementing fault slip in finite-element models of quasi-static and dynamic crustal deformation. *Journal of Geophysical Research: Solid Earth*, *118*(6), 3059–3079. https://doi.org/10.1002/jgrb.50217

Araki, E., Saffer, D. M., Kopf, A. J., Wallace, L. M., Kimura, T., Machida, Y., et al. (2017). Recurring and triggered slow-slip events near the trench at the Nankai Trough subduction megathrust. *Science*, *356*(6343), 1157–1160. https://doi.org/10.1126/science.aan3120

Baba, T., Hirata, K., Hori, T., & Sakaguchi, H. (2006). Offshore geodetic data conducive to the estimation of the afterslip distribution following the 2003 Tokachi-oki earthquake. *Earth and Planetary Science Letters*, *241*(1), 281–292. https://doi.org/10.1016/j.epsl.2005.10.019

Badrinarayanan, V., Handa, A., & Cipolla, R. (2015, May 27). SegNet: A Deep Convolutional Encoder-Decoder Architecture for Robust Semantic Pixel-Wise Labelling. arXiv. https://doi.org/10.48550/arXiv.1505.07293

Baillard, C., Crawford, W. C., Ballu, V., Hibert, C., & Mangeney, A. (2013). An Automatic Kurtosis-Based P- and S-Phase Picker Designed for Local Seismic Networks. *Bulletin of the Seismological Society of America*, *104*(1), 394–409. https://doi.org/10.1785/0120120347

Baker-Yeboah, S., Watts, D. R., Byrne, D. A., & Witter, D. L. (2011). Sea Surface Height Variability in the eastern South Atlantic from Satellite and in situ Measurements, *2011*, OS23A-1620.

Bappy, J. H., Simons, C., Nataraj, L., Manjunath, B. S., & Roy-Chowdhury, A. K. (2019). Hybrid LSTM and Encoder–Decoder Architecture for Detection of Image Forgeries. *IEEE Transactions on Image Processing*, *28*(7), 3286–3300. https://doi.org/10.1109/TIP.2019.2895466

Barcheck, G., Abers, G. A., Adams, A. N., Bécel, A., Collins, J., Gaherty, J. B., et al. (2020). The Alaska Amphibious Community Seismic Experiment. *Seismological Research Letters*, *91*(6), 3054–3063. https://doi.org/10.1785/0220200189

Bartlow, N. M., Wallace, L. M., Beavan, R. J., Bannister, S., & Segall, P. (2014). Time-dependent modeling of slow slip events and associated seismicity and tremor at the Hikurangi subduction zone, New Zealand. *Journal of Geophysical Research: Solid Earth*, *119*(1), 734–753. https://doi.org/10.1002/2013JB010609

Bergen, K. J., Johnson, P. A., Hoop, M. V. de, & Beroza, G. C. (2019). Machine learning for data-driven discovery in solid Earth geoscience. *Science*, *363*(6433). https://doi.org/10.1126/science.aau0323

Beroza, G. C., & Ide, S. (2011). Slow Earthquakes and Nonvolcanic Tremor. *Annual Review of Earth and Planetary Sciences*, *39*(1), 271–296. https://doi.org/10.1146/annurev-earth-040809-152531

Bürgmann, R. (2018). The geophysics, geology and mechanics of slow fault slip. *Earth and Planetary Science Letters*, *495*, 112–134. https://doi.org/10.1016/j.epsl.2018.04.062

Chen, K. H., Tai, H.-J., Ide, S., Byrne, T. B., & Johnson, C. W. (2018). Tidal Modulation and Tectonic Implications of Tremors in Taiwan. *Journal of Geophysical Research: Solid Earth*, *123*(7), 5945–5964. https://doi.org/10.1029/2018JB015663

Crowell, B. W., & Melgar, D. (2020). Slipping the Shumagin Gap: A Kinematic Coseismic and Early Afterslip Model of the Mw 7.8 Simeonof Island, Alaska, Earthquake. *Geophysical Research Letters*, *47*(19), e2020GL090308. https://doi.org/10.1029/2020GL090308

Cummings, J. A., & Smedstad, O. M. (2013). Variational Data Assimilation for the Global Ocean. In S. K. Park & L. Xu (Eds.), *Data Assimilation for Atmospheric, Oceanic and Hydrologic Applications (Vol. II)* (pp. 303–343). Berlin, Heidelberg: Springer. https://doi.org/10.1007/978-3-642-35088-7_13

Davies, J., Sykes, L., House, L., & Jacob, K. (1981). Shumagin Seismic Gap, Alaska Peninsula: History of great earthquakes, tectonic setting, and evidence for high seismic potential. *Journal of Geophysical Research: Solid Earth*, *86*(B5), 3821–3855. https://doi.org/10.1029/JB086iB05p03821

Davis, E. E., Villinger, H., & Sun, T. (2015). Slow and delayed deformation and uplift of the outermost subduction prism following ETS and seismogenic slip events beneath Nicoya Peninsula, Costa Rica. *Earth and Planetary Science Letters*, *410*, 117–127. https://doi.org/10.1016/j.epsl.2014.11.015

Dixon, T. H., Jiang, Y., Malservisi, R., McCaffrey, R., Voss, N., Protti, M., & Gonzalez, V. (2014). Earthquake and tsunami forecasts: Relation of slow slip events to subsequent earthquake rupture. *Proceedings of the National Academy of Sciences*, *111*(48), 17039–17044.

Dobashi, Y., & Inazu, D. (2021). Improving Detectability of Seafloor Deformation From Bottom Pressure Observations Using Numerical Ocean Models. *Frontiers in Earth Science*, *8*. https://doi.org/10.3389/feart.2020.598270

Fredrickson, E. K., Wilcock, W. S. D., Schmidt, D. A., MacCready, P., Roland, E., Kurapov, A. L., et al. (2019). Optimizing Sensor Configurations for the Detection of Slow-Slip Earthquakes in Seafloor Pressure Records, Using the Cascadia Subduction Zone as a Case Study. *Journal of Geophysical Research: Solid Earth*, *124*(12), 13504–13531. https://doi.org/10.1029/2019JB018053

Freymueller, J. T., Suleimani, E. N., & Nicolsky, D. J. (2021). Constraints on the Slip Distribution of the 1938 MW 8.3 Alaska Peninsula Earthquake From Tsunami Modeling. *Geophysical Research Letters*, *48*(9), e2021GL092812. https://doi.org/10.1029/2021GL092812

Gomberg, J., Hautala, S., Johnson, P., & Chiswell, S. (2019). Separating Sea and Slow Slip Signals on the Seafloor. *Journal of Geophysical Research: Solid Earth*, *124*(12), 13486–13503. https://doi.org/10.1029/2019JB018285

Hayes, G. P., Moore, G. L., Portner, D. E., Hearne, M., Flamme, H., Furtney, M., & Smoczyk, G. M. (2018). Slab2, a comprehensive subduction zone geometry model. *Science*, *362*(6410), 58–61. https://doi.org/10.1126/science.aat4723

He, B., Watts, R. D., Tracey, K. L., Donohue, K. A., & Wei, M. (2018). Reducing `Noise' in Ocean Bottom Pressure Measurements in the Cascadia Subduction Zone. *AGU Fall Meeting Abstracts*, *T41F-0369*. Retrieved from http://adsabs.harvard.edu/abs/2018AGUFM.T41F0369H

He, B., Wei, M., Watts, D. R., & Shen, Y. (2020). Detecting Slow Slip Events From Seafloor Pressure Data Using Machine Learning. *Geophysical Research Letters*, *47*(11), e2020GL087579. https://doi.org/10.1029/2020GL087579

Hino, R., Inazu, D., Ohta, Y., Ito, Y., Suzuki, S., Iinuma, T., et al. (2014). Was the 2011 Tohoku-Oki earthquake preceded by aseismic preslip? Examination of seafloor vertical deformation data near the epicenter. *Marine Geophysical Research*, *35*(3), 181–190. https://doi.org/10.1007/s11001-013-9208-2

Huene, R. von, Miller, J. J., & Dartnell, P. (2016). A possible transoceanic tsunami directed toward the U.S. west coast from the Semidi segment, Alaska convergent margin. *Geochemistry, Geophysics, Geosystems*, *17*(3), 645–659. https://doi.org/10.1002/2015GC006147

Ide, S. (2012). Variety and spatial heterogeneity of tectonic tremor worldwide. *Journal of Geophysical Research: Solid Earth*, *117*(B3). https://doi.org/10.1029/2011JB008840

Inazu, D., Hino, R., & Fujimoto, H. (2012). A global barotropic ocean model driven by synoptic atmospheric disturbances for detecting seafloor vertical displacements from in situ ocean bottom pressure measurements. *Marine Geophysical Research*, *33*(2), 127–148. https://doi.org/10.1007/s11001-012-9151-7

Inoue, T., Ito, Y., Wallace, L. M., Yoshikawa, Y., Inazu, D., Garcia, E. S. M., et al. (2021). Water Depth Dependence of Long-Range Correlation in Nontidal Variations in Seafloor Pressure. *Geophysical Research Letters*, *48*(8), e2020GL092173. https://doi.org/10.1029/2020GL092173

Ito, Y., Hino, R., Kido, M., Fujimoto, H., Osada, Y., Inazu, D., et al. (2013a). Episodic slow slip events in the Japan subduction zone before the 2011 Tohoku-Oki earthquake. *Tectonophysics*, *600*, 14–26. https://doi.org/10.1016/j.tecto.2012.08.022

Ito, Y., Hino, R., Kido, M., Fujimoto, H., Osada, Y., Inazu, D., et al. (2013b). Episodic slow slip events in the Japan subduction zone before the 2011 Tohoku-Oki earthquake. *Tectonophysics*, *600*, 14–26. https://doi.org/10.1016/j.tecto.2012.08.022

Itoh, Y., Nishimura, T., Ariyoshi, K., & Matsumoto, H. (2019). Interplate Slip Following the 2003 Tokachi-oki Earthquake From Ocean Bottom Pressure Gauge and Land GNSS Data. *Journal of Geophysical Research: Solid Earth*, *124*(4), 4205–4230. https://doi.org/10.1029/2018JB016328

Kingma, D. P., & Ba, J. (2014). Adam: A Method for Stochastic Optimization. *ArXiv:1412.6980 [Cs]*. Retrieved from http://arxiv.org/abs/1412.6980

Kong, Q., Trugman, D. T., Ross, Z. E., Bianco, M. J., Meade, B. J., & Gerstoft, P. (2019). Machine Learning in Seismology: Turning Data into Insights. *Seismological Research Letters*, *90*(1), 3–14. https://doi.org/10.1785/0220180259

Li, J., Shillington, D. J., Bécel, A., Nedimović, M. R., Webb, S. C., Saffer, D. M., et al. (2015). Downdip variations in seismic reflection character: Implications for fault structure and seismogenic behavior in the Alaska subduction zone. *Journal of Geophysical Research: Solid Earth*, *120*(11), 7883–7904. https://doi.org/10.1002/2015JB012338

Li, J., Shillington, D. J., Saffer, D. M., Bécel, A., Nedimović, M. R., Kuehn, H., et al. (2018). Connections between subducted sediment, pore-fluid pressure, and earthquake behavior along the Alaska megathrust. *Geology*, *46*(4), 299–302. https://doi.org/10.1130/G39557.1

Li, S., & Freymueller, J. T. (2018). Spatial Variation of Slip Behavior Beneath the Alaska Peninsula Along Alaska-Aleutian Subduction Zone. *Geophysical Research Letters*, *45*(8), 3453–3460. https://doi.org/10.1002/2017GL076761

Li, S., Freymueller, J., & McCaffrey, R. (2016). Slow slip events and time-dependent variations in locking beneath Lower Cook Inlet of the Alaska-Aleutian subduction zone. *Journal of Geophysical Research: Solid Earth*, *121*(2), 1060–1079. https://doi.org/10.1002/2015JB012491

Lindsey, E. O., Mallick, R., Hubbard, J. A., Bradley, K. E., Almeida, R. V., Moore, J. D. P., et al. (2021). Slip rate deficit and earthquake potential on shallow megathrusts. *Nature Geoscience*, *14*(5), 321–326. https://doi.org/10.1038/s41561-021-00736-x

Liu, C., Lay, T., Xiong, X., & Wen, Y. (2020). Rupture of the 2020 MW 7.8 Earthquake in the Shumagin Gap Inferred From Seismic and Geodetic Observations.

Geophysical Research Letters, *47*(22), e2020GL090806. https://doi.org/10.1029/2020GL090806

Liu, C., Lay, T., & Xiong, X. (2022). The 29 July 2021 MW 8.2 Chignik, Alaska Peninsula Earthquake Rupture Inferred From Seismic and Geodetic Observations: Re-Rupture of the Western 2/3 of the 1938 Rupture Zone. *Geophysical Research Letters*, *49*(4), e2021GL096004. https://doi.org/10.1029/2021GL096004

Lomax, A., Virieux, J., Volant, P., & Berge-Thierry, C. (2000). Probabilistic Earthquake Location in 3D and Layered Models. In C. H. Thurber & N. Rabinowitz (Eds.), *Advances in Seismic Event Location* (pp. 101–134). Dordrecht: Springer Netherlands. https://doi.org/10.1007/978-94-015-9536-0_5

Montgomery-Brown, E. K., & Syracuse, E. M. (2015). Tremor-genic slow slip regions may be deeper and warmer and may slip slower than non-tremor-genic regions. *Geochemistry, Geophysics, Geosystems*, *16*(10), 3593–3606. https://doi.org/10.1002/2015GC005895

Moseley, B., Markham, A., & Nissen-Meyer, T. (2018). Fast approximate simulation of seismic waves with deep learning. *ArXiv:1807.06873 [Physics]*. Retrieved from http://arxiv.org/abs/1807.06873

Mousavi, S. M., Zhu, W., Sheng, Y., & Beroza, G. C. (2019). CRED: A Deep Residual Network of Convolutional and Recurrent Units for Earthquake Signal Detection. *Scientific Reports*, *9*(1), 1–14. https://doi.org/10.1038/s41598-019-45748-1

Mousavi, S. M., Ellsworth, W. L., Zhu, W., Chuang, L. Y., & Beroza, G. C. (2020). Earthquake transformer—an attentive deep-learning model for simultaneous earthquake detection and phase picking. *Nature Communications*, *11*(1), 3952. https://doi.org/10.1038/s41467-020-17591-w

Munk, W. H., Cartwright, D. D., & Bullard, E. C. (1966). Tidal spectroscopy and prediction. *Philosophical Transactions of the Royal Society of London. Series A, Mathematical and Physical Sciences*, *259*(1105), 533–581. https://doi.org/10.1098/rsta.1966.0024

Muramoto, T., Ito, Y., Inazu, D., Wallace, L. M., Hino, R., Suzuki, S., et al. (2019). Seafloor Crustal Deformation on Ocean Bottom Pressure Records With Nontidal Variability Corrections: Application to Hikurangi Margin, New Zealand. *Geophysical Research Letters*, *46*(1), 303–310. https://doi.org/10.1029/2018GL080830

Nanjo, K. Z., Hirata, N., Obara, K., & Kasahara, K. (2012). Decade-scale decrease inb value prior to the M9-class 2011 Tohoku and 2004 Sumatra quakes. *Geophysical Research Letters*, *39*(20). https://doi.org/10.1029/2012GL052997

Nishikawa, T., & Ide, S. (2018). Recurring Slow Slip Events and Earthquake Nucleation in the Source Region of the M 7 Ibaraki-Oki Earthquakes Revealed by Earthquake Swarm and Foreshock Activity. *Journal of Geophysical Research: Solid Earth*, *123*(9), 7950–7968. https://doi.org/10.1029/2018JB015642

Park, H., Oh, C., Moon, J., & Kim, S. (2018). Development of a lane change risk index using vehicle trajectory data. *Accident Analysis & Prevention*, *110*, 1–8. https://doi.org/10.1016/j.aap.2017.10.015

Perol, T., Gharbi, M., & Denolle, M. (2018). Convolutional neural network for earthquake detection and location. *Science Advances*, *4*(2), e1700578. https://doi.org/10.1126/sciadv.1700578

Polster, A., Fabian, M., & Villinger, H. (2009). Effective resolution and drift of Paroscientific pressure sensors derived from long-term seafloor measurements. *Geochemistry, Geophysics, Geosystems*, *10*(8). https://doi.org/10.1029/2009GC002532

Reverso, T., Marsan, D., Helmstetter, A., & Enescu, B. (2016). Background seismicity in Boso Peninsula, Japan: Long-term acceleration, and relationship with slow slip events. *Geophysical Research Letters*, *43*(11), 5671–5679. https://doi.org/10.1002/2016GL068524

Ross, Z. E., White, M. C., Vernon, F. L., & Ben-Zion, Y. (2016). An Improved Algorithm for Real-Time S-Wave Picking with Application to the (Augmented) ANZA Network in Southern California. *Bulletin of the Seismological Society of America*, *106*(5), 2013–2022. https://doi.org/10.1785/0120150230

Rousset, B., Fu, Y., Bartlow, N., & Bürgmann, R. (2019). Weeks-Long and Years-Long Slow Slip and Tectonic Tremor Episodes on the South Central Alaska Megathrust. *Journal of Geophysical Research: Solid Earth*, *124*(12), 13392–13403. https://doi.org/10.1029/2019JB018724

Ruiz, S., Metois, M., Fuenzalida, A., Ruiz, J., Leyton, F., Grandin, R., et al. (2014). Intense foreshocks and a slow slip event preceded the 2014 Iquique Mw 8.1 earthquake. *Science*, *345*(6201), 1165–1169. https://doi.org/10.1126/science.1256074

Saffer, D. M., & Wallace, L. M. (2015). The frictional, hydrologic, metamorphic and thermal habitat of shallow slow earthquakes. *Nature Geoscience*, *8*(8), 594–600. https://doi.org/10.1038/ngeo2490

Schorlemmer, D., & Wiemer, S. (2005). Microseismicity data forecast rupture area. *Nature*, *434*(7037), 1086–1086. https://doi.org/10.1038/4341086a

Schorlemmer, D., Wiemer, S., & Wyss, M. (2005). Variations in earthquake-size distribution across different stress regimes. *Nature*, *437*(7058), 539–542. https://doi.org/10.1038/nature04094

Serban, I., Klinger, T., Tesauro, G., Talamadupula, K., Zhou, B., Bengio, Y., & Courville, A. (2017). Multiresolution Recurrent Neural Networks: An Application to Dialogue Response Generation. *Proceedings of the AAAI Conference on Artificial Intelligence*, *31*(1). https://doi.org/10.1609/aaai.v31i1.10984

Shillington, D. J., Bécel, A., Nedimović, M. R., Kuehn, H., Webb, S. C., Abers, G. A., et al. (2015). Link between plate fabric, hydration and subduction zone seismicity in Alaska. *Nature Geoscience*, *8*(12), 961–964. https://doi.org/10.1038/ngeo2586

Shoji, D., Noguchi, R., Otsuki, S., & Hino, H. (2018). Classification of volcanic ash particles using a convolutional neural network and probability. *Scientific Reports*, *8*(1), 1–12. https://doi.org/10.1038/s41598-018-26200-2

Stevenson, A. J., Scholl, D. W., & Vallier, T. L. (1983). Tectonic and geologic implications of the Zodiac fan, Aleutian Abyssal Plain, northeast Pacific. *GSA Bulletin*, *94*(2), 259–273. https://doi.org/10.1130/0016-7606(1983)94<259:TAGIOT>2.0.CO;2

Suzuki, K., Nakano, M., Takahashi, N., Hori, T., Kamiya, S., Araki, E., et al. (2016). Synchronous changes in the seismicity rate and ocean-bottom hydrostatic pressures along the Nankai trough: A possible slow slip event detected by the Dense Oceanfloor Network system for Earthquakes and Tsunamis (DONET). *Tectonophysics*, *680*, 90–98. https://doi.org/10.1016/j.tecto.2016.05.012

Todd, E. K., & Schwartz, S. Y. (2016). Tectonic tremor along the northern Hikurangi Margin, New Zealand, between 2010 and 2015. *Journal of Geophysical Research: Solid Earth*, *121*(12), 8706–8719. https://doi.org/10.1002/2016JB013480

Todd, E. K., Schwartz, S. Y., Mochizuki, K., Wallace, L. M., Sheehan, A. F., Webb, S. C., et al. (2018). Earthquakes and Tremor Linked to Seamount Subduction During Shallow Slow Slip at the Hikurangi Margin, New Zealand. *Journal of Geophysical Research: Solid Earth*, *123*(8), 6769–6783. https://doi.org/10.1029/2018JB016136

Vallée, M., Nocquet, J.-M., Battaglia, J., Font, Y., Segovia, M., Régnier, M., et al. (2013). Intense interface seismicity triggered by a shallow slow slip event in the Central Ecuador subduction zone. *Journal of Geophysical Research: Solid Earth*, *118*(6), 2965–2981. https://doi.org/10.1002/jgrb.50216

Wallace, L. M., Webb, S. C., Ito, Y., Mochizuki, K., Hino, R., Henrys, S., et al. (2016). Slow slip near the trench at the Hikurangi subduction zone, New Zealand. *Science*, *352*(6286), 701–704.

Wang, F., Wei, S. S., Ruppert, N. A., & Zhang, H. (2021). Seismic imaging of the Alaska Peninsula using the body-wave double-difference tomography. AGU. Retrieved from https://agu.confex.com/agu/fm21/meetingapp.cgi/Paper/903665

Wang, Q., Guo, Y., Yu, L., & Li, P. (2017). Earthquake Prediction based on Spatio-Temporal Data Mining: An LSTM Network Approach. *IEEE Transactions on Emerging Topics in Computing*, 1–1. https://doi.org/10.1109/TETC.2017.2699169

Warren-Smith, E., Fry, B., Wallace, L., Chon, E., Henrys, S., Sheehan, A., et al. (2019). Episodic stress and fluid pressure cycling in subducting oceanic crust during slow slip. *Nature Geoscience*, *12*(6), 475–481. https://doi.org/10.1038/s41561-019-0367-x

Watts, D. R., & Kontoyiannis, H. (1990). Deep-Ocean Bottom Pressure Measurement: Drift Removal and Performance. *Journal of Atmospheric and Oceanic Technology*, *7*(2), 296–306. https://doi.org/10.1175/1520-0426(1990)007<0296:DOBPMD>2.0.CO;2

Wech, A. G., Sheehan, A. F., Boese, C. M., Townend, J., Stern, T. A., & Collins, J. A. (2013). Tectonic Tremor Recorded by Ocean Bottom Seismometers. *Seismological Research Letters*, *84*(5), 752–758. https://doi.org/10.1785/0220120184

Wech, Aaron G., & Creager, K. C. (2008). Automated detection and location of Cascadia tremor. *Geophysical Research Letters*, *35*(20). https://doi.org/10.1029/2008GL035458

Wei, M., McGuire, J. J., & Richardson, E. (2012). A slow slip event in the south central Alaska Subduction Zone and related seismicity anomaly. *Geophysical Research Letters*, *39*(15). https://doi.org/10.1029/2012GL052351

Wei, S. S., Ruprecht, P., Gable, S. L., Huggins, E. G., Ruppert, N., Gao, L., & Zhang, H. (2021). Along-strike variations in intermediate-depth seismicity and arc magmatism along the Alaska Peninsula. *Earth and Planetary Science Letters*, *563*, 116878. https://doi.org/10.1016/j.epsl.2021.116878

Wei, X., Shen, Y., Caplan-Auerbach, J., & Morgan, J. (2020). An improved earthquake catalog during the 2018 Kīlauea Volcano eruption from combined onshore and offshore seismic arrays. AGU. Retrieved from https://agu.confex.com/agu/fm20/meetingapp.cgi/Paper/689044

Wiszniowski, J., Plesiewicz, B. M., & Trojanowski, J. (2014). Application of real time recurrent neural network for detection of small natural earthquakes in Poland. *Acta Geophysica*, *62*(3), 469–485. https://doi.org/10.2478/s11600-013-0140-2

Withers, M., Aster, R., Young, C., Beiriger, J., Harris, M., Moore, S., & Trujillo, J. (1998). A comparison of select trigger algorithms for automated global seismic phase and event detection. *Bulletin of the Seismological Society of America*, *88*(1), 95–106. https://doi.org/10.1785/BSSA0880010095

Xiao, Z., Freymueller, J. T., Grapenthin, R., Elliott, J. L., Drooff, C., & Fusso, L. (2021). The deep Shumagin gap filled: Kinematic rupture model and slip budget analysis of the 2020 Mw 7.8 Simeonof earthquake constrained by GNSS, global seismic waveforms, and floating InSAR. *Earth and Planetary Science Letters*, *576*, 117241. https://doi.org/10.1016/j.epsl.2021.117241

Yarce, J., Sheehan, A. F., Nakai, J. S., Schwartz, S. Y., Mochizuki, K., Savage, M. K., et al. (2019). Seismicity at the Northern Hikurangi Margin, New Zealand, and Investigation of the Potential Spatial and Temporal Relationships With a Shallow Slow Slip Event. *Journal of Geophysical Research: Solid Earth*, *124*(5), 4751–4766. https://doi.org/10.1029/2018JB017211

Ye, L., Lay, T., Kanamori, H., Yamazaki, Y., & Cheung, K. F. (2021). The 22 July 2020 MW 7.8 Shumagin seismic gap earthquake: Partial rupture of a weakly coupled megathrust. *Earth and Planetary Science Letters*, *562*, 116879. https://doi.org/10.1016/j.epsl.2021.116879

Zhu, W., & Beroza, G. C. (2019). PhaseNet: a deep-neural-network-based seismic arrival-time picking method. *Geophysical Journal International*, *216*(1), 261–273. https://doi.org/10.1093/gji/ggy423

CHAPTER 3

Quantifying the water contribution to seafloor pressure by combining machine learning method and ocean circulation models

Bing He

Abstract

Megathrust earthquakes with destructive tsunamic waves mainly occurred in the offshore subduction zone, causing massive fatalities and significant property losses. Due to their underwater environment, monitoring these offshore faults and estimating the location and size of potential earthquakes and tsunamis are challenging. Seafloor pressure data have been used to monitor vertical tectonic motion on the seafloor, especially in detecting slow slip events. However, such detections are difficult due to long-term instrumental drift and considerable water noise. In this study, I investigate the ocean circulation-generated pressure by using the machine learning method. The investigated process can help quantify the ocean circulation-generated signals and better detect the tectonic deformation signals.

3.1 Introduction

Seafloor pressure measurements have been recorded for over a decade, but only detected SSEs in a few cases. Correctly detecting SSEs from the seafloor pressure data mainly depends on finding SSE signals from the terrestrial observations (Hino et al., 2014; Wallace et al., 2016). The essential issues limiting SSEs detection are long-term instrumental drifts and large water movement noises in the pressure data. It is hard to remove those effects thoroughly. In our previous studies, we designed a machine learning algorithm to detect SSEs with instrumental drifts and ocean circulation-generated signals. The variations of surrounding water movements prevented us to detect small SSEs. In this study, I am exploring how to reduce the water movement noise and improve the signal-to-noise ratio.

The observed seafloor pressure can be expressed as a formula (3-1).

$$P(x,t) = P_T(x,t) + P_D(x,t) + P_{SSE}(x,t) + P_O(x,t) + \varepsilon(x,t) \qquad (3\text{-}1)$$

The measured seafloor pressure, $P(x,t)$, varied with location x and time t, can be considered a sum of the following signals: $P_T(x,t)$ earth tides, $P_D(x,t)$ instrumental drift, $P_{SSE}(x,t)$ SSE (tectonic motion) caused pressure changes, $P_O(x,t)$ non-tidal ocean circulation, and $\varepsilon(x,t)$ other unknown sources of noise. Tide waves can be removed by using tidal response models or a half-day low pass filter. Long-term drift is often removed by an exponential plus linear curve (Watts & Kontoyiannis, 1990). However, if an SSE exists in the pressure data, the de-drifting procedure will tilt the SSE and make the detection harder. Ocean water columns that contributed to seafloor pressure changes $P_O(x,t)$ have large amplitude and mixed frequency components than the tectonic motion that contributed to seafloor pressure changes $P_{SSE}(x,t)$. Directly distinguishing them in both the time and frequency domain is very difficult. Therefore, other auxiliary measurements or simulations are necessary.

There are four standard methods to remove the oceanographic signals in pressure data, including the reference station method (Wallace et al., 2016), ocean circulation model (Inazu et al., 2012), depth-matched spatial coherence method (Fredrickson et al., 2019), and temperature pressure correlation method (Gomberg et al., 2019). The reference station method uses one station at the other side of the trench as the reference and subtracts it from other stations because the subducting plate does not move during an SSE. This method applies when the station's spatial distance is less than 200 km and the depth offset is within 3 km. For example, the reference station method works well for the northern Hikurangi Margin, a small, shallow continental slope region (Wallace et al., 2016).The reference station method can remove 80%-95% of oceanographic signals $P_O(x,t)$ (Wallace et al., 2016). Nevertheless, the ocean circulation model works better for stations located far away and with relatively significant depth differences than the reference station method. For instance, Muramoto et al. (2019) indicated that station LOBS8 and TXBPR2 have larger variance reduction using the ocean model method than the reference station method in New Zealand 2014-2015 SSE.

The ocean circulation model method includes the global ocean circulation model: HYCOM, ECCO2, GLORYS, and regional ocean model: ROMs, which subtracts the modeled seafloor pressure data from real data. Most models are reanalysis which assimilates with the satellite altimeter observations and in-situ sea surface temperature as well as in-situ vertical temperature and salinity profiles (Cummings & Smedstad, 2013). According to different assimilating methods and statements, the ocean circulation model method depends highly on the quality, temporal and spatial resolutions of ocean circulation models in different regions. For example, HYCOM works better in Alaska, while ECCO2 has a high correlation in New Zealand (Dobashi & Inazu, 2021). Inazu et al. (2012) designed a one-layer barotropic ocean circulation model to simulate the ocean bottom pressure $P_O(x,t)$. They further considered the effects of the seafloor bathymetry and air pressure compared to other ocean circulation models. However, it is challenging to simulate small and deep eddy flows owing to lacking ocean bottom observations. No matter how well the model is, it is impossible to include all the small-scale pressure perturbations in the model. Directly subtracting the ocean circulation model from the real seafloor pressure data may add additional errors to the data. The best-modeled pressures can only explain 50-80% variations in the real pressure data (Muramoto et al., 2019).

Isobath reference method is proposed by Fredrickson et al. (2019). Because of the along-margin spatial coherence of the ocean-generated pressure field, they used a pressure record at a site far from the posited SSE deformation at approximately the same depth as the reference station. They then subtracted the corresponding reference one in each station pair. The size of detectable SSE Mw ranges from 5-7, so the produced deformation fields with dimensions are smaller than 100 km. For this reason, the distance between the depth-matched station pairs should be larger than 100 km to avoid subtracting SSE signals and smaller than spatial correlation limitations. Seafloor pressures at the continental shelf are not only affected by depth variations but also the bathymetry and coastal trapped waves. The depth-matched station pairs should be analysis and well-considered in the local area (Inoue et al., 2021).

Seafloor pressure depends on sea surface height and upper column water density variations. Ocean water density relates to the surrounding water temperature and salinity changes (equation 3-2).

$$SSH(x,t) = P_O(x,t)/(\rho g) + gpan(x,t)/g, \tag{3-2}$$

where $gpan(x,t)$ is integrated from the bottom to the sea surface and is a function of temperature and salinity. The sea surface height, $SSH(x,t)$, varied with location x and time t, can be considered a linear combination of bottom pressure anomaly $P_O(x,t)$ and geopotential anomaly $gpan(x,t)$. ρ, g represents seawater density and acceleration term, respectively (Baker-Yeboah et al., 2011). Gomberg et al. (2019) indicated that seafloor temperature could be used as an independent proxy to remove oceanographic signals. The relation between the seafloor pressure and temperature was observed and studied in New Zealand and Japan (Baba et al., 2006; Gomberg et al., 2019; Itoh et al., 2019). However, such correlations are unstable and vary with time evolution and location. For example, the max cross-correlation coefficient in 2014 HOBITTS data ranges from 0.2 to 0.6, and the time lag is around 8-16 days for different stations (Gomberg et al., 2019). For some specific stations, LBPR4, the correlation is even negative. It is complicated to extract functional correlations to help remove oceanographic signals by working on seafloor pressure and temperature relationships.

All the above methods have their disadvantages. High variance reduction methods are not applicable for large study area, while low variance reduction methods may add additional errors to the residual. I want to find a new approach to reduce oceanographic noise and have minimum error uncertainties. Many features, such as sea surface height, sea surface temperature, seafloor temperature, seafloor salinity, and deep currents, are measurable and closely related to the water column contributed to seafloor pressure changes. However, these relationships are implicit and sometimes nonlinear. Summarizing an explicit and experienced equation and directly subtracting it is hard.

Machine learning can study nonlinear and implicit relationship between the input (features) and output (target) and has the potential to be a powerful tool for estimating the ocean circulation-generated bottom pressure. As a first step, I investigate how well machine learning works by using only variables co-located in space and time. Six measurable features are considered in this study, including sea surface height (SSH), sea surface temperature (SST), seafloor bottom temperature (B-Temp), seafloor bottom salinity (B-Sali), deep current east component (U), and deep current north component (V). I am exploring whether machine learning techniques can do better than just using SSH or B-Temp alone and which features affect the seafloor pressure the most. Based on my scientific questions, two machine learning methods: random forest and deep learning neural network, are used to study the relation between the features and target. Because real data is not abundant, I used the ocean circulation model data to build the training dataset. The random forest results show that the order of important features is SSH, B-Temp, SST, B-Sali, U, and V, and the proportion of importance of SSH is over 50%. The deep learning method shows a similar order to the random forest method, but it further studies the evolution of feature changes over time. For the later study, a well-trained model can be generalized with real data and build a new proxy to predict the oceanographic signals $P_O(x,t)$.

3.2 Method

I chose the southern Alaska subduction zone as the study area. HYCOM simulates the Alaska seafloor pressure better than other ocean circulation models and is chosen as the training data for the machine learning studies (Dobashi & Inazu, 2021). I downloaded ten years of HYCOM data from 2010 to 2019 in this area, including sea surface height and temperature, salinity, and deep currents data at all water column depths. Seafloor pressure is calculated by using equation 3-2. The spatial coverage of HYCOM ranges from 198 W to 210 W and 53 N to 59 N (Figure. 3.1), covering all the absolute pressure gauges in AACSE. I studied the relationship between different features: SSH, SST, B-Temp, B-Sali, U, and V, and seafloor pressure data using machine learning.

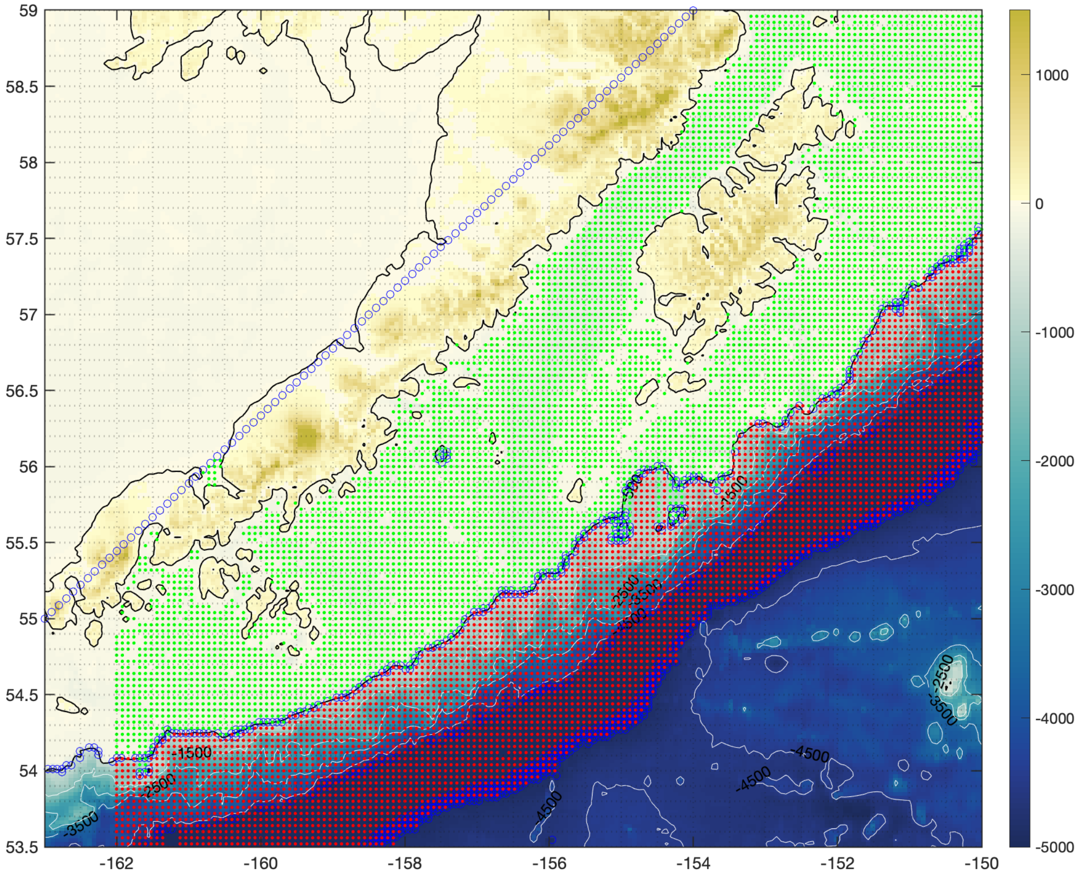

Figure 3.1 *Map of the study area in the Alaska-Aleutian megathrust. The red and green dots represent the HYCOM data. According to the depth, I separate the data into two parts: red dots for the continental slope region (500-5000 m) and green dots for the continental shelf region(50- 500m).*

The problem is supervised machine learning with a regression function. The features and seafloor pressure (target) are the input and output of the machine learning model. The machine learning model uses many simple linear and nonlinear formulas to explore the relations between the features and target relations. I first use a random forest method to determine which feature is the most important and how important they are. Then, I consider the time evolution of features using the deep learning method.

Pressure data on the continental shelf has a much larger amplitude than on the continental slope, and two different currents flow along the continental shelf and slope regions. The relationship between seafloor pressure and other features on the continental shelf and slope could be different. Thus, I separate the HYCOM data into two groups based on their depth (Figure 3.1). The continental shelf data includes depths from 50 – 500m, and continental slope data is at a depth of 500 – 5000m. The HYCOM space resolution is 1/12 degree, and the time resolution is 3 hours. Each part of the region includes about 6000 data points in 10 years.

Before train the machine learning model with the HYCOM data, I have to pre-process each piece of data. Because the high-frequency noises can be ignored in the data, I filter the high-frequency stuff in all the features and pressure data using a one-day low pass filter. Then I cut the data into 30-days pieces. I throw out the last part of the data in less than 30 days, avoiding data leakages during the training process. Finally, I make each piece of data zero mean and unit variance. Salinity and deep currents U and V data vary slightly in 30 days. Unit variance manipulation may cause substantial values and affect the training result. Here, I do not divide its standard if the standard deviation of 30-days data is less than 10^{-8}. Figure 3-2 shows the processed seafloor pressure data and six features. Because the data is processed in 30-dyas time window, there are some discontinuous segments in the long time series.

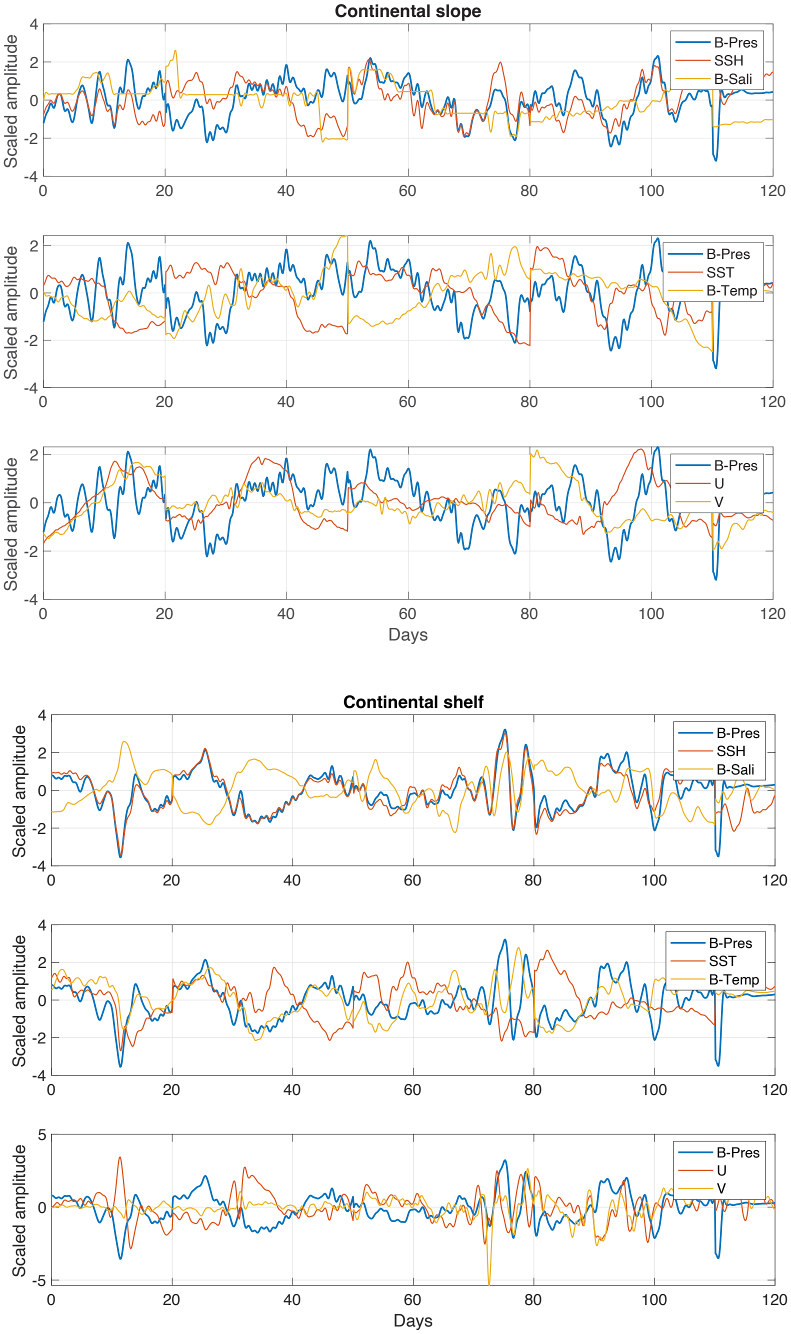

Figure 3.2. *The learning features and the seafloor pressure data at the continental slope and continental shelf regions. The six features are SSH (Sea Surface Height), B-Sali (Ocean Bottom Salinity), SST (Sea Surface Temperature), B-Temp (Ocean Bottom Temperature), U (ocean bottom deep current east component), and V (ocean bottom deep current north component)*

Machine learning study

Random forest regression uses an ensemble learning method for regression, which is the process of using multiple models trained over the same data, averaging the results of each model, and ultimately finding a robust predictive result. The random forest method can build many decision trees, and the errors of each decision tree are independent and different from tree to tree. Thus, this method is powerful and accurate for problems with complex and nonlinear relationships. I applied the random forest method by importing the scikit-learn package in Python. I also calculated the feature importance using the random forest built-in function. Larger importance indicates that the features have a more significant influence on predicting the target. The input and output data are six features and seafloor pressure simultaneously. I reshaped the data points into one long piece and separated the first 75% into the training dataset and the last 25% into the test dataset. The data points in the HYCOM output are very close. To make sure that the deep learning studies the relationship between features and output and does not memorize the result for adjacent stations, the training and test datasets are from different locations. The location of each dataset has no overlap. The motivation is to test whether the learned relationships can be applied to nearby areas. Besides, I did another test that separated the training and test dataset into two different time ranges. The training dataset includes the data from 2010 to 2017.5, and validation is from 2017.5 to 2019. This test can help evaluate whether the learned relationships can be applied to other time steps.

Some features, like seafloor temperature, show time lags with seafloor pressure, and it is hard to extract the time features and put them into the random forest method. Thus, I use a deep learning neural network to include the time information in the prediction. For this study, the input and output become the features and target in 30 days, so I cut the data into 30-days pieces without overlap. The deep learning architecture includes an encoder-decoder network (Figure 3.3), which is a popular network design in ML problems in generating dialogues (Serban et al., 2017), labeling semantic images (Badrinarayanan et al., 2015), detecting image forgeries (Bappy et al., 2019), and predicting vehicle trajectory (H. Park et al., 2018, p. 2). Seismic phase picking (Mousavi et al., 2020) and denoise seismic signals (Zhu & Beroza, 2019) also applied encoder-decoder network in seismology study.

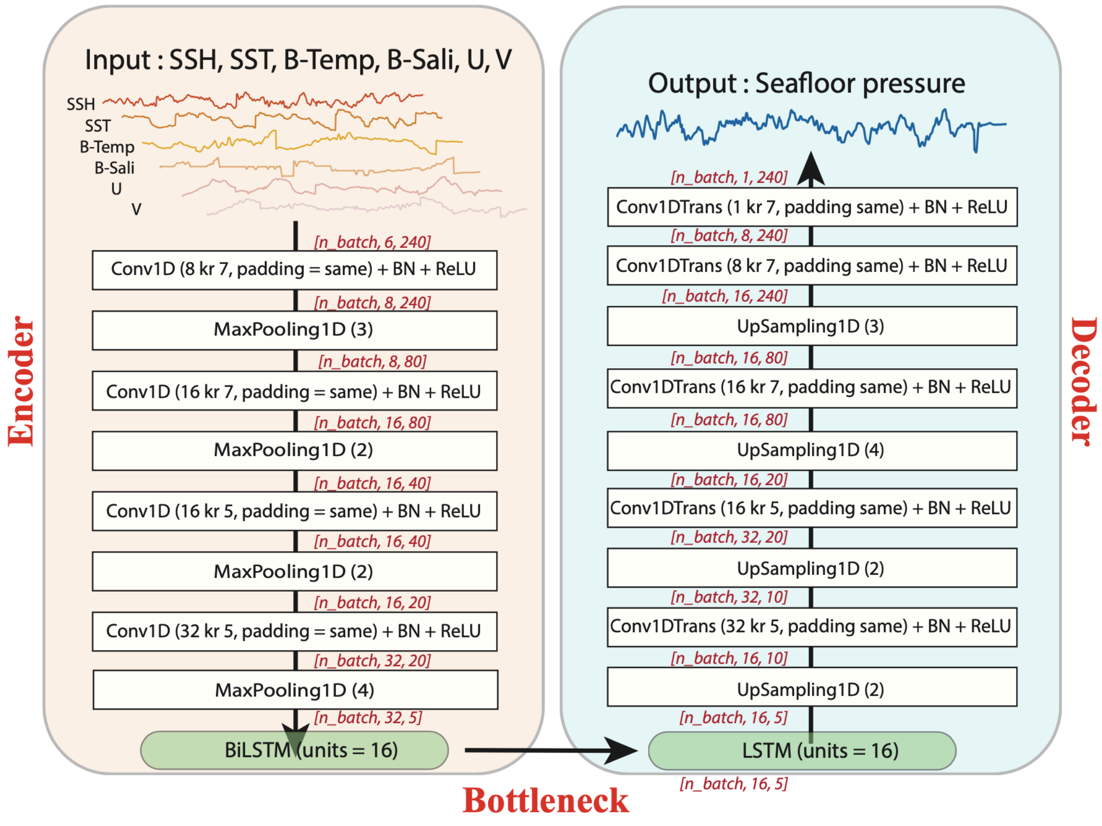

Figure 3.3: *The encoder-decoder neural network is to learn the relations between the features and seafloor pressure data. The network consists of 3 main blocks: encoder,*

bottleneck, and decoder branches. The encoder and decoder branches contain 4 and 5 one-dimensional convolutional and transpose convolutional layers. The layer parameters "x kr y, padding" refers to x kernels with y features and same padding that means output and input are the same size. Each convolutional and transpose convolutional layer is followed by a batch normalization (BN) layer and a ReLU antinational layer. A detailed explanation is discussed in the main text. The red numbers in the brackets show how the tensor size varies between layers [number of batches × number of channels × length of signal sequence].

The architecture includes three major parts: (1) The encoder branch takes the role of extracting beneficial, high-level characteristics from the input features. Through training with sufficient data and updating its parameters, the encoder aims to extract helpful input data characteristics that can help predict seafloor pressure. I used one-dimensional (1D) convolutional layers with increasing kernels to extract high-level features with a minimal number of parameters (Figure 3.3). The stride of the convolution is adjusted to down-sample the time series along the time axis. I tested using MaxPooling instead of convolutional strides but found poorer network performance. After each 1D convolutional layer, batch normalization is applied to normalize the output to zero-mean and unit variance. Finally, a rectified linear unit function (ReLU) is used as the activation function for non-linearity. (2). The decoder branch translates the learned features from the encoder branch and reconstructs the output time series. The branch is composed of 1D transpose convolutional layers. In symmetry with the encoder block, the number of kernels gradually decreases, and then the high-level characteristics are incorporated back into the time domain. I also applied batch-normalization and ReLU activation following each 1D transpose convolutional layer, like the encoder block. Only the final layer used linear activation to perform the seafloor pressure better. (3). The bottleneck block links the encoder and decoder branches. Its purpose is to learn the mapping relation between the encoder-extracted characteristics of the input features and the output seafloor pressure. Based on our previous study about machine learning detectors, combining convolutional neural network and LSTM (Long and short-term memory) shows a good performance on 1D time-series data. I also used LSTM to build the bottleneck block in this study (Figure 3.3). In total, the architecture includes around 23000 machine learning parameters.

I used a mean squared error as the loss function and chose ADAM algorithm for optimization (Kingma & Ba, 2014). In order to monitor the training process, I use an early stoppling of 10 steps to monitor the validation loss. The training process will be terminated if the validation loss is not improved for the subsequent rolling of 10 steps. I split the entire dataset into the training, validation, and test datasets with a proportion of 60%-20%-20%, respectively. Only the training data set is used to train the network, update the model parameters, and minimize the loss function. The validation data set is used to validate the model and track over-fitting during training. The testing data set is used to evaluate the performance of models after training. For the same reason as the random forest study, the training, validation, and test datasets have no overlap in the spatial domain.

I used the explained variance score (EVS) and R2 score to evaluate the performance of two machine learning models. The larger the two scores mean, the better the trained model. A score of 1 represents the predicted result equal to the real one. If two scores are less than 0, the predictions have many artifacts.

I tested the performance of the machine learning model with different size of training dataset. The random forest method has fewer learning parameters than the deep learning method, so the random forest method does not need lots of training data. I tested 1/10, 1/5, ½, and 1 of the training dataset, and the training performance did not improve. Thus, I used 1/10 of the training data to save computational time. However, in the deep learning study, I found the performance of the deep learning model increases with the number of the training dataset in a logarithmic form. I tested 0.2 and 0.5 million of the training dataset, and the performance of the continental slope dataset rises from 0.52 to 0.63. If I put more data into the deep learning model, the model can be trained better.

3.3 Result

I separated data into training and validation datasets for random forest study using location and time separation methods. These two methods show similar performance and importance factors (Figure 3.4). I used the mean value of EVS and R2 score to evaluate the model performance. The performance score for the continental shelf dataset is 0.92 for both methods. The high-performance score is that seafloor pressure is similar to the SSH at the continental shelf regions. The performance score is 0.89 if I only used SSH data. The continental slope dataset has a performance score of 0.51 because of the deep flow uncertainties. This number is much higher than that, only using the SSH data of 0.39. SSH is the most important feature in predicting seafloor pressure, especially for continental shelf data; its importance factor is over 0.9. For the continental shelf dataset, SST is slightly more important than B-Temp. B-Sali is the third important factor. U and V have a tiny importance proportion. The importance of SST, B-Sali, B-Temp, U, and V are all less than

3%. Their contribution can be ignored in the random forest model. B-Temp is more important than SST for the continental slope dataset because of the oceanic depth. The importance of B-Sali, U, and V are similar, and they are about 8%.

A critical parameter in the random forest model is the number of trees (n_estimator in scikit-learn). I tested the n_estimator from 20 to 40, and the model performance increased by less than 1%. Lager n_estimator will significantly add computational time, so I used n_estimator = 20 in this study.

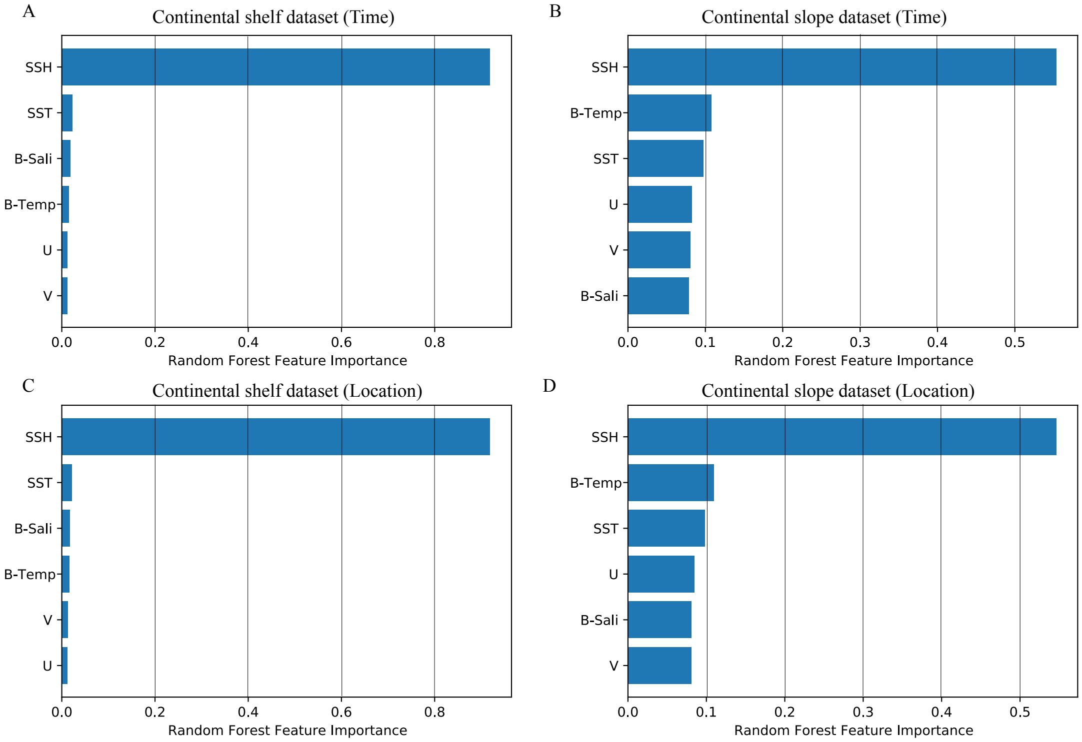

Figure 3.4. *The importance factor for different random forest training datasets. Figure A & B use the time separation dataset, and figure C and D use the location separation dataset. Figure A & C are from the continental shelf dataset and figure B & D are from the continental slope dataset.*

I also used different data separation methods in the deep learning model. However, the time separation dataset cannot be trained well, and its validation dataset is not improved during the training process. Therefore, I only show the result from the location separation dataset (Table 3.1 & Table 3.2). The continental shelf data achieves higher performance scores than the continental slope data because of the oceanic depth. Although SSH is the most important feature in predictions, other features still help to improve the training performance by about 3% in continental shelf data and 4% in slope data. Deep current velocities U and V seem useless in the continental shelf data and have an insignificant contribution to the continental slope data. SST and B-Temp are the second most important factor in predictions. B-Sali is the fourth important factor. These results are similar to the random forest.

The performance scores in the random forest and deep learning studies are not comparable. Their input and output lengths are different. The input and output of a random forest model are the features and target at one time. Even if I gave the continuous data to the random forest training model, the model could not consider the time evolutions of the features. When there is a time lag in the features, such as temperatures, the random forest model can not study it. On the contrary, the input and output for the deep learning model are 30-days time series. It can learn some intrinsic characteristics from the continuous 30-days time series data.

Table 3.1. *The performance of the continental shelf data*

Features	SSH, SST, B-Temp, B-Sali, U, V	SSH	SSH, SST	SSH, B-Temp	SSH, SST, B-Temp	SSH, SST, B-Temp, B-Sali	SSH, SST, B-Temp, U, V
EVS score R^2 score	0.79 0.79	0.76 0.76	0.78 0.78	0.76 0.76	0.78 0.78	0.79 0.79	0.79 0.78

Table 3.2. *The performance of the continental slope data*

Features	SSH, SST, B-Temp, B-Sali, U, V	SSH	SSH, SST	SSH, B-Temp	SSH, SST, B_Temp	SSH, SST, B-Temp, B-Sali	SSH, SST, B-Temp, U, V
EVS score R^2 score	0.63 0.63	0.59 0.58	0.61 0.60	0.61 0.61	0.61 0.61	0.62 0.61	0.63 0.62

In order to validate whether the trained relation can be applied to other regions, the training and validation dataset are from different areas. During the training process, there is a gap between the training and validation loss curves (Figure 3.5). Although the training loss is significantly lower than the validation loss, it does not mean over-training because both training and validation loss values are still improved with the epochs. Over-training means that the training loss continuously decreases, and validation loss increases.

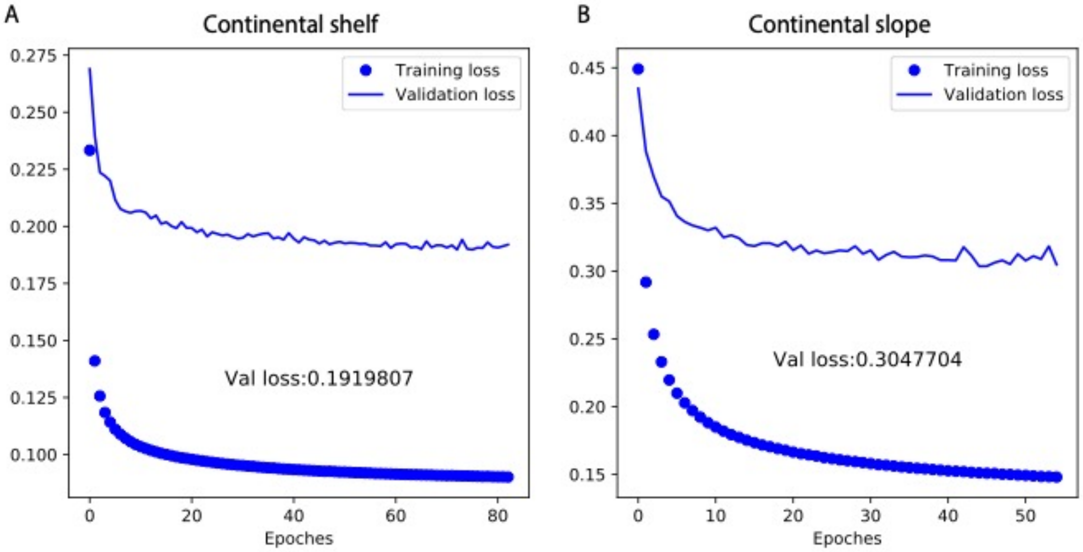

Figure 3.5. *The training and validation loss curve for the continental shelf (A) and the continental slope (B) data.*

Figure 3.6 shows the deep learning model test examples. Because seafloor pressure resembles the SSH, I calculate the EVS score for SSH (S_SSH) compared with S_Predict. The averaged S_SSH is 0.4 for continental shelf data and 0.89 for continental slope data. The deep learning model for the continental shelf data has a higher performance than SSH, but for the continental slope data, it has a lower performance than SSH. For the cases where S_Predict is smaller than S_HH, the machine learning model tends to predict a curve with fewer variations and to lack detailed features. Also, the EVS scores for machine learning prediction are all positive. It means that no artificial errors are produced during the predictions. If the machine learning model can not sufficiently study the relationship, it will output zeros rather than strange signals.

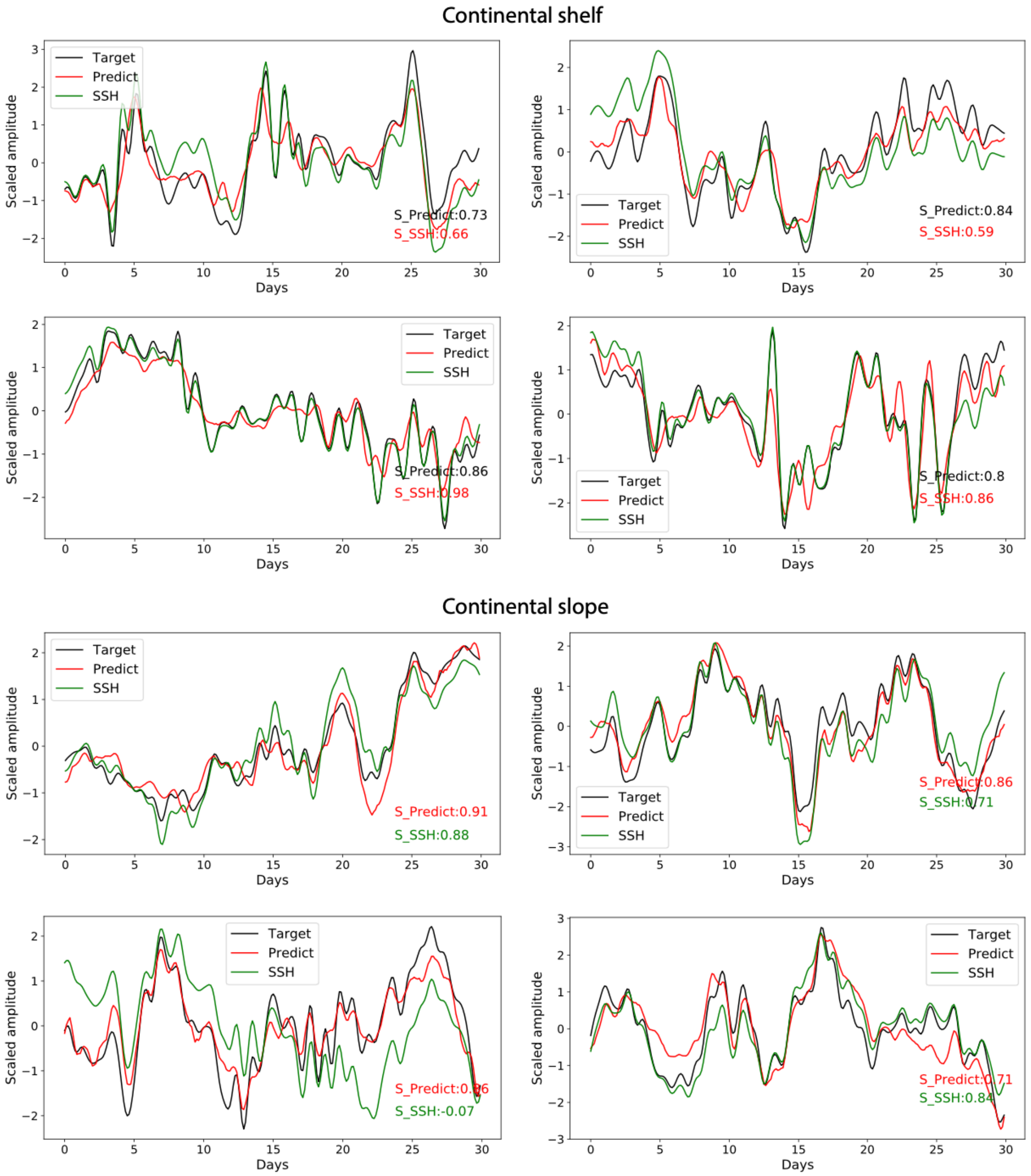

Figure 3.6. *Examples of the test dataset. The upper four figures are from the continental shelf data, and the lower four are from the continental slope data. Target means the seafloor pressure data. S_Predict represents the EVS score for the predicted result, and S_SSH means the EVS score for SSH data.*

3.4 Discussion and Conclusion

In the feature importance analysis, deep current velocities U and V have a tiny importance proportion. It might be due to the fact that U and V are proportional to pressure gradient instead of pressure. Therefore, if we consider the spatial variation of the pressure field, U and V could show a much higher importance factor. For the deep learning studies using continental slope data, U and V help improve the performance by about 2%. Even if the improvement is small, it indicates that, in the deep quiet ocean, the deep currents changes are slightly related to the pressure changes for the single station.

Besides, we found that SST and B-Temp have similar importance factors. Suppose the B-Temp is not available or has some issues in the seafloor temperature sensors. In that case, SST can be a good substitute for the B-Temp, available from the satellite altimetry measurement. In my trained result (Table 3.1), SST seems better than B-Temp for the continental shelf data. It could be because water column density depends more on SST than B-Temp. SST and B-Temp can help learn the ocean circulation contributed pressure changes, but their help is not significant. Their contribution is less than 10% in both machine learning models.

B-Sali is a feature that previous studies did not use, and it has minimal variations in the deep ocean. Although B-Sali is not as crucial as B-Temp in two machine learning models, B-Sali did help improve the predictions in the continental shelf and slope data. I suggest assembling a salinity measurement with absolute pressure gauges.

This study only considers the time evolution of features and ignores the spatial variations. In future research, the input data can be 2D feature data with 30-days images, consisting of both spatial and temporal information. The output data will be the pressure field with

30-days images. Simultaneously, the one-dimensional convolutional neural network could become two dimensions. This training process will require more data. This deep learning study uses about 0.6 million data. The suggested model will need much more data than this study. After the deep learning model is well trained, the model can be generalized using real observations. Then it can be used to estimate $P_O(x, t)$ and provide a new proxy to remove the ocean circulation contribution to seafloor pressure.

To conclude, I used six ocean circulation features and two machine learning methods to predict the bottom pressure. The sea surface height is essential in predicting the seafloor pressure among six features, and its importance is over 80% for continental slope and shelf data. Sea surface temperature and seafloor bottom temperature is the second most important factor. Seafloor salinity and deep current velocity are helpful in predictions, but their contributions are insignificant in time series data.

References

Aagaard, B. T., Knepley, M. G., & Williams, C. A. (2013). A domain decomposition approach to implementing fault slip in finite-element models of quasi-static and dynamic crustal deformation. *Journal of Geophysical Research: Solid Earth*, *118*(6), 3059–3079. https://doi.org/10.1002/jgrb.50217

Araki, E., Saffer, D. M., Kopf, A. J., Wallace, L. M., Kimura, T., Machida, Y., et al. (2017). Recurring and triggered slow-slip events near the trench at the Nankai Trough subduction megathrust. *Science*, *356*(6343), 1157–1160. https://doi.org/10.1126/science.aan3120

Baba, T., Hirata, K., Hori, T., & Sakaguchi, H. (2006). Offshore geodetic data conducive to the estimation of the afterslip distribution following the 2003 Tokachi-oki earthquake. *Earth and Planetary Science Letters*, *241*(1), 281–292. https://doi.org/10.1016/j.epsl.2005.10.019

Badrinarayanan, V., Handa, A., & Cipolla, R. (2015, May 27). SegNet: A Deep Convolutional Encoder-Decoder Architecture for Robust Semantic Pixel-Wise Labelling. arXiv. https://doi.org/10.48550/arXiv.1505.07293

Baillard, C., Crawford, W. C., Ballu, V., Hibert, C., & Mangeney, A. (2013). An Automatic Kurtosis-Based P- and S-Phase Picker Designed for Local Seismic Networks. *Bulletin of the Seismological Society of America*, *104*(1), 394–409. https://doi.org/10.1785/0120120347

Baker-Yeboah, S., Watts, D. R., Byrne, D. A., & Witter, D. L. (2011). Sea Surface Height Variability in the eastern South Atlantic from Satellite and in situ Measurements, *2011*, OS23A-1620.

Bappy, J. H., Simons, C., Nataraj, L., Manjunath, B. S., & Roy-Chowdhury, A. K. (2019). Hybrid LSTM and Encoder–Decoder Architecture for Detection of Image Forgeries. *IEEE Transactions on Image Processing*, *28*(7), 3286–3300. https://doi.org/10.1109/TIP.2019.2895466

Barcheck, G., Abers, G. A., Adams, A. N., Bécel, A., Collins, J., Gaherty, J. B., et al. (2020). The Alaska Amphibious Community Seismic Experiment. *Seismological Research Letters*, *91*(6), 3054–3063. https://doi.org/10.1785/0220200189

Bartlow, N. M., Wallace, L. M., Beavan, R. J., Bannister, S., & Segall, P. (2014). Time-dependent modeling of slow slip events and associated seismicity and tremor at the Hikurangi subduction zone, New Zealand. *Journal of Geophysical Research: Solid Earth*, *119*(1), 734–753. https://doi.org/10.1002/2013JB010609

Bergen, K. J., Johnson, P. A., Hoop, M. V. de, & Beroza, G. C. (2019). Machine learning for data-driven discovery in solid Earth geoscience. *Science*, *363*(6433). https://doi.org/10.1126/science.aau0323

Beroza, G. C., & Ide, S. (2011). Slow Earthquakes and Nonvolcanic Tremor. *Annual Review of Earth and Planetary Sciences*, *39*(1), 271–296. https://doi.org/10.1146/annurev-earth-040809-152531

Bürgmann, R. (2018). The geophysics, geology and mechanics of slow fault slip. *Earth and Planetary Science Letters*, *495*, 112–134. https://doi.org/10.1016/j.epsl.2018.04.062

Chen, K. H., Tai, H.-J., Ide, S., Byrne, T. B., & Johnson, C. W. (2018). Tidal Modulation and Tectonic Implications of Tremors in Taiwan. *Journal of Geophysical Research: Solid Earth*, *123*(7), 5945–5964. https://doi.org/10.1029/2018JB015663

Crowell, B. W., & Melgar, D. (2020). Slipping the Shumagin Gap: A Kinematic Coseismic and Early Afterslip Model of the Mw 7.8 Simeonof Island, Alaska, Earthquake. *Geophysical Research Letters*, *47*(19), e2020GL090308. https://doi.org/10.1029/2020GL090308

Cummings, J. A., & Smedstad, O. M. (2013). Variational Data Assimilation for the Global Ocean. In S. K. Park & L. Xu (Eds.), *Data Assimilation for Atmospheric, Oceanic* *and Hydrologic Applications (Vol. II)* (pp. 303–343). Berlin, Heidelberg: Springer. https://doi.org/10.1007/978-3-642-35088-7_13

Davies, J., Sykes, L., House, L., & Jacob, K. (1981). Shumagin Seismic Gap, Alaska Peninsula: History of great earthquakes, tectonic setting, and evidence for high seismic potential. *Journal of Geophysical Research: Solid Earth*, *86*(B5), 3821–3855. https://doi.org/10.1029/JB086iB05p03821

Davis, E. E., Villinger, H., & Sun, T. (2015). Slow and delayed deformation and uplift of the outermost subduction prism following ETS and seismogenic slip events beneath Nicoya Peninsula, Costa Rica. *Earth and Planetary Science Letters*, *410*, 117–127. https://doi.org/10.1016/j.epsl.2014.11.015

Dixon, T. H., Jiang, Y., Malservisi, R., McCaffrey, R., Voss, N., Protti, M., & Gonzalez, V. (2014). Earthquake and tsunami forecasts: Relation of slow slip events to subsequent earthquake rupture. *Proceedings of the National Academy of Sciences*, *111*(48), 17039–17044.

Dobashi, Y., & Inazu, D. (2021). Improving Detectability of Seafloor Deformation From Bottom Pressure Observations Using Numerical Ocean Models. *Frontiers in Earth Science*, *8*. https://doi.org/10.3389/feart.2020.598270

Fredrickson, E. K., Wilcock, W. S. D., Schmidt, D. A., MacCready, P., Roland, E., Kurapov, A. L., et al. (2019). Optimizing Sensor Configurations for the Detection of Slow-Slip Earthquakes in Seafloor Pressure Records, Using the Cascadia Subduction Zone as a Case Study. *Journal of Geophysical Research: Solid Earth*, *124*(12), 13504–13531. https://doi.org/10.1029/2019JB018053

Freymueller, J. T., Suleimani, E. N., & Nicolsky, D. J. (2021). Constraints on the Slip Distribution of the 1938 MW 8.3 Alaska Peninsula Earthquake From Tsunami Modeling. *Geophysical Research Letters*, *48*(9), e2021GL092812. https://doi.org/10.1029/2021GL092812

Gomberg, J., Hautala, S., Johnson, P., & Chiswell, S. (2019). Separating Sea and Slow Slip Signals on the Seafloor. *Journal of Geophysical Research: Solid Earth*, *124*(12), 13486–13503. https://doi.org/10.1029/2019JB018285

Hayes, G. P., Moore, G. L., Portner, D. E., Hearne, M., Flamme, H., Furtney, M., & Smoczyk, G. M. (2018). Slab2, a comprehensive subduction zone geometry model. *Science*, *362*(6410), 58–61. https://doi.org/10.1126/science.aat4723

He, B., Watts, R. D., Tracey, K. L., Donohue, K. A., & Wei, M. (2018). Reducing `Noise’ in Ocean Bottom Pressure Measurements in the Cascadia Subduction Zone. *AGU Fall Meeting Abstracts*, *T41F-0369*. Retrieved from http://adsabs.harvard.edu/abs/2018AGUFM.T41F0369H

He, B., Wei, M., Watts, D. R., & Shen, Y. (2020). Detecting Slow Slip Events From Seafloor Pressure Data Using Machine Learning. *Geophysical Research Letters*, *47*(11), e2020GL087579. https://doi.org/10.1029/2020GL087579

Hino, R., Inazu, D., Ohta, Y., Ito, Y., Suzuki, S., Iinuma, T., et al. (2014). Was the 2011 Tohoku-Oki earthquake preceded by aseismic preslip? Examination of seafloor vertical deformation data near the epicenter. *Marine Geophysical Research*, *35*(3), 181–190. https://doi.org/10.1007/s11001-013-9208-2

Huene, R. von, Miller, J. J., & Dartnell, P. (2016). A possible transoceanic tsunami directed toward the U.S. west coast from the Semidi segment, Alaska convergent margin. *Geochemistry, Geophysics, Geosystems*, *17*(3), 645–659. https://doi.org/10.1002/2015GC006147

Ide, S. (2012). Variety and spatial heterogeneity of tectonic tremor worldwide. *Journal of Geophysical Research: Solid Earth*, *117*(B3). https://doi.org/10.1029/2011JB008840

Inazu, D., Hino, R., & Fujimoto, H. (2012). A global barotropic ocean model driven by synoptic atmospheric disturbances for detecting seafloor vertical displacements from in situ ocean bottom pressure measurements. *Marine Geophysical Research*, *33*(2), 127–148. https://doi.org/10.1007/s11001-012-9151-7

Inoue, T., Ito, Y., Wallace, L. M., Yoshikawa, Y., Inazu, D., Garcia, E. S. M., et al. (2021). Water Depth Dependence of Long-Range Correlation in Nontidal Variations in Seafloor Pressure. *Geophysical Research Letters*, *48*(8), e2020GL092173. https://doi.org/10.1029/2020GL092173

Ito, Y., Hino, R., Kido, M., Fujimoto, H., Osada, Y., Inazu, D., et al. (2013a). Episodic slow slip events in the Japan subduction zone before the 2011 Tohoku-Oki earthquake. *Tectonophysics*, *600*, 14–26. https://doi.org/10.1016/j.tecto.2012.08.022

Ito, Y., Hino, R., Kido, M., Fujimoto, H., Osada, Y., Inazu, D., et al. (2013b). Episodic slow slip events in the Japan subduction zone before the 2011 Tohoku-Oki earthquake. *Tectonophysics*, *600*, 14–26. https://doi.org/10.1016/j.tecto.2012.08.022

Itoh, Y., Nishimura, T., Ariyoshi, K., & Matsumoto, H. (2019). Interplate Slip Following the 2003 Tokachi-oki Earthquake From Ocean Bottom Pressure Gauge and Land GNSS Data. *Journal of Geophysical Research: Solid Earth*, *124*(4), 4205–4230. https://doi.org/10.1029/2018JB016328

Kingma, D. P., & Ba, J. (2014). Adam: A Method for Stochastic Optimization. *ArXiv:1412.6980 [Cs]*. Retrieved from http://arxiv.org/abs/1412.6980

Kong, Q., Trugman, D. T., Ross, Z. E., Bianco, M. J., Meade, B. J., & Gerstoft, P. (2019). Machine Learning in Seismology: Turning Data into Insights. *Seismological Research Letters*, *90*(1), 3–14. https://doi.org/10.1785/0220180259

Li, J., Shillington, D. J., Bécel, A., Nedimović, M. R., Webb, S. C., Saffer, D. M., et al. (2015). Downdip variations in seismic reflection character: Implications for fault structure and seismogenic behavior in the Alaska subduction zone. *Journal of Geophysical Research: Solid Earth*, *120*(11), 7883–7904. https://doi.org/10.1002/2015JB012338

Li, J., Shillington, D. J., Saffer, D. M., Bécel, A., Nedimović, M. R., Kuehn, H., et al. (2018). Connections between subducted sediment, pore-fluid pressure, and earthquake behavior along the Alaska megathrust. *Geology*, *46*(4), 299–302. https://doi.org/10.1130/G39557.1

Li, S., & Freymueller, J. T. (2018). Spatial Variation of Slip Behavior Beneath the Alaska Peninsula Along Alaska-Aleutian Subduction Zone. *Geophysical Research Letters*, *45*(8), 3453–3460. https://doi.org/10.1002/2017GL076761

Li, S., Freymueller, J., & McCaffrey, R. (2016). Slow slip events and time-dependent variations in locking beneath Lower Cook Inlet of the Alaska-Aleutian subduction zone. *Journal of Geophysical Research: Solid Earth*, *121*(2), 1060–1079. https://doi.org/10.1002/2015JB012491

Lindsey, E. O., Mallick, R., Hubbard, J. A., Bradley, K. E., Almeida, R. V., Moore, J. D. P., et al. (2021). Slip rate deficit and earthquake potential on shallow megathrusts. *Nature Geoscience*, *14*(5), 321–326. https://doi.org/10.1038/s41561-021-00736-x

Liu, C., Lay, T., Xiong, X., & Wen, Y. (2020). Rupture of the 2020 MW 7.8 Earthquake in the Shumagin Gap Inferred From Seismic and Geodetic Observations. *Geophysical Research Letters*, *47*(22), e2020GL090806. https://doi.org/10.1029/2020GL090806

Liu, C., Lay, T., & Xiong, X. (2022). The 29 July 2021 MW 8.2 Chignik, Alaska Peninsula Earthquake Rupture Inferred From Seismic and Geodetic Observations: Re-Rupture of the Western 2/3 of the 1938 Rupture Zone. *Geophysical Research Letters*, *49*(4), e2021GL096004. https://doi.org/10.1029/2021GL096004

Lomax, A., Virieux, J., Volant, P., & Berge-Thierry, C. (2000). Probabilistic Earthquake Location in 3D and Layered Models. In C. H. Thurber & N. Rabinowitz (Eds.), *Advances in Seismic Event Location* (pp. 101–134). Dordrecht: Springer Netherlands. https://doi.org/10.1007/978-94-015-9536-0_5

Montgomery-Brown, E. K., & Syracuse, E. M. (2015). Tremor-genic slow slip regions may be deeper and warmer and may slip slower than non-tremor-genic regions. *Geochemistry, Geophysics, Geosystems*, *16*(10), 3593–3606. https://doi.org/10.1002/2015GC005895

Moseley, B., Markham, A., & Nissen-Meyer, T. (2018). Fast approximate simulation of seismic waves with deep learning. *ArXiv:1807.06873 [Physics]*. Retrieved from http://arxiv.org/abs/1807.06873

Mousavi, S. M., Zhu, W., Sheng, Y., & Beroza, G. C. (2019). CRED: A Deep Residual Network of Convolutional and Recurrent Units for Earthquake Signal Detection. *Scientific Reports*, *9*(1), 1–14. https://doi.org/10.1038/s41598-019-45748-1

Mousavi, S. M., Ellsworth, W. L., Zhu, W., Chuang, L. Y., & Beroza, G. C. (2020). Earthquake transformer—an attentive deep-learning model for simultaneous earthquake detection and phase picking. *Nature Communications*, *11*(1), 3952. https://doi.org/10.1038/s41467-020-17591-w

Munk, W. H., Cartwright, D. D., & Bullard, E. C. (1966). Tidal spectroscopy and prediction. *Philosophical Transactions of the Royal Society of London. Series A, Mathematical and Physical Sciences*, *259*(1105), 533–581. https://doi.org/10.1098/rsta.1966.0024

Muramoto, T., Ito, Y., Inazu, D., Wallace, L. M., Hino, R., Suzuki, S., et al. (2019). Seafloor Crustal Deformation on Ocean Bottom Pressure Records With Nontidal

Variability Corrections: Application to Hikurangi Margin, New Zealand. *Geophysical Research Letters*, *46*(1), 303–310. https://doi.org/10.1029/2018GL080830

Nanjo, K. Z., Hirata, N., Obara, K., & Kasahara, K. (2012). Decade-scale decrease inb value prior to the M9-class 2011 Tohoku and 2004 Sumatra quakes. *Geophysical Research Letters*, *39*(20). https://doi.org/10.1029/2012GL052997

Nishikawa, T., & Ide, S. (2018). Recurring Slow Slip Events and Earthquake Nucleation in the Source Region of the M 7 Ibaraki-Oki Earthquakes Revealed by Earthquake Swarm and Foreshock Activity. *Journal of Geophysical Research: Solid Earth*, *123*(9), 7950–7968. https://doi.org/10.1029/2018JB015642

Park, H., Oh, C., Moon, J., & Kim, S. (2018). Development of a lane change risk index using vehicle trajectory data. *Accident Analysis & Prevention*, *110*, 1–8. https://doi.org/10.1016/j.aap.2017.10.015

Perol, T., Gharbi, M., & Denolle, M. (2018). Convolutional neural network for earthquake detection and location. *Science Advances*, *4*(2), e1700578. https://doi.org/10.1126/sciadv.1700578

Polster, A., Fabian, M., & Villinger, H. (2009). Effective resolution and drift of Paroscientific pressure sensors derived from long-term seafloor measurements. *Geochemistry, Geophysics, Geosystems*, *10*(8). https://doi.org/10.1029/2009GC002532

Reverso, T., Marsan, D., Helmstetter, A., & Enescu, B. (2016). Background seismicity in Boso Peninsula, Japan: Long-term acceleration, and relationship with slow slip events. *Geophysical Research Letters*, *43*(11), 5671–5679. https://doi.org/10.1002/2016GL068524

Ross, Z. E., White, M. C., Vernon, F. L., & Ben-Zion, Y. (2016). An Improved Algorithm for Real-Time S-Wave Picking with Application to the (Augmented) ANZA Network in Southern California. *Bulletin of the Seismological Society of America*, *106*(5), 2013–2022. https://doi.org/10.1785/0120150230

Rousset, B., Fu, Y., Bartlow, N., & Bürgmann, R. (2019). Weeks-Long and Years-Long Slow Slip and Tectonic Tremor Episodes on the South Central Alaska Megathrust. *Journal of Geophysical Research: Solid Earth*, *124*(12), 13392–13403. https://doi.org/10.1029/2019JB018724

Ruiz, S., Metois, M., Fuenzalida, A., Ruiz, J., Leyton, F., Grandin, R., et al. (2014). Intense foreshocks and a slow slip event preceded the 2014 Iquique Mw 8.1 earthquake. *Science*, *345*(6201), 1165–1169. https://doi.org/10.1126/science.1256074

Saffer, D. M., & Wallace, L. M. (2015). The frictional, hydrologic, metamorphic and thermal habitat of shallow slow earthquakes. *Nature Geoscience*, *8*(8), 594–600. https://doi.org/10.1038/ngeo2490

Schorlemmer, D., & Wiemer, S. (2005). Microseismicity data forecast rupture area. *Nature*, *434*(7037), 1086–1086. https://doi.org/10.1038/4341086a

Schorlemmer, D., Wiemer, S., & Wyss, M. (2005). Variations in earthquake-size distribution across different stress regimes. *Nature*, *437*(7058), 539–542. https://doi.org/10.1038/nature04094

Serban, I., Klinger, T., Tesauro, G., Talamadupula, K., Zhou, B., Bengio, Y., & Courville, A. (2017). Multiresolution Recurrent Neural Networks: An Application to Dialogue Response Generation. *Proceedings of the AAAI Conference on Artificial Intelligence*, *31*(1). https://doi.org/10.1609/aaai.v31i1.10984

Shillington, D. J., Bécel, A., Nedimović, M. R., Kuehn, H., Webb, S. C., Abers, G. A., et al. (2015). Link between plate fabric, hydration and subduction zone seismicity in Alaska. *Nature Geoscience*, *8*(12), 961–964. https://doi.org/10.1038/ngeo2586

Shoji, D., Noguchi, R., Otsuki, S., & Hino, H. (2018). Classification of volcanic ash particles using a convolutional neural network and probability. *Scientific Reports*, *8*(1), 1–12. https://doi.org/10.1038/s41598-018-26200-2

Stevenson, A. J., Scholl, D. W., & Vallier, T. L. (1983). Tectonic and geologic implications of the Zodiac fan, Aleutian Abyssal Plain, northeast Pacific. *GSA Bulletin*, *94*(2), 259–273. https://doi.org/10.1130/0016-7606(1983)94<259:TAGIOT>2.0.CO;2

Suzuki, K., Nakano, M., Takahashi, N., Hori, T., Kamiya, S., Araki, E., et al. (2016). Synchronous changes in the seismicity rate and ocean-bottom hydrostatic pressures along the Nankai trough: A possible slow slip event detected by the Dense Oceanfloor Network system for Earthquakes and Tsunamis (DONET). *Tectonophysics*, *680*, 90–98. https://doi.org/10.1016/j.tecto.2016.05.012

Todd, E. K., & Schwartz, S. Y. (2016). Tectonic tremor along the northern Hikurangi Margin, New Zealand, between 2010 and 2015. *Journal of Geophysical Research: Solid Earth*, *121*(12), 8706–8719. https://doi.org/10.1002/2016JB013480

Todd, E. K., Schwartz, S. Y., Mochizuki, K., Wallace, L. M., Sheehan, A. F., Webb, S. C., et al. (2018). Earthquakes and Tremor Linked to Seamount Subduction During Shallow Slow Slip at the Hikurangi Margin, New Zealand. *Journal of Geophysical Research: Solid Earth*, *123*(8), 6769–6783. https://doi.org/10.1029/2018JB016136

Vallée, M., Nocquet, J.-M., Battaglia, J., Font, Y., Segovia, M., Régnier, M., et al. (2013). Intense interface seismicity triggered by a shallow slow slip event in the Central Ecuador subduction zone. *Journal of Geophysical Research: Solid Earth*, *118*(6), 2965–2981. https://doi.org/10.1002/jgrb.50216

Wallace, L. M., Webb, S. C., Ito, Y., Mochizuki, K., Hino, R., Henrys, S., et al. (2016). Slow slip near the trench at the Hikurangi subduction zone, New Zealand. *Science*, *352*(6286), 701–704.

Wang, F., Wei, S. S., Ruppert, N. A., & Zhang, H. (2021). Seismic imaging of the Alaska Peninsula using the body-wave double-difference tomography. AGU. Retrieved from https://agu.confex.com/agu/fm21/meetingapp.cgi/Paper/903665

Wang, Q., Guo, Y., Yu, L., & Li, P. (2017). Earthquake Prediction based on Spatio-Temporal Data Mining: An LSTM Network Approach. *IEEE Transactions on Emerging Topics in Computing*, 1–1. https://doi.org/10.1109/TETC.2017.2699169

Warren-Smith, E., Fry, B., Wallace, L., Chon, E., Henrys, S., Sheehan, A., et al. (2019). Episodic stress and fluid pressure cycling in subducting oceanic crust during slow slip. *Nature Geoscience*, *12*(6), 475–481. https://doi.org/10.1038/s41561-019-0367-x

Watts, D. R., & Kontoyiannis, H. (1990). Deep-Ocean Bottom Pressure Measurement: Drift Removal and Performance. *Journal of Atmospheric and Oceanic Technology*, *7*(2), 296–306. https://doi.org/10.1175/1520-0426(1990)007<0296:DOBPMD>2.0.CO;2

Wech, A. G., Sheehan, A. F., Boese, C. M., Townend, J., Stern, T. A., & Collins, J. A. (2013). Tectonic Tremor Recorded by Ocean Bottom Seismometers. *Seismological Research Letters*, *84*(5), 752–758. https://doi.org/10.1785/0220120184

Wech, Aaron G., & Creager, K. C. (2008). Automated detection and location of Cascadia tremor. *Geophysical Research Letters*, *35*(20). https://doi.org/10.1029/2008GL035458

Wei, M., McGuire, J. J., & Richardson, E. (2012). A slow slip event in the south central Alaska Subduction Zone and related seismicity anomaly. *Geophysical Research Letters*, *39*(15). https://doi.org/10.1029/2012GL052351

Wei, S. S., Ruprecht, P., Gable, S. L., Huggins, E. G., Ruppert, N., Gao, L., & Zhang, H. (2021). Along-strike variations in intermediate-depth seismicity and arc magmatism along the Alaska Peninsula. *Earth and Planetary Science Letters*, *563*, 116878. https://doi.org/10.1016/j.epsl.2021.116878

Wei, X., Shen, Y., Caplan-Auerbach, J., & Morgan, J. (2020). An improved earthquake catalog during the 2018 Kīlauea Volcano eruption from combined onshore and offshore seismic arrays. AGU. Retrieved from https://agu.confex.com/agu/fm20/meetingapp.cgi/Paper/689044

Wiszniowski, J., Plesiewicz, B. M., & Trojanowski, J. (2014). Application of real time recurrent neural network for detection of small natural earthquakes in Poland. *Acta Geophysica*, *62*(3), 469–485. https://doi.org/10.2478/s11600-013-0140-2

Withers, M., Aster, R., Young, C., Beiriger, J., Harris, M., Moore, S., & Trujillo, J. (1998). A comparison of select trigger algorithms for automated global seismic phase and event detection. *Bulletin of the Seismological Society of America*, *88*(1), 95–106. https://doi.org/10.1785/BSSA0880010095

Xiao, Z., Freymueller, J. T., Grapenthin, R., Elliott, J. L., Drooff, C., & Fusso, L. (2021). The deep Shumagin gap filled: Kinematic rupture model and slip budget analysis of the 2020 Mw 7.8 Simeonof earthquake constrained by GNSS, global seismic waveforms, and floating InSAR. *Earth and Planetary Science Letters*, *576*, 117241. https://doi.org/10.1016/j.epsl.2021.117241

Yarce, J., Sheehan, A. F., Nakai, J. S., Schwartz, S. Y., Mochizuki, K., Savage, M. K., et al. (2019). Seismicity at the Northern Hikurangi Margin, New Zealand, and Investigation of the Potential Spatial and Temporal Relationships With a Shallow Slow Slip Event. *Journal of Geophysical Research: Solid Earth*, *124*(5), 4751–4766. https://doi.org/10.1029/2018JB017211

Ye, L., Lay, T., Kanamori, H., Yamazaki, Y., & Cheung, K. F. (2021). The 22 July 2020 MW 7.8 Shumagin seismic gap earthquake: Partial rupture of a weakly coupled megathrust. *Earth and Planetary Science Letters*, *562*, 116879. https://doi.org/10.1016/j.epsl.2021.116879

Zhu, W., & Beroza, G. C. (2019). PhaseNet: a deep-neural-network-based seismic arrival-time picking method. *Geophysical Journal International*, *216*(1), 261–273. https://doi.org/10.1093/gji/ggy423